Fall 12-2014

Computational and Experimental Investigation Into Yield Behavior and Cure Rate Dependence of Thermoset Polymers

Christopher Harold Childers
University of Southern Mississippi

The University of Southern Mississippi

COMPUTATIONAL AND EXPERIMENTAL INVESTIGATION INTO YIELD BEHAVIOR AND CURE RATE DEPENDENCE OF THERMOSET POLYMERS

by

Christopher Harold Childers

Abstract of a Dissertation
Submitted to the Graduate School
of The University of Southern Mississippi
in Partial Fulfillment of the Requirements
for the Degree of Doctor of Philosophy

December 2014

ABSTRACT

COMPUTATIONAL AND EXPERIMENTAL INVESTIGATION INTO YIELD BEHAVIOR AND CURE RATE DEPENDENCE OF THERMOSET POLYMERS

by Christopher Harold Childers

December 2014

This dissertation is broken down into two primary sections: firstly, the development and improvement of molecular dynamics simulations of thermoset matrix polymers including their use in understanding molecular response to applied strain deformation and secondly, the discernment of a cure heating ramp rate dependence of the final molecular and macro-molecular properties of thermoset matrix polymer.

The molecular dynamics section will discuss the development of molecular dynamics simulations of thermoset epoxy/amine matrix polymers, and the implementation of this work to determine the underlying molecular level events that cause thermoset matrix polymer yield. It will report a novel method for the determination of the strain at yield for thermoset matrix polymers and is based on the monitoring of the van der Waals potential energy. A correlation exists between the uptake of the van der Waals energy in the matrix polymer and the yield strain of the matrix. This analysis is a method to simulate the polymer yield and a method of understanding the nature of material yield.

The second section of this dissertation will discuss a cure heating ramp rate dependence for thermoset matrix polymers based on epoxy/amine chemistry. Initially, this dependence was studied for a 33DDS/DGEBF matrix polymer. Using DSC and NIR it was found that the network growth mechanism is altered significantly by the cure

heating ramp rate, which results in differences in the final network architecture for these polymers. These differences are most apparent in changes in the free volume hole size and the dielectric responses for these networks. It was found that the hole size decreased from approximately 65 to 50 $Å^3$ when changing the cure ramp rate from 1–10 °C/min. Furthermore, the distribution of relaxation times $G(\tau)$ was altered by a variation of the cure heating ramp rate. In addition to the di-functional epoxide DGEBF, matrix polymers comprised of TGDDM/33DDS and TGDDM/44DDS were also studied for cure ramp rate dependence. It was found that these polymers also exhibit cure ramp rate dependence; however, the dependence itself appears to be chemistry specific, as the responses for the TGDDM systems are different than those for the DGEBF matrix.

The University of Southern Mississippi

COMPUTATIONAL AND EXPERIMENTAL INVESTIGATION INTO YIELD BEHAVIOR AND CURE RATE DEPENDENCE OF THERMOSET POLYMERS

by

Christopher Harold Childers

A Dissertation
Submitted to the Graduate School
of The University of Southern Mississippi
in Partial Fulfillment of the Requirements
for the Degree of Doctor of Philosophy

Approved:

Dr. Jeffrey Wiggins
Committee Chair

Dr. Sarah Morgan

Dr. Derek Patton

Dr. James Rawlins

Dr. Robson Storey

Dr. Karen Coats
Dean of the Graduate School

December 2014

DEDICATION

This dissertation is dedicated to my wonderful wife, Kendyl, who has stood by my side throughout the entire process of graduate school and has kept pushing me even when I could not push myself. I would also like to dedicate this dissertation to my parents, Anthony and Lisa Childers, as well as those who have inspired me to pursue knowledge while keeping focused on the things in life that are truly important.

ACKNOWLEDGMENTS

I would first and foremost like to acknowledge my advisor, Dr. Jeffrey Wiggins, for his instruction and support these past several years. From Dr. Wiggins, I learned what it really means to obtain a doctoral degree and to be a scientist. He taught me many invaluable skills in graduate school that I did not even expect to learn, and for that I am both humbled and grateful. I would also like to thank the members of my committee: Dr. Sarah Morgan, Dr. Derek Patton, Dr. Rob Storey, and Dr. James Rawlins for their contribution to my education.

I would also like to thank those persons whom I have collaborated with over the years for their contribution to my work and development as a scientist. Specifically, Dr. Samuel Tucker, Dr. Rob Maskell, Dr. Matthew Jackson, and Steve Christensen.

Contributions from several researchers made this possible, and I would like to acknowledge Dr Jim Geotz for his assistance with PALS samples and Dr. Mohammad Hassan for his assistance with the dielectric experiments and analysis.

Finally, I would like to thank the members of the Wiggins Research Group, especially John Misasi, Jeremy Moskowitz, and Brian Greenhoe for supporting my work.

TABLE OF CONTENTS

LIST OF TABLES

Table

LIST OF ILLUSTRATIONS

Figure

CHAPTER I

INTRODUCTION

Preface

Carbon fiber reinforced polymer composites, or CFPS's, are the current state-of-the-art material for lightweight, high performance applications. Due to their high strength to weight ratio when compared to traditional materials (such as metals), CFRP's have begun to replace metals in a wide variety of applications, including construction, automotive, aerospace, and defense. While each application has specific demands, in general, CFRP's are composed of a carbon fiber reinforcement phase and a polymer matrix phase. While a considerable amount of effort and resources are going into developing the next generation of carbon fibers, advances in the polymer matrix component must also be realized in order to achieve full utility from CFRP's. To that end, this dissertation will focus on advancing fundamental understanding of the polymer matrix materials.

Composites and Matrix Polymers

CFRP's realize a specific strength (failure strength to density ratio) that is currently unprecedented among other known materials. Despite their high performance, the maximum utility of a CFRP has not been realized. For example, if a carbon fiber tested for mechanical strength in tension has a modulus of around 276 GPa, the 0° fiber orientation epoxy matrix composite fabricated with this fiber would display a tensile modulus of around 164 GPa.[1] This reduction in properties is generally attributed to the matrix contribution in the composite, but the exact mechanism for the property decrease is not known. In general, the decrease is contributed to either the load transfer within an interphase region that exists between the matrix and fiber or residual stresses generated

within the matrix during cure.[2,3] Further, while it is agreed that residual stress is induced during the cure, the causes are not well understood, nor are ways to alleviate the stresses.

One possible method of changing the interaction between the matrix and the fiber is to change the rate at which the polymer matrix is cured by increasing the cure heating ramp rate. This will also have the added effect of reducing the cycle times for production of each part and could lead to the widespread use of composites into new areas, such as automotive. However, before the effect of cure heating ramp rate on complex composite structures can be studied and understood, consensus must first be reached on a cure heating ramp rate dependence. At the time of this writing, there is little literature and less agreement on the existence of cure rate dependence for epoxy/amine base thermoset polymers.

Cure Rate Dependence

In order to understand if a cure heating ramp rate dependence for thermoset matrix polymers of epoxy/amine chemistry exists, the latter half of this dissertation will be focused on solving that problem. However, before the results are discussed, it is important to understand the variables that will influence any cure heating ramp rate dependence. The most important of these factors are network polymer architecture, the formation of said architecture, isomerization of amine monomers, and functionality of epoxide monomers. Additionally, current research in this area will be presented, and properties that may possibly have a cure heating ramp rate dependence will be discussed.

Network Architecture

For thermoset matrix polymers, the term “network architecture” is used to describe the three dimension arrangement of monomers in space, especially their orientation after the polymer has been completely cured. The size scale associated with

the network architecture of the polymer is on the order of tens to hundreds of angstroms. This topic has been the focus of considerable work in the Wiggins Research Group over the last several years and is hypothesized to be greatly altered by the cure heating ramp rate.[4,5] It is believed that the cure kinetics will be significantly affected by the cure heating ramp rate, because the ramp rate will alter the kinetics of the polymer, which is the primary influence for how the network architecture develops. Changes in the network architecture could be identified by free volume analysis, dielectric analysis, and possibly even macro-scale properties such as glass transition temperature and mechanical modulus.

Differences in the network architecture of various thermoset polymers typically arise from the chemistry. In the case of epoxy/amine thermoset polymers, side reactions such as etherification, or other factors such as electronics of the amine can influence the overall kinetics of the polymerization. In its most basic form, the reaction between an epoxy and an amine is described below in Figure 1. Nucleophilic attack by the primary amine will occur on the oxirane ring, resulting in a ring opening reaction generating a hydroxypropyl ether and secondary amine. The secondary amine can then ring open a second epoxide in a similar manner resulting, in the generation of a tertiary amine.[6,7] After the formation of the tertiary amine, it will act as a catalyst for the remaining reactions possible. It is also possible at high temperatures for etherification, or the ring opening of an epoxide via the hydroxypropyl ether linkage, to occur.[8,9]

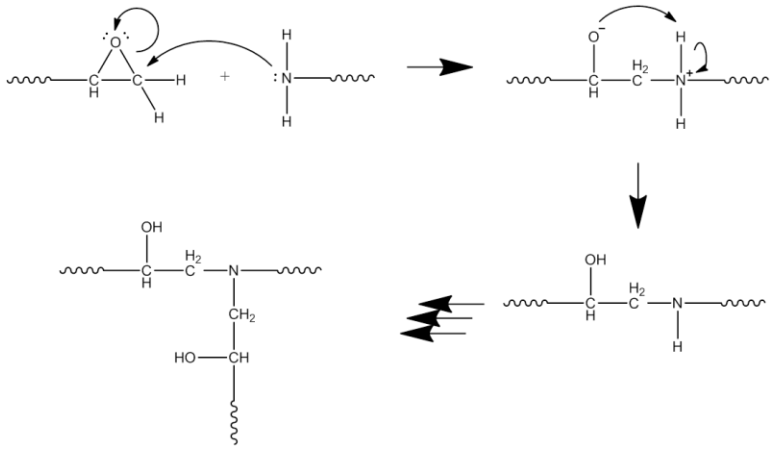

Figure 1. Mechanism of chemical reaction between an epoxide and amine.

As the molecular weight of the thermoset polymer builds, the solution transitions from a liquid to gel to glass solid state. While the monomers continue to react past the transition from liquid to gel phases, in some cases, the reaction may change kinetics as the mobility of the unreacted monomers is now hindered. The next transitional phase of the reaction is known as vitrification and occurs when the glass transition temperature of the polymer exceeds the curing temperature. Vitrification does not occur in all polymers. However, when it does, the network is effectively fully cured at that temperature. The gelation and vitrification stages greatly influence the network architecture of the polymer but are themselves controlled by the kinetics of the reaction. Because thermoset network polymers are intractable and insoluble by nature, the two main methods of analysis to observe the cure kinetics are near infrared spectroscopy and *in situ* dielectric spectroscopy.

Considerable work has been done in the Wiggins Research Group using near infrared spectroscopy (NIR) to characterize epoxy/amine thermoset polymers. Using NIR, concentrations of epoxide, primary, and secondary amine can be measured, allowing for conversion to be tracked. This can be done for a variety of epoxy and amine

chemistries and can provide valuable information for network formation. Specifically, the Wiggins Research Group has reported that, by variation of the amine curative and the temperature of cure, the reaction between the amine and epoxide can become preferential resulting in differences in network architecture. Shown in Figure 2 is a plot of concentrations versus time for a DGEBF/33DDS thermoset matrix. It shows a depletion of primary amine and a simultaneous increase in secondary amine. This suggests that the reaction conditions have made the primary amine reaction preferential at that temperature, meaning that the network architecture is different than other studied thermoset matrix polymers. This difference manifests itself as differences in glass transition temperature, mechanical properties, and free volume characteristics.[10,11]

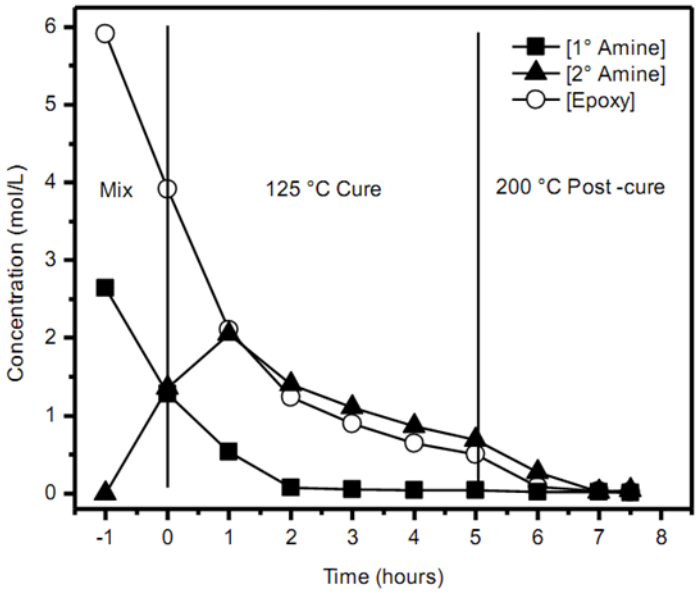

Figure 2. Concentrations of epoxide, primary, and secondary amine as measured using NIR. Reproduced with permission.[4]

Isomerization and Functionality

Network architecture is not only influenced by the type of cure but also by the monomers chosen to be incorporated into the polymer. Effects of amine isomerization and epoxide functionality have been found by the Wiggins Research Group to significantly alter the final thermal and mechanical properties of the matrix.[12] It would stand to reason then, that if the cure temperature and network kinetics govern any cure heating ramp rate dependence, the selected amine isomer and the functionality of the epoxide monomers may make any ramp rate dependence chemistry specific.

The effect of isomerization is best illustrated between the monomers 3,3'-diaminodiphenyl sulfone (33DDS) and 4,4'-diaminodiphenyl sulfone (44DDS). In the case of the meta substitution (33DDS), differences in primary and secondary amine reactivity have been found due to the electrostatics of the monomer.[4,13] Due to the electrostatic interactions with the sulfone withdrawing group, the 44DDS isomer does not suffer from differences in reactivity. Furthermore, it has been reported that this change in secondary amine reactivity has significant consequences on the final thermal and mechanical properties of the network polymer. For example, the fractional free volume and hole size free volume for these polymers are significantly different leading to variations in solvent ingress into the system.[14,15] At first glance, these differences in amine reactivity may not seem relevant to any cure ramp rate dependence the polymer matrix might have, but consider the following. It is known from previous work in the Wiggins Research Group that if enough thermal energy is applied to a 33DDS matrix during the cure, the observed differences in the network formation are eliminated.[4] Then, if the cure heating ramp rate was fast enough, it would be possible to change the nature of the 33DDS network growth profile as well, resulting in potentially significant differences

in the overall network architecture and resulting physical properties. This hypothesis is the main driving force for Chapter VII and the initial comparison between 33DDS and 44DDS containing matrix polymers.

The functionality of the epoxide has also been widely reported to alter the final thermal and mechanical properties of the polymer matrix material, from the Tg, to mechanical properties, to free volume characteristics.[16–18] The most significant impact of the incorporation of epoxide monomers of higher functionality (greater than two) is the impact on gelation and vitrification that lead to lower maximum conversions for these polymer networks.[19–21] It has been found that the conversion of a the tetra-functional epoxide TGDDM, can only reach approximately 70%.[22] However, the actual number for the maximum conversion can be varied between 60-75% based on the maximum curing temperature of the matrix polymer. Therefore, it is reasonable to propose that with the higher functionality epoxides, the final conversion may be dependent on the cure heating ramp rate of the polymer. This will be the focus of discussion in Chapter VII.

Arguments on Cure Rate Dependence

While there are several hypotheses proposed above as to how a cure heating ramp rate dependence might be influenced by isomerization, functionality, and network formation, there are a few areas relating to epoxy/amine thermoset polymers that have already been explored for a cure ramp rate dependence. Currently, there is little agreement in the literature as to the nature of any cure ramp rate dependence. The lack of agreement most likely relates to what properties are being studied and a lack of a systematic approach by polymer scientists, as a majority of the research done to this time relates to a mechanical properties approach, not a molecular level approach. The main areas of current work that will be discussed in this section, relate to the formation of

residual stresses within the matrix, and the study of cure ramp rate by DSC methods to determine differences in glass transition behavior.

A residual stress (or strain) formed within a matrix during polymer cure is inevitable. The formation of these stresses is due to the gelation and vitrification of the matrix polymers and is exacerbated by the inclusion of nanomaterials or fiber reinforcement.[23–25] The phenomenon is caused after vitrification when the polymer is still in the rubbery state (above Tg), the molecules have molecular motion, and are trying to reach a thermodynamic energy minimum. This is prevented, however, by physical constraints due to cross-linking.[26,27] When the polymer is cooled below the glass transition temperature, the thermodynamic state of the polymer is now locked due to restricted motion, leaving an inherent residual stress or strain that results in micro-cracking of the matrix polymer. Trappe and coworkers found that there was a connection between the cure rate and the propagation rate of these cracks within a polymer matrix.[28] Despite this connection, more work is necessary to determine a positive correlation.

Differential scanning calorimetry has probably been the most common tool to study any cure ramp rate dependence in the polymer matrix.[29] While it has been well established that the maximum cure temperature will alter the conversion and thermo-mechanical properties of the network, it is unclear if there is also a dependence on cure heating ramp rate.[30–32] Several research groups have conducted both isothermal and non-isothermal DSC studies to attempt to solve this problem; however, debate still exists.[18,19,33] Perhaps the most significant contributions to the question of cure ramp rate dependence have been made by Hardis et al. and Rosu et al. Hardis and coworkers used three techniques to study the cure kinetics and non-isothermal behavior of the networks: DSC, Raman spectroscopy, and DEA (DES). They were able to show that one uniform

mechanism exists throughout the entire reaction of the matrix polymer, and by tracking conversions, were able to show that the Tg for the matrix changes with degree of cure. While they did not specifically show any other dependencies between the ramp rate and the polymer properties, their work does suggest that a cure ramp rate dependence exists. Rosu and coworkers did a similar study; however, their primary focus was on the non-isothermal behavior of the matrix. Yet, in their study, they suggest that no ramp rate dependence exists.

Dielectric Spectroscopy

Dielectric spectroscopy (DES), sometimes referred to dielectric analysis (DEA), is a powerful tool for studying the molecular motions within thermoset polymer matrix systems. The Wiggins Research Group has been using DES to study the molecular motions that occur both at and below Tg for several years.[12] Additionally, DES has a long history in the study of molecular motions of polymers.[32,34,35] Despite the utility of dielectric spectroscopy, little to no research has been found that utilizes DES to study the effect the cure heating ramp rate on the molecular motions and molecular architecture of epoxy/amine thermoset polymers. Because of the unique ability of DES having the sensitivity to study very complex molecular motions, it will be extensively utilized in this dissertation and will be the focus of Chapter VI. Since DES is discussed in detail in this dissertation and is not widely applied in thermoset matrix analysis, a brief overview of the technique is included here.

There are two main methods of application for DES that are included in this dissertation. The first to be discussed, and by far the most common, is broadband-DES and the second *in situ*-DES. However, both methods rely on the same fundamental applications.[36] DES is essentially an analysis method that studies the relationship between

the sample and an alternating electric field and is in many ways analogous to dynamic mechanical analysis of a polymer. Similar to DMA, where a complex mechanical response exists, when the alternating electric field is applied to the polymer, there is both a real and imaginary component of the dielectric response.[37] The main advantage of the use of DES as opposed to DMA is the much larger frequency range of DES. Typical instruments can range from 10^{-6} to 10^{11} Hz.[38] This large frequency range allows for the observation of both very long and very short time scale molecular motions.[39–42]

A schematic representation of the sample setup for broadband-DES is shown in Figure 3. The polymer sample is typically 100-300 µm in thickness for a thermoset matrix polymer. An alternating current is applied to the polymer sample; an electric field is then generated within the sample, shown as field lines in the figure. Once the current is applied a dielectric response for that frequency is measured. In addition to the standard dielectric response, a charge build up at the interfaces between the sample and electrode can be formed.[43–45] This phenomenon is called electrode polarization and occurs most often at lower frequencies.[46]

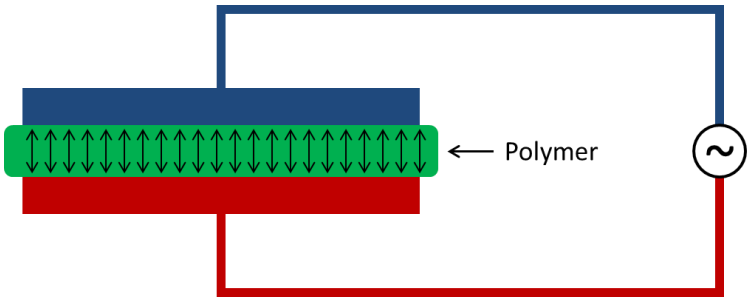

Figure 3. Experimental setup schematic for broadband DES.

Once a dielectric response is observed, typically either with respect to frequency or temperature, a series of analytical methods are then applied to understand the data. A

very common initial analysis is to plot the dielectric loss, ε", versus the frequency.[38] In this plot, a peak represents a relaxation event for the polymer, and an exact relaxation time for the event is determined via fitting the data with the Havriliak-Negami (HN) equation.[34,47] This fitting allows for the determination of a characteristic relaxation time, Advanced analyses can also be used to determine activation energy and distributions of these relaxations.[48] The specific functions and analysis methods are discussed in Chapter II.

The second type of DES to be discussed in this dissertation is *in situ* DES. While the fundamental principles governing the response of *in situ* and broadband are the same, there are two main differences.[35] First, the primary information tracked is not the dielectric storage or loss, but the ion viscosity. Ion viscosity for thermoset matrix polymers is related to the mobility of any ionic impurities that are present in the monomers during cure.[49,50] Ion viscosity is also proportional to the rheological viscosity of the polymer sample. The second difference between the two methods is that the sample geometry is no longer important. A schematic representation for the *in situ* method is shown in Figure 4. The design of the sensor alternates electrodes on one surface as opposed to two and can be used during a normal curing cycle. This electrode design allows for any geometry to be used, and the analysis can then be performed during the cure for the polymer matrix. In fact, almost any sample geometry can be used even with such constructions as a carbon fiber composite. For the analysis then, ion viscosity is usually plotted against temperature at a specific frequency and allows for a determination of the relative kinetic rate, gel point, and vitrification of the polymer matrix.

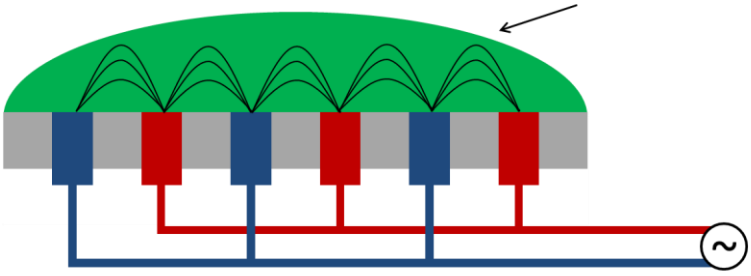

Figure 4. Experimental setup schematic for *in situ* DES.

Summary of Cure Rate Dependence

Based on the current available literature on the topic of cure ramp rate dependence for thermoset polymers based on epoxy/amine chemistry and the brief overview discussed above, this area is ripe for exploration and has garnered the attention of both academics and industrial scientists. Based on the above discussion, the following hypotheses are proposed and will be the basis for the cure ramp rate dependence portion of this dissertation:

1. A cure ramp rate dependence exists for these polymers and will be most apparent on a molecular level due to the nature of network architectural formation.
2. Any cure ramp rate dependence for epoxy/amine thermosets will be magnified when the amine monomer has different primary and secondary amine reactivity.
3. Higher functionality epoxides will also exacerbate any cure ramp rate dependence for these polymer networks.

These hypotheses will be explored by the thermal and molecular level characterization of a series of epoxy/amine thermoset network polymers prepared at various cure heating ramp rates.

Molecular Dynamics of Thermoset Polymers

Since their first implementation in the 1950's, molecular dynamics simulations have been realized as a means to create and understand the atom and how it interacts to form molecules. While computer power has progressed significantly since the first use of molecular dynamics, the general principles remain the same and will be the focus of this section. Before they are introduced specifically; however, there are two main themes that will be a point of reference for both the introduction and this dissertation as a whole. Firstly, molecular dynamics simulations allow scientists to understand the atomic and molecular levels. We can now visualize and understand complex molecular interactions that give rise to the macro-molecular properties we observe in nature every day.[51,52] And secondly, molecular dynamics simulations will quickly become a low cost, high throughput method of analysis for novel polymers as it has become in the field of pharmaceutics. [53]

Molecular Dynamics of Condensed Phase Matter

Originally, molecular dynamics simulations were performed only on gas phase matter; however, as they have matured, the ability to simulate condensed phase (liquid or solid) matter has been realized. There are several different process methods for the simulation of condensed phase matter, including quantum mechanical simulations, Density Functional Theory, Monte Carlo, *ab initio*, and empirical force field models. For the purpose of this dissertation, the focus of the introduction will be on empirical force field models that utilize both the Monte Carlo and *an initio* methods of simulation.[54,55]

While the specific process of modeling thermoset matrix polymers will be introduced in Chapter III, some instruction will be given here with the explanation of molecular dynamics simulations. Essentially, a molecular dynamics simulation of a solid phase material is done by designing your molecule in a visualization environment based with Cartesian coordinates assigned to each atom. Then, the atoms are related to one another using one of two approaches detailed below:

1. Monte Carlo Method

   In the Monte Carlo (or numerical best guess method), values for certain properties such as bond lengths, and angles are assigned to various atoms comprising the molecule. Then by applying a minor perturbation to one of the properties, a new potential energy is generated for the system. If the new potential energy value is less than that of the original, then the change is kept, else the original value is restored. This method is iterated sometimes hundreds of thousands of times until an energy minimum is reached.[56]

2. *Ab initio*

   The *ab initio* or first principles method, calculates values such as bond length, angle, etc., based on a series of empirical equations that are unique to the software system that has been utilized, and are generally related to approximations of the wave function(s). This type of calculation is in general more accurate, however, considerably more computationally expensive.

Each method has their drawbacks and molecular dynamics simulations usually use a combination of these methods in the calculations. Specifically, the Monte Carlo method suffers from an energy well trap. The best way to explain this trap is visually, and a representation of the problem is shown in Figure 5. The problem with the Monte Carlo method in this case is that there would be two energy minima. If the exact energy value were not the equivalent, then a false minima could be achieved that would cause errors to arise later in the simulation process. While there are programming safeguards in place to minimize this risk, it is still possible that this event could occur.

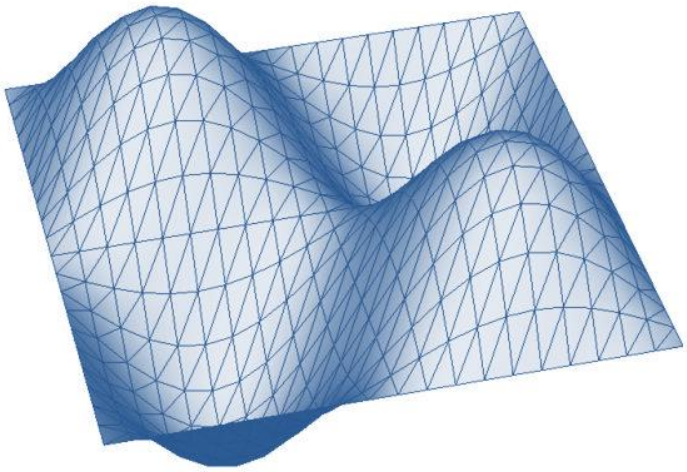

Figure 5. Energy well trap. $z(x.y) = \sin(2\pi x) * \sin(2\pi y)$.

As mentioned previously, the *ab initio* method generally suffers from a high computational complexity which consumes considerable computer resources during the calculation. To further complicate this problem, the scale between the number of atoms (or degrees of freedom) does not relate to the computing time in a linear fashion, but the time function is generally an $O(n^x)$ problem where x can vary between 2-5. As a result, the simulations will generally build the structure, then initially minimize the potential

energy based on a Monte Carlo calculation and then finalize the minimization using an *ab initio* calculation.

While for simulations on condensed phase matter generally use both a Monte Carlo and *ab initio* approach to calculate the results, there are a series of fundamental assumptions that must be satisfied to use these calculations. The assumptions are outlined below and will be discussed in detail in Chapter III:

1. Constant number of atoms
2. Constant pressure and/or constant volume
3. Forcefield selection
4. Electrostatic parameters

All of these are related to the precision and accuracy of the simulations as a whole. Additionally, there are several ways to refine the assumptions to either increase the precision and the computing time or decrease them.

Current Application

In light of how complex the calculations are to fully utilize molecular dynamics simulations, it should be no surprise that the development of these simulations for both polymers in general and specifically thermoset polymers has been an iterative process developed over many years.[52,57–60] In general, the research conducted in this field has followed this iterative approach by simulation of a system, analysis of differences between simulation and experiment, determination of cause of the differences, and refining of simulation.[61,62] This section will focus on the research leading to what was used for this dissertation.

Some of the seminal work for the full computational analysis of thermoset polymers was completed by Farmer and Varshney at the Air Force Research

Laboratories.[63] They were the first researchers to develop a full set of analysis protocols for the simulation of thermoset polymers, and moreover, were some of the first researchers to develop a mechanism to simulate the growth and formation. Their work on simulation of network formation consisted of an algorithm to determine if reaction should occur between two monomers. Essentially, un-reacted monomer was placed in a box of known size. If two monomers moved closed enough to each other during an energy minimization, the algorithm established that a reaction had occurred and a chemical bond was created between the two monomers. This would continue to progress until a desired cross-link density, molecular weight, or conversion was achieved. Farmer and Varshney were the first to utilize this approach and the first to place an emphasis on the number of atoms in the simulation. Before their work, most of the molecular dynamics simulations utilized only a few monomers (less than ten). After their work a larger simulation size was used (hundreds of monomers). [64–67]

Following the work done by Farmer and Varshney at the Air Force Research Laboratory, Boeing Research and Technology (BRT) began to implement molecular dynamics simulations for materials development as a mainstream process. As a result of this significant advancement in the simulation of thermoset matrix polymers, improvements were realized. The build procedure used by Christensen and coworkers at BRT was slightly different than that of Farmer, where they utilized a dendrimer type build approach. Essentially, the polymers were built generationally, as opposed to the reaction scheme as proposed by Farmer. It was found that this build approach did not alter the accuracy or precision of the final simulated results and operated much quicker than previous methods.[53,68] Furthermore, this type of simulation was validated and has been used in a variety of thermoset polymer simulations.[69]

One practical application of finally having a reliable simulation method is the simulation of new matrix polymer systems, either by means of new monomers or potential new nanomaterial additives. An example of this is collaboration between BRT and the Wiggins Research Group that involved the simulation of polyhedral oligomericsilsesquioxanes (POSS) and their molecular level dispersion in traditional aerospace epoxy matrix materials. Through this work, a significant enhancement in yield strain with no loss in modulus or Tg was realized, leading to an entire area of research for the Wiggins Research Group.[5,12]

Molecular dynamics can also be utilized to study the molecular level of a molecule and how that relates to the macro scale properties that are observed. While this will be a significant area of discussion in both Chapters III and IV, an example of such an occurrence is work done by Boyce and coworkers in the late 1990's. Boyce was able to study the molecular motions and events that occur on the nano-scale during applied material deformation.[56] She and her coworkers found that there was an increase in the potential energy when deformation occurs. Interestingly, however, she did not find a correlation between the applied strain and changes in bond length that would be associated with the breaking of chemical bonds. At the time it was unclear as to why this is the case, but in light of recent work done to simulate thermoset failure, it suggests that when macroscopic failure occurs very few chemical bonds are broken.[70]

While there are numerous examples of the capability of molecular dynamics simulations of thermoset polymers, two more specific examples are necessary to fully understand the cutting edge in this research. Molecular dynamics simulations are also being used to understand composites and how they behave to other stimuli, such as fluid ingress or how carbon fibers interact with the matrix material. Clancy et al. found that

fluid ingress could be modeled in these systems, and a knockdown in mechanical performance could be observed with the increase in moisture content in the simulation.[71] Strachan and coworkers found that by simulating a carbon fiber surface next to a matrix polymer, the direction of pull and surface orientation of the fibers began to influence the failure mode of the composite between adhesive and cohesive failure.[68]

These other uses for molecular dynamics simulations are especially important to discuss for two reasons. Not only can the molecular dynamics simulations be used to determine material properties and understand molecular level events, they can also be used to understand the complex interactions with other materials that, to date, require expensive and lengthy testing to conduct.

Future Direction

While it is impossible to predict the future, it is possible to propose one possible outcome for molecular dynamics. As computing power continues to increase, it may be the case that this method of analysis will be advanced even further, to the point where all experiments will begin with a molecular dynamics simulation, and then progress into the laboratory. I believe that rational molecular design will have a significant impact on the field of polymer science and is already beginning to.

Using these simulations, researchers in collaboration with The University of Southern Mississippi, the Commonwealth Scientific and Industrial Organization (CSIRO) of Australia, and The Boeing Company have already begun to design new monomers for thermoset epoxy/amine chemistries. Further, companies such as Cytec Advanced Materials have already begun to patent molecules based solely on their results from molecular dynamics simulations.[72,73] These simulations are the future. While I cannot

predict their exact course, they are not going away, and understanding how the simulations work will only be advantageous to future researchers.

Research Overview

The purpose of this dissertation at a global level is to discuss improvements in the understanding of the fundamental molecular level properties that drive the macromolecular performance of high performance thermoset epoxy matrix polymers. Specifically, the discussion in this dissertation will revolve around two areas:

1. The development and improvement of molecular dynamics simulations of thermoset matrix polymers and their use in understanding molecular response to applied strain deformation.
2. The investigation and discernment of a cure heating ramp rate dependence on the final molecular and macro-molecular properties on thermoset matrix polymers.

This work will build on previous advances in structure-property relationships of high performance epoxy/amine thermoset polymers that has been previously been reported in the Wiggins Research Group.

This dissertation is broken down into two primary sections, each focused on one of the two main themes presented above. The first section will begin by discussing the development of atomistic molecular dynamics simulations of thermoset epoxy/amine matrix polymers and conclude with the implementation of this work to determine a fundamental understanding of molecular level events that drive thermoset matrix polymer yield. This section is contained within Chapters III and IV of this work. The second section of this dissertation will focus on determining if a cure heating ramp rate dependence exists for thermoset matrix polymers based on epoxy/amine chemistry.

Chapter V will discuss the implementation of techniques such as NIR and DSC to determine network growth patterns and how these growth patterns alter the molecular level architecture of the polymer network. Molecular level characterization will be discussed in light of PALS data to determine the free volume hole size and its dependence on cure heating ramp rate. Chapter VI will continue the molecular architecture discussion with an in-depth analysis using two forms of dielectric spectroscopy. Finally, Chapter VII will conclude the cure heating ramp rate discussion with an introduction to a second epoxy/amine chemistry to deduce if the previous observations of cure heating ramp rate dependence were chemistry specific or valid for a variety of epoxy/amine thermoset polymers.

CHAPTER II

EXPERIMENTAL

Materials

For use in this work, high performance thermosetting polymer composite matrix materials were formulated from epoxy-amine chemistry. Based on their differences in primary and secondary amine reactivity, the isomers 3,3'-diaminodiphenyl sulfone (33DDS) and 4,4'-diaminodiphenyl sulfone (44DDS) were chosen as the amine curative components. The chemical structures of these amines are shown in Figure 6 and Figure 7, respectively. The epoxide components chosen for this work were diglycidyl ether of bisphenol-f (DGEBF) and tetraglycidyl diamino diphenyl methane (TGDDM). The chemical structures of the epoxides are shown in Figure 8 and Figure 9. DGEBF was chosen as a model compound for typical thermoset epoxides, and TGDDM was selected to study the effect of higher functionality on thermoset polymer properties. The specific formulations prepared will be discussed in further detail later in this chapter. The characterization and analysis methods utilized will also be discussed in this chapter.

Thermoset Amines

33DDS (Royce International, 97% purity, micronized), with a molecular weight of 248.3 g/mol and an equivalent hydrogen weight (EHW) of 62.08 g/eq, was dried in a vacuum oven at 50 °C for 24 hrs before use to remove any residual water present. The pKa of 33DDS as determined using Advanced Chemistry Development Software (SciFinder Chemical Search), is 3.16. The chemical structure of 33DDS is shown below in Figure 6.

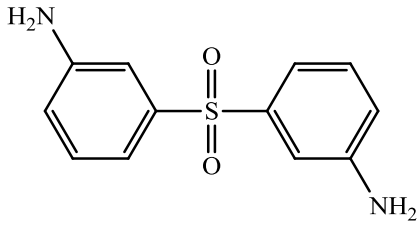

Figure 6. Chemical structure of 33DDS.

44DDS (Atul Sulpho, 97% purity, micronized), of molecular weight 248.3 g/mol and EHW of 62.08 g/eq, was dried in a vacuum oven at 50 °C for 24 hrs before use to remove any residual water present. The pKa of 44DDS as determined using Advanced Chemistry Development Software (SciFinder Chemical Search), is 1.24. The chemical structure of 44DDS is shown in Figure 7.

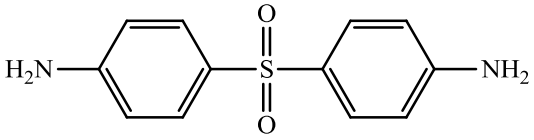

Figure 7. Chemical structure of 44DDS.

Thermoset Epoxides

DGEBF or EPON 862 (Hexion Specialty Chemicals), of average molecular weight 338 g/mol and equivalent epoxide weight (EEW) of 169, was used as received. The chemical structure of DGEBF is shown in Figure 8.

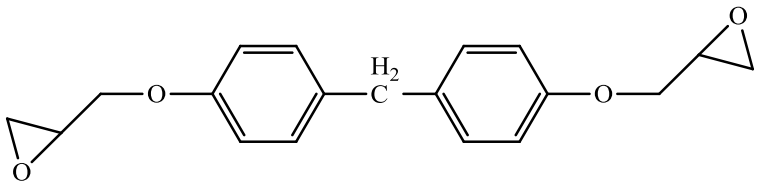

Figure 8. Chemical structure of DGEBF.

TGDDM (Hexion Specialty Chemicals), of average molecular weight 450 g/mol and EEW of 112.5 g/eq, was used as received. The chemical structure of TGDDM is shown in Figure 9.

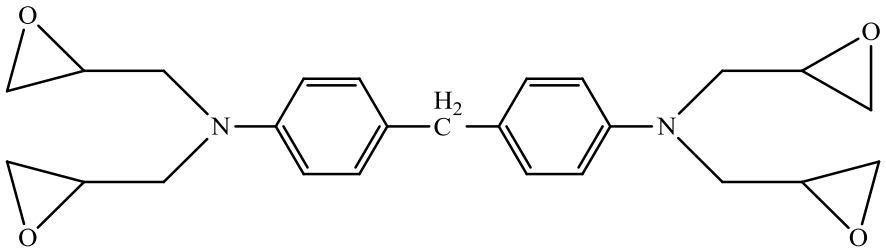

Figure 9. Chemical structure of TGDDM.

Characterization

Differential Scanning Calorimetry

Matrix thermal properties were conducted on a DSC Q200 (TA Instruments). All experiments were calibrated to Indium and Sapphire temperature and enthalpy standards, respectively. Additionally, in all cases, nitrogen was used as the purge gas. A series of DSC experiments were conducted throughout this work and will be described below:

1. Exotherm Intensity

   Dynamic DSC experiments were conducted to determine the exotherm intensity as a function of cure heating ramp rate. Samples were prepared by placing between 10–30 mg of uncured polymer within a hermetically sealed TZero® aluminum DSC pan. The samples were then heated from 35–180 °C, at ramp rates ranging from 1.0–65.0 °C/min. The heat of reaction, for an uncured sample (ΔH) was then taken as the integral of the exotherm peak.

2. Residual Exotherm

The residual cure was determined using a series of isothermal and dynamic DSC experiments. The samples were prepared as described previously. After heating from 35–180 °C, at variable ramp rates, the samples were held at 180 °C for 3 hrs. The residual exotherm energy was taken as the integral of the exotherm peak once the sample reached 180 °C.

3. Extent of Conversion

Extent of conversion was calculated by ramping the sample to 180 °C at a specified cure rate and holding at temperature between 0-180 min. The samples were then cooled to 35 °C and reheated at 10 °C/min to 300 °C. The integral of the second heating peak was calculated to determine ΔH_c, or the heat of curing for each ramp rate. The following equation was then used to determine the extent of conversion, α:[74]

$$\alpha = \frac{\Delta H_{uc} - \Delta H_c}{\Delta H_{uc}} * 100\%$$

The determination of ΔH_{uc} will be discussed in Chapter VII and is a standard value that is chemistry specific.

4. Glass Transition Temperature

T_g was determined using a Heat/cool/heat (HCH) experiment where a cured polymer sample is placed in a pan (as described previously) and heated to 300 °C, cooled to 35 °C, and heated again to 300 °C. The heating and cooling rates were held at 5.0 °C/min. The glass transition

temperature is determined from the DSC trace on the second heating cycle.

In addition to the standard DSC runs described above, advanced kinetics analysis was also performed using the acquired data. Because the analysis is utilized in several sections of this dissertation, the methodology will be described here.

Apparent activation energy, E_a, can be determined using exotherm data obtained at a variety of cure heating ramp rates. Typically, two approaches are used to determine the apparent energy of activation for a reaction, the Flynn-Wall-Ozawa (FWO) and Kissinger-Akahira-Sunose (KAS).[19,75,76] The FWO approximation for activation energy can be described as:

$$\ln(\beta) = -\frac{1.052E_a}{R} * \frac{1}{T} + A'$$

where β is the cure heating ramp rate, R the idea gas constant, T the temperature in Kelvin, and A' is a convoluted form related to the pre-exponential factor of the Arrhenius expression. The apparent activation energy is then determined from the linear regression of a plot of ln(β) vs T^{-1}. The KAS approximation is similar to the FWO approximation and is as follows:

$$\ln\left(\frac{\beta}{T^2}\right) = -\frac{E_a}{R} * \frac{1}{T} + A''$$

where all of the terms have their previous meaning, and A" is again related to the pre-exponential term of the Arrhenius expression. The apparent activation energy as determined from the KAS approach is calculated from the slope of the linear regression of a plot of $\ln(\beta/T^2)$ versus T^{-1}. It is generally accepted that the activation energy is between the values calculated by the two different methods.[75]

Density Determination

Density was determined using a Quantachrome Ultrapycnometere 1200e (Quantachrome) in collaboration with Deakin University in Geelong, Australia. The water temperature of the ultrapycnometer was 28.9 °C, with an internal pycnometer temperature of 23.0 °C. The volume of the reference cell was 12.7008 cm^3, and the volume of the sample chamber was 19.3291 cm^3. Density was determined with a standard deviation of 0.0002 g/cm^3. For the density calculation, the masses of five individual samples were measured, and the samples were then placed into the sample chamber. With a known mass, the volume was measured and density calculated.

Near Infrared Spectroscopy

Near infrared spectra in transmission mode were collected using a Nicolet 6700 FTIR (Thermo Scientific) with variable temperature cell in the range of 4000-8000 cm^{-1}. A white light source with a potassium bromide beam splitter and DTGS potassium bromide detector was used. Samples were prepared by placing, drop-wise B-staged polymer between two glass slides that are separated by a 0.8 mm Teflon® spacer. The samples were then reacted while in a Simplex Scientific Heating Cell. While heating, 32 scans at a 4 cm^{-1} resolution were acquired every 5 mins.

Positron Annihilation Lifetime Spectroscopy

Average free volume hole size and the relative intensity of o-Ps was determined with positron annihilation lifetime spectroscopy (PALS) on a fast-fast coincidence system, based on a system described by Olson et al., [77] with an average resolution FWHM of 290 ps. Sample disks were prepared as described in Section 2.1. A foil wrapped Na-22 source was sandwiched between two sample disks, wrapped in PTFE tape, and placed between two photomultiplier assemblies equipped with BF_3 scintillation

crystals, aligned coincident to the sample stack. Twelve spectra were collected for each sample at ambient conditions (23 °C, 45% RH) using a system based on an Ortec Positron Lifetime System (Advanced Measurement Technology, Oak Ridge, TN) over 1 hr to collect greater than 10^6 incidences. Coincidences were compiled using a multichannel analyzer. Spectra were analyzed for three lifetimes and intensities using PATFIT-88 software.[78] Assuming spherical holes, the average radius of free volume elements was calculated using [79]

$$\tau_{o-Ps} = 0.5\left[1 - \frac{R}{R_0} + \frac{1}{2\pi}\sin\left(\frac{2\pi R}{R_0}\right)\right]$$

where $\tau_{o\text{-}Ps}$ is the lifetime of the long lived o-Ps, R is the radius of the cavity, and R_0 is a constant 1.66 Å. The volume of the spherical hole is calculated as: $< v_h > = \frac{4}{3}\pi R^3$.

Broadband Dielectric Spectroscopy

Dielectric spectra were collected isothermally using a Novocontrol GmbH Concept 80 Broadband Dielectric Spectrometer over the frequency range 0.1 Hz-3 MHz and temperature range of -100-260 °C. Temperature stability was controlled to within ±0.2 °C. Samples were kept in a Humidity Control Chamber (Model 503-20, Electro-tech Systems, Inc.) with RH ≅ 5% at room temperature for at least three days prior to analysis to decrease the obscuring influence of water on the dielectric response. Sample discs of 2 cm diameter that were covered with two very clean aluminum sheets on both sides were sandwiched between two gold-coated copper electrodes of 2 cm diameter and transferred to the instrument for data collection.

To extract dielectric parameters, the Havriliak-Negami (HN) equation,[34,43] shown below, was fitted to experimental data:

$$\varepsilon^*(\omega) = \varepsilon' - i\varepsilon'' = -i\left(\frac{\sigma_{dc}}{\varepsilon_0 \omega}\right)^N + \sum_{k=1}^{3}\left[\frac{\Delta\varepsilon_k}{\left(1+(i\omega\tau_{HN})^{\alpha_k}\right)^{\beta_k}} + \varepsilon_{\infty k}\right]$$

ε' and ε'' are the real and imaginary dielectric permittivities, respectively, and i = $\sqrt{}$-1. There are three relaxation terms in the sum, and the term on the left accounts for dc conductivity, ε_0 = vacuum permittivity, and $\omega = 2\pi f$. For each relaxation term *k*, the dielectric strength $\Delta\varepsilon_k = (\varepsilon_R - \varepsilon_\infty)_k$ is the difference between ε' at very low and very high frequencies, respectively. σ_{dc} is dc conductivity, and the exponent *N* characterizes conduction in terms of the nature of charge hopping pathways and charge mobility constraints.[45] α and β characterize the breadth and degree of asymmetry, respectively, of ε'' vs. ω peaks. The Havriliak-Negami relaxation time τ_{HN} is related to the actual relaxation time τ_{max} at loss peak maximum at f_{max} by the following equation:[35]

$$\tau_{max} = \tau_{HN}\left[\frac{\sin\left(\frac{\pi\alpha\beta}{2(\beta+1)}\right)}{\sin\left(\frac{\pi\alpha}{2(\beta+1)}\right)}\right]^{\frac{1}{\alpha}}$$

The dc term in the first equation accounts for inherent or unintended (impurity) charge migration that is often subtracted to uncover loss peaks or at least make them more separate.

Sample disks of consistent thickness were prepared using a specific procedure developed and maintained throughout all formulations. Specifically, B-staged thermoset polymer (prepared as described in the Thermoset Polymer Synthesis portion of this chapter) was placed drop-wise onto a 12” x 12” x ¾” aluminum plate with Teflon® sheet

coating 0.08” thick. A similar aluminum plate was then placed on top of the polymer. A schematic is shown below in Figure 10. The entire assembly was placed in the oven for curing. Between 10-20 g of pre-polymer was used, resulting in films approximately 200 μm in thickness. After completion of cure, disk geometry was obtained using a 2 cm diameter die punch.

Figure 10. Schematic representation of DES sample apparatus. Blue rectangles represent aluminum plates, red represent Teflon® sheets and green represents the pre-polymer.

in situ Dielectric Spectroscopy

in situ dielectric spectroscopy (IS-DES) experiments were conducted using Netzsch Instruments interdigitated electrodes in conjunction with a 3 m portable sensor unit. These sensors are covered with a droplet of B-staged matrix polymer and cured using the standard process. The IS-DES experiments were designed to monitor the polymer cure in real time by determining ion viscosity as a function of either cure time or cure temperature. Ion viscosity (IV) is a measure of the ion mobility in the uncured polymer and is related to polymer chain mobility (and thus rheological viscosity). For thermoset matrix polymers, these ions can be either impurities or highly polarizable chemical units on monomers. IV is not directly measured but derived from the dielectric loss (ε”) using the following equation:

$$IV = \frac{1}{\sigma} \ where\ \sigma = 2\pi f \varepsilon'' \varepsilon_0$$

where f is the frequency, and ε_0 is the electrical permittivity in vacuum. While it is not necessary to have a sample of fixed thickness, all samples were approximately 300-400 μm thick.

Thermoset Polymer Synthesis

Difunctional Cure Rate Dependence

Matrix polymers were synthesized by adding epoxide (DGEBF) into an Erlenmeyer flask with a vacuum fitting and magnetic stir bar. The epoxide was then heated to 65 °C, and a vacuum of approximately 10^{-3} torr was applied to remove any air, water, or solvent impurity present in the epoxide. After degassing was complete, vacuum was removed, and amine was added to the reaction vessel. The amount of amine added varied by formulation; however, in all cases, the ratio of epoxide concentration to active amine hydrogen was maintained at 1:1. In a typical reaction of DGEBF epoxide and 33DDS amine, approximately 70 g epoxide and 26 g amine were used. After the amine was added, the system was vigorously stirred to mix the amine and epoxide components and vacuum was reapplied. After no residual gas evolved from the reaction flask, the temperature is raised from 65 °C to the dissolution temperature of the amine (approximately 125 °C). Upon amine dissolution in the epoxide, the matrix polymer was cast into various geometries for curing. To cure, formulations were heated from 35 °C to 180 °C, at variable ramp rates and held for three hours at 180 °C. Matrix polymers were prepared with varying heating ramp rates ranging from 1.0 – 25 °C/min.

Multifunctional Cure Rate Dependence

Thermoset polymers containing TGDDM and 33/44DDS were prepared in a similar manner to the difunctional matrix polymers. Again, ratio of epoxide concentration to active amine hydrogen was maintained at 1:1. A typical reaction for TGDDM and

33DDS would utilize approximately 131 g epoxide and 72 g amine. Polymers for each 33DDS / TGDDM and 44DDS / TGDDM were prepared at the following cure heating ramp rates: 1.0, 2.0, 5.0, 10.0, 15.0, and 20.0 °C/min. (DSC samples were also prepared for 45.0 and 65.0 °C/min.

CHAPTER III

DESIGN OF THERMOSET POLYMER MOLECULAR DYNAMICS SIMULATIONS

Molecular Dynamics

Molecular dynamics simulations of materials are computer simulations that relate atoms and molecules to one another using Newton's laws of motion. In the earliest molecular dynamics simulations conducted in the 1950's by Alder and Wainwright, particles were treated as hard spheres within a defined space and with a set velocity.[55] A perfectly elastic collision between the two spheres was modeled. As time has progressed, the computations have become more complex and now allow for much larger systems that can account for individual atoms and the effect from their electrons.[54] This is called an atomistic or atomistically explicit approach.

There are two different approaches often employed in molecular dynamics modeling, *ab initio* and Monte Carlo simulations. In *ab initio,* or first principles simulations, the properties of the system are calculated from fundamental thermodynamic equations of state, and are typically applied when determining the potential energy of the system. Monte Carlo, or numerical best guess, simulations are where the properties of a system are estimated using empirical data and then the variables (such as Cartesian position or bond length) are perturbed slightly. This process is typically repeated hundreds or thousands of times until an optimized solution is achieved.[80] Despite their differences, in atomistic simulations larger than 100 atoms, both techniques are commonly used. The most common implementation of the Monte Carlo method is when determining the bond length and bond angle between atoms in a molecule. The Monte Carlo approach tends to require less time to complete, with solutions that are comparable to those which would be achieved in an *ab initio* calculation. *Ab initio* calculations are

typically employed when it is necessary to determine properties such as the potential energy of a molecule. Quickly, these simulations can become very computationally expensive (requires excessive computer time) because the relationship between the number of atoms in a system and the time required to complete the calculations does not scale linearly. As mentioned, to reduce the computational time, both *ab initio* and Monte Carlo simulations are employed, but the complexity of the calculations can be further reduced by the utilization of a the Born-Oppenheimer approximation. Rather than explicitly defining the contributions of electrons of each atom, the electrons' effects are averaged over the entire molecule. While this approximation does introduce a source of error in the calculations, the error is reduced by the application of a force-field. A force-field is essentially a correction for the electron effects and typically includes experimental data that further refines the simulation. Additionally, a force-field is employed to correct for any other interactions that could occur between molecules such as van der Waals forces, hydrogen bonding, or other long-range interactions.

After the way the particles are related to one another is defined in the simulations, properties such as modulus and glass transition can be determined. The properties are simulated by introducing a small perturbation to the system on an extremely small time scale (typically fempto- or pico-seconds). This is done for an "infinite" number of times, and the property is determined by a time average of the properties,

$$A_{avg} = \lim_{\tau\to\infty} \frac{1}{\tau}\int_{t=0}^{\tau} A(t)dt \cong \lim_{M\to\infty} \frac{1}{M}\sum_{i=1}^{M} A(t_i)$$

where A is the desired property and is a function of the force-field of the simulation.[55] Figure 11 illustrates the perturbations of gas molecules over time and would be used to simulate a property such as the pressure of the system at a given temperature.

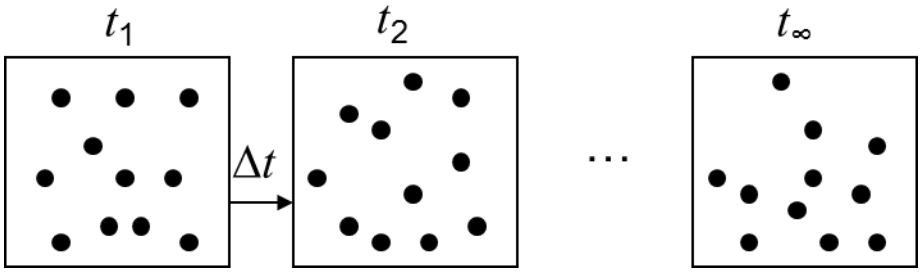

Figure 11. Perturbation of spheres over time for an infinite number of time steps.[55]

Despite the complex nature of molecular dynamics simulations and the limitations of current computer power, atomistic simulations of materials provide a pathway for low cost, high throughput analysis of materials. Molecular dynamics simulations can also be used to provide insight into areas of atom level interactions that could not be explored otherwise.

Computational Methods

Process Overview

To accurately perform molecular dynamics simulations of thermoset epoxy/amine polymers, it is necessary to follow a specific order of operations to ensure that the simulations are as realistic as possible. Without proper simulation generation, the thermal and mechanical properties simulated will not be meaningful or reproducible. While each of the steps will be discussed in detail over the course of this chapter, the general process for the creation of a realistic polymer model are as follows:

1. Generation of desired monomer(s)
2. Simulated “synthesis” of the polymer
3. Population of periodic repeat structures (amorphous cells)
4. Virtual annealing processes and density verification
5. Thermo-mechanical property modeling

Successful completion of these steps to form an accurate molecular dynamics model of a thermoset polymer yields a considerable amount of information about the polymer, including: glass transition temperature, thermal expansion behavior, and stress/strain response. All simulations were conducted using Materials Studio® version 6.1 and the Condensed-phase Optimized Molecular Potentials for Atomistic Simulation Studies (COMPASS) force-field, which is a commercially available platform that can be obtained from Accelrys Inc.

Monomer Generation and Modification

One of the predominant benefits of molecular dynamics simulations is the ability to accommodate a large number of different chemistries in a cost effective and efficient manner. Through these simulations, it becomes possible to study how systematic molecular changes can impact macromolecular performance or even to determine if synthetically complex monomer syntheses are worth the effort to attempt. To realize this goal, the monomer to be simulated must first be generated in the software. In general, a monomer is generated in the following manner:

1. Draw the molecule
2. Modify the molecule to simulate chemical “reaction”
3. “Type” the molecule to define partial charges and then define charge groups
4. Define the monomer connectivity
5. Define the monomer backbone atoms

The first step, drawing an atomistically explicit representation of the molecule to be simulated, is a straightforward process similar to other software platforms, such as ChemDraw®. “Ball and stick” representations of a typical high performance thermoset

amine (44DDS) and epoxide (DGEBF) are shown in Figure 12. Due to a drawback with how the software currently simulates polymer development, it is necessary to slightly modify the monomers. Specifically, the polymer development algorithm cannot tolerate changes in partial charges of the atoms. Thus, the monomer must be "pre-reacted." This is achieved by ring opening of the epoxide monomers and replacing the amine hydrogen atoms with methyl groups. Modified 44DDS and DGEBF monomers are shown in Figure 13.

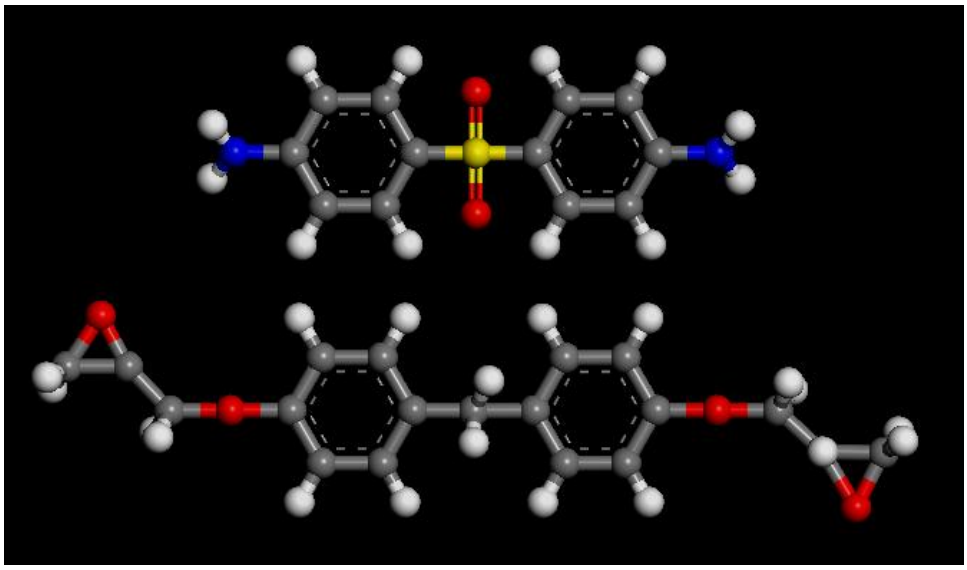

Figure 12. "Ball and stick" representation of 44DDS (top) and DGEBF (bottom) using Materials Studio®.

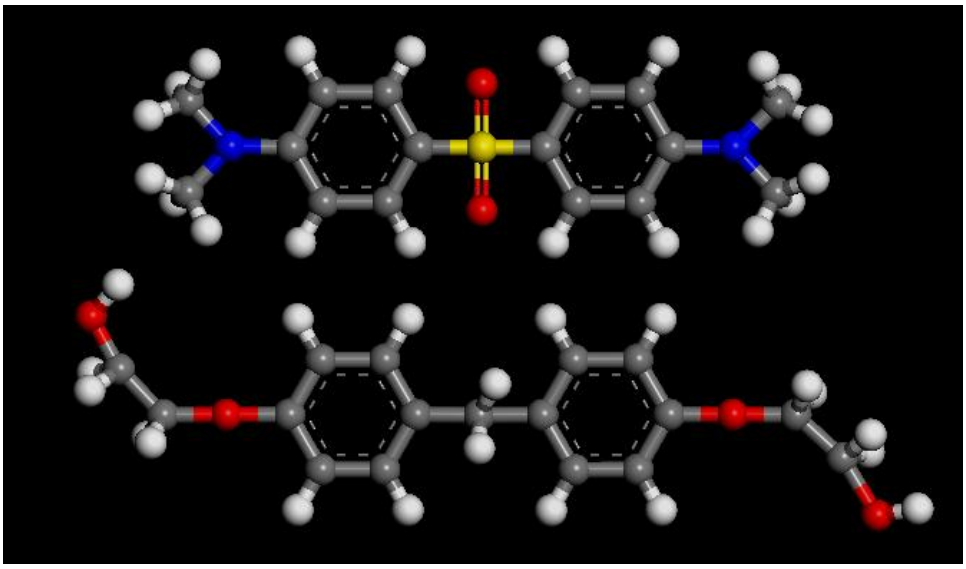

Figure 13. Modified “ball and stick” representations of 44DDS (top) and DGEBF (bottom).

The third step in the monomer creation process it to define explicitly the partial charges of each of the monomer atoms. Using the COMPASS® forcefield, the software will calculate the charges automatically for every monomer atom. Before this can be accomplished, however, the hydrogen atoms that will serve as connection points between atoms must be assigned their partial charges independently of the other atoms. Again, this is to prevent any significant changes in the overall partial electrostatic charge of the resulting polymer molecule. Typical values for the partial charges on DGEBF atoms are shown in Figure 14.

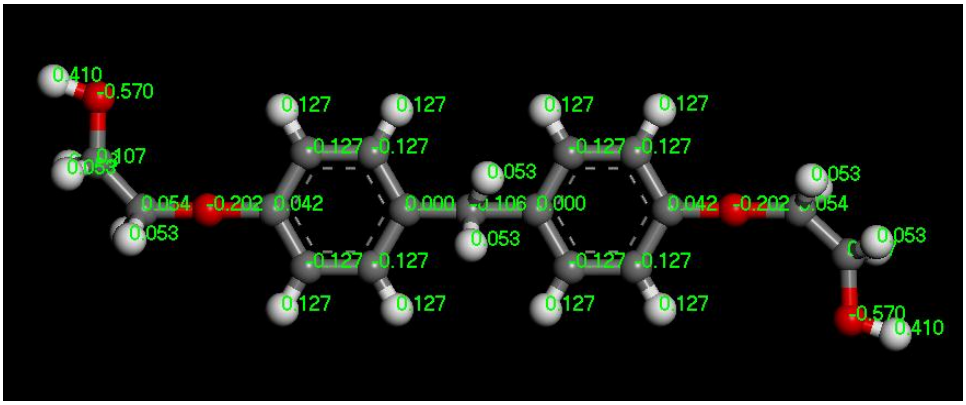

Figure 14. Assigned partial charges on DGEBF (modified structure) atoms.

From the assigned partial charges, charge groups are created. This is a manual process the user must define for all atoms in the molecule. Charge groups are defined for several reasons; however, they are predominately defined to improve the accuracy of the simulation calculations.[54,55] During the simulations, when one atom may interact with other atoms, the software will only include interactions up to a certain distance from the parent atom. (The Materials Studio® default cut-off distance is 9.5 Å.) In defining the charge groups, if any atom in the group is within the cut-off distance of the parent atom, the simulation will include the interactions of all atoms in the group. The more polar groups that are included in the monomer, the more important charge group definition becomes. A common assignment for charge groups on 44DDS is shown in Figure 15, where the top image is colored by atom and the bottom image is colored by charge group. Specifically, a charge group is defined as the smallest collection of connected (bonded) atoms where the sum of the partial charges is zero. This is best illustrated by direct comparison of the partial charges shown in Figure 14 and the charge group definitions in Figure 15.

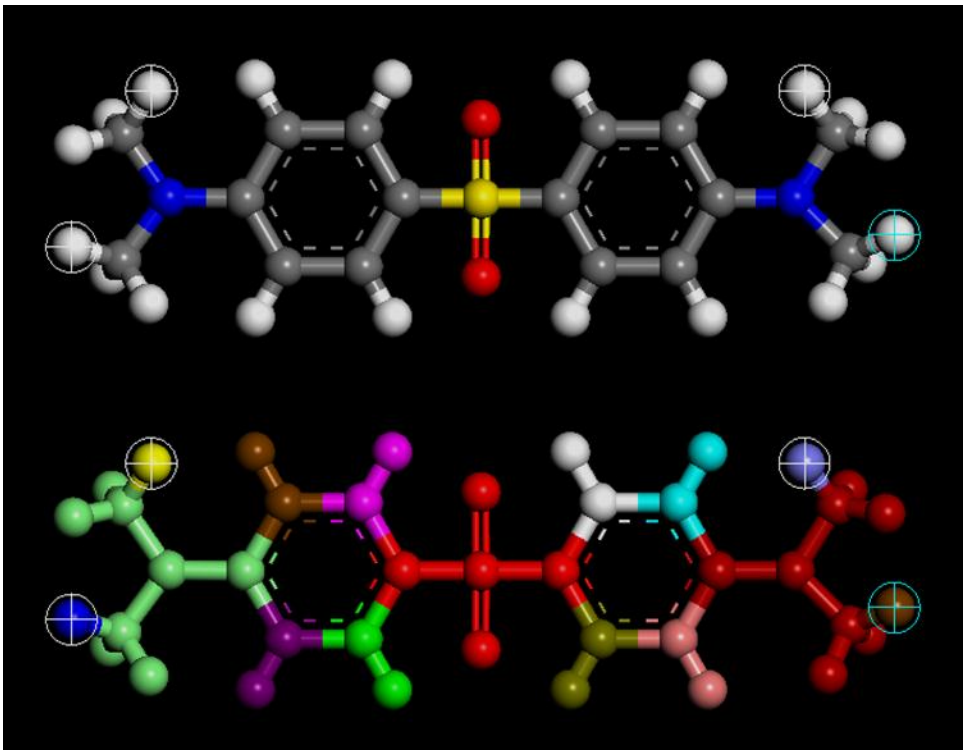

Figure 15. Monomer charge group definitions. Top represents color by element; bottom is color by charge group.

The final two steps in the monomer generation process deal with establishing the connectivity of the monomer. The first of the two steps is to define the connection point(s) of the monomer. By software convention, one point must be the head atom, and the remaining are defined as connection points. For the purposes of these simulations, hydrogen atoms are always used as the connection points. To form bonds between the two monomers, the connection points (hydrogen atoms) are removed, and a covalent bond is formed in their place. The remaining step in the monomer construction process is to establish the atoms that will be incorporated into the backbone of the resulting polymer. The backbone atoms must include the connection point(s) and all atoms between them. An example of backbone definition is shown in Figure 16.

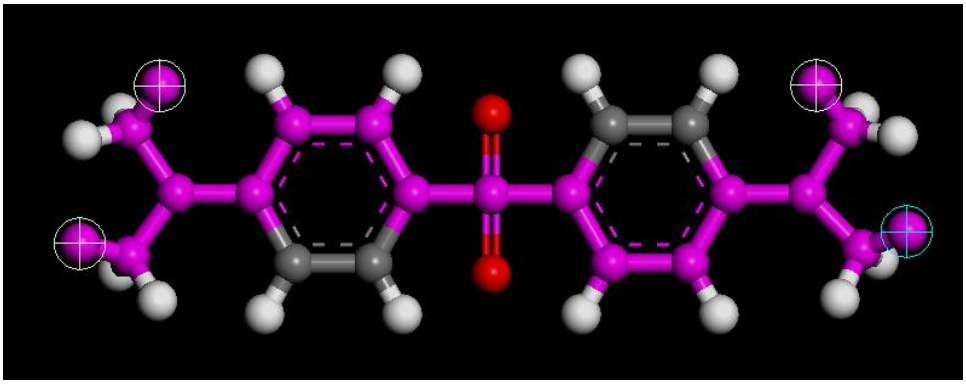

Figure 16. Connection point and backbone atoms assignments for 44DDS.

Matrix Simulation Generation

Once the monomers are prepared, the polymer creation and simulation process can begin. The first step in the polymer simulation is the computational "synthesis" of the polymer. The synthesis utilizes a script to create a final polymer structure. In the script, the monomer stoichiometry and molecular weight are input by the user. While the simulations can accommodate polymer containing multiple amine and/or epoxides, typically only polymers with a single amine and epoxide are prepared. Additionally, polymer systems simulated are kept with equal numbers of amine protons and epoxide rings (on stoichiometry). To optimize simulation time and still maintain simulation validity, the polymers simulated are restricted to a maximum of 8,000 atoms. This number of atoms reduces the required simulation time to approximately two weeks from start to completion. The script formulates polymers by addition of monomers over a series of generations, similar to how a dendrimer would be prepared. A representation of a typical polymer "synthesized" *in silico* is shown in Figure 17 below.

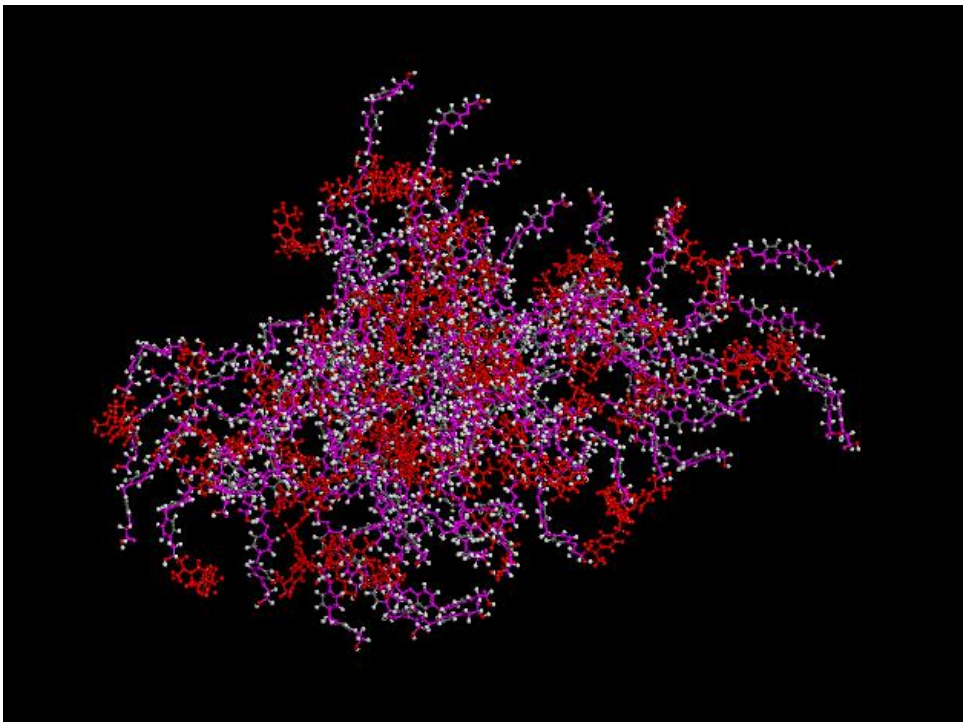

Figure 17. Polymer structure after simulated "synthesis."

One of the major assumptions in molecular dynamics simulations is that the simulated environment be in a periodic structure, usually in the shape of a cube. Every face of the cube, or cell, is attached to another cell identical in composition to the original. This is used to satisfy another assumption in molecular dynamics simulations that there are a constant number of atoms in each cell. If one atom were to be moved out of the cell during the simulation, an identical atom would be moved into the simulation cell from an adjacent repeat structure. This phenomenon is best illustrated by comparison of the same cell using different views. The left cell in Figure 18 shows the default polymer view, while the right cell of Figure 18 shows the in-cell view. Both are the same polymer and the same system; however, the in-cell view shows how the simulation would "see" a cross-section of the polymer during the simulation. Ultimately, how the polymer is viewed and which specific cell the atom comes from makes no difference to the simulation because the simulation is performed on condensed matter.

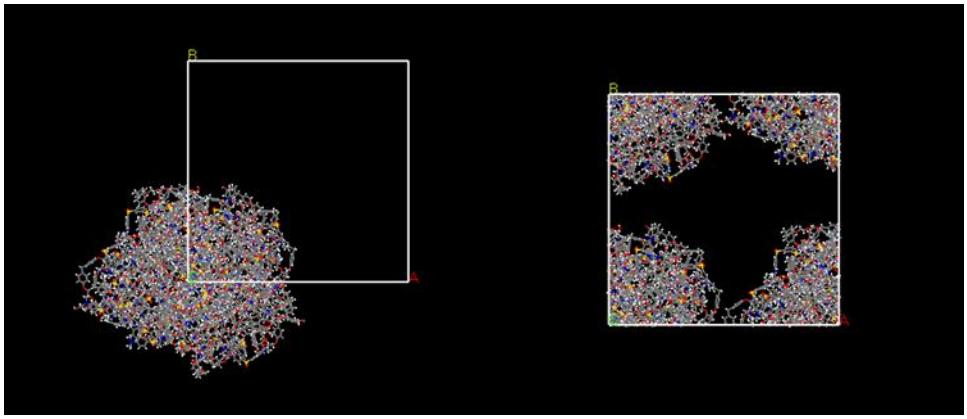

Figure 18. Amorphous cell views: left is default polymer view and right is the in-cell view.

The periodic structures, or amorphous cells, are simulated using the following specifications: one polymer per cell, a temperature of 298 K, a density of 0.4 g/cm^3, and a total of ten polymer configurations. During the building of the periodic structure, the density was ramped from an initial density of 0.01 g/cm^3, and all of the polymers in the created cells were checked for ring catenations (ring spearing) before qualification. Structures containing catenations were removed from the simulation. From the created configurations, the three lowest energy configurations were used independently for all of the remaining calculations, allowing for three replicates of each simulation. After amorphous cell creation, the bond lengths and bond angles for the polymer structures were optimized using a Discover Geometry Optimization with a maximum of 200,000 iterations. This step is necessary to prevent large changes in the potential energy of the polymer during the first step of the annealing process to follow. Any large energy deviations will cause the simulation to error.

To obtain a polymer structure that is used for thermo-mechanical property simulation, the polymer must first be annealed. After annealing, the simulated polymer should have an appropriate density. Verification of a realistic material density is the main

method of simulation validation. The annealing process is simulated using a series of constant volume and constant pressure dynamics simulations. The constant volume or isothermal-isochoric-constant number of particles (NVT) and constant pressure or isothermal-isobaric-constant number of particles (NPT) simulations increase the temperature of the simulation environment from 298 K to 650 K and decrease back to 298 K. Simultaneously, the pressure was increased from atmospheric to 0.1 GPa and reduced back to atmospheric. Then, a final constant energy or isochoric-isoentropic-constant number of particles (NVE) process equilibrates the structure at 298 K and atmospheric pressure. The final NVE dynamics are done to ensure no large changes in volume that would occur if the system was not properly equilibrated after annealing. Should a system that was not fully equilibrated be identified, the system would undergo the entire annealing process again to obtain energy/pressure/volume equilibration.

The annealing process is done to mimic the energy that would be added to the polymer during a physical curing and to remove any residual internal stress from the simulated system. [63] At the conclusion of the annealing process, the density of each of the cells should be approximately the density of the actual polymer. Typical densities are approximately 1.2 g/cm^3.[59,63,81] A representative image of the polymer structure before and after annealing are shown in Figure 19, and a series of simulated densities are shown in Table 1.

Table 1

Simulated densities after annealing with the standard protocol

Epoxide	Amine	Simulated Density g/cm^3
DGEBA	44DDS	1.202
DGEBF	44DDS	1.238
TGDDM	44DDS	1.214
DGEBF	APB-133	1.205

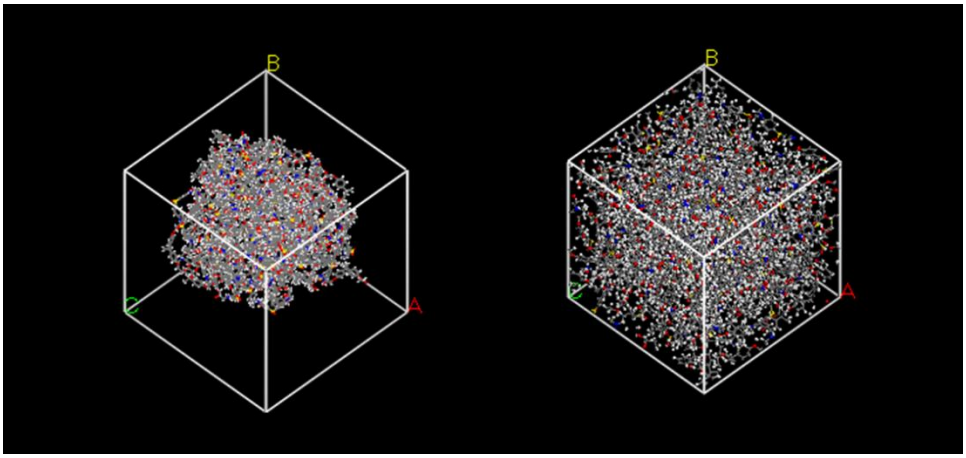

Figure 19. Thermoset polymer structure before (left) and after (right) the simulated annealing process. Density before annealing is approximately 0.4 g/cm^3; density after annealing is approximately 1.2 g/cm^3.

Matrix Analysis

Glass transition temperature, T_g, of the polymers is calculated from a pressure-volume-temperature cycle, analogous to the experimental technique of pressure-volume-temperature goniometry. During the temperature cycle, the polymer is held at atmospheric pressure, heated/cooled at a constant ramp rate, and the volume is recorded. The temperature cycle is as follows: ramping from 100–800 K and then back down to 100 K. From the data, a volume versus temperature curve, at constant pressure, is

generated, and the average of the heating and cooling runs for three trials is reported. A representative volume versus temperature plot for 44DDS/DGEBF is shown in Figure 20.

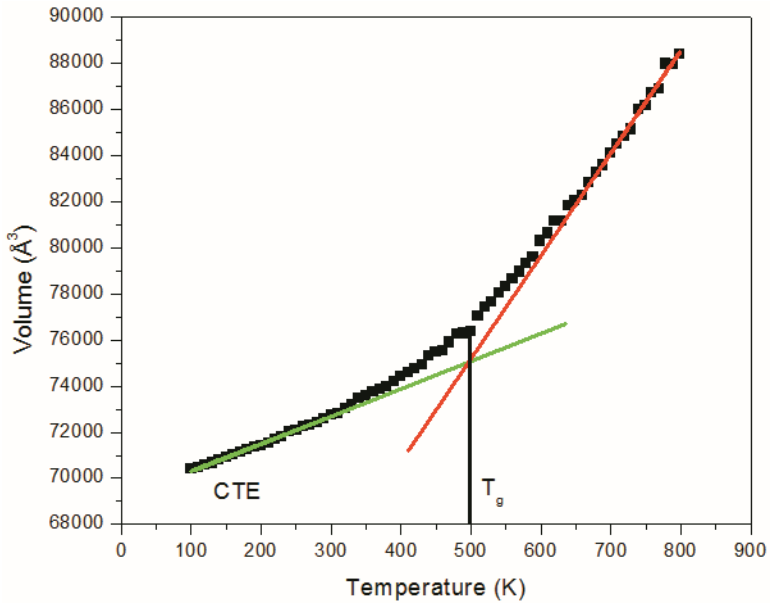

Figure 20. Volume vs temperature plot (at constant pressure) for a 44DDS/DGEBF polymer matrix.

From this plot, the T_g and the linear coefficient of thermal expansion (α) for the glassy state are determined. α is taken to be the slope of the heating portion of the curve that is below the glass transition temperature (see Figure 20). T_g is taken as the intersection between a linear fit of the regions below and above T_g (see Figure 20). There is a distortion in the data around the glass transition temperature, and the characteristic bend in a PVT curve is not seen, due to the relatively fast heating rates required to reduce the simulation time to a manageable length of approximately two weeks for this analysis.

Values for tensile, bulk, and shear moduli, as well as Poisson's ratio, were simulated using a software function called static elastic property determination. The analysis was performed according to software specifications and functions by indicating a small stress and observing the response. This method is applied using a tensile, shear, and

compressive stress independently of one another. From the response the Lamé constants are determined, and moduli values calculated. [65,82] It is important to note that the induced stress is sufficiently small, to ensure the simulation and analysis occurs in the linear (elastic) region of typical polymer visco-elastic response.

Typical values for the mechanical analysis of a polymer are displayed in Table 2. The results show how the tensile and shear moduli, as well as the first invariant of the strain tensor (measure of dilatational ability) and the coefficient of thermal expansion, vary with a decrease in molecular weight between crosslinks. From this information, it was identified that by reducing the molecular weight between crosslinks, the tensile modulus was increased (Figure 21).[62] This observation is expected as a reduction in molecular weight between crosslinks would increase the crosslink density, which has been previously identified to improve the tensile modulus of the material.

Table 2

Simulated mechanical properties for a series of molecular weights between crosslinks

Epoxide Chain Extension	Tensile Modulus, E	Shear Modulus, G	Strain Invariant, J_1	CTE, α
	GPa	*GPa*	---	*cm/cm/°C*
1.25	4.61	1.75	0.031	23.11
1.20	4.77	1.79	0.038	23.26
1.15	4.77	1.8	0.031	22.66
1.05	4.83	1.82	0.027	22.17
1.00	4.96	1.89	0.028	22.89

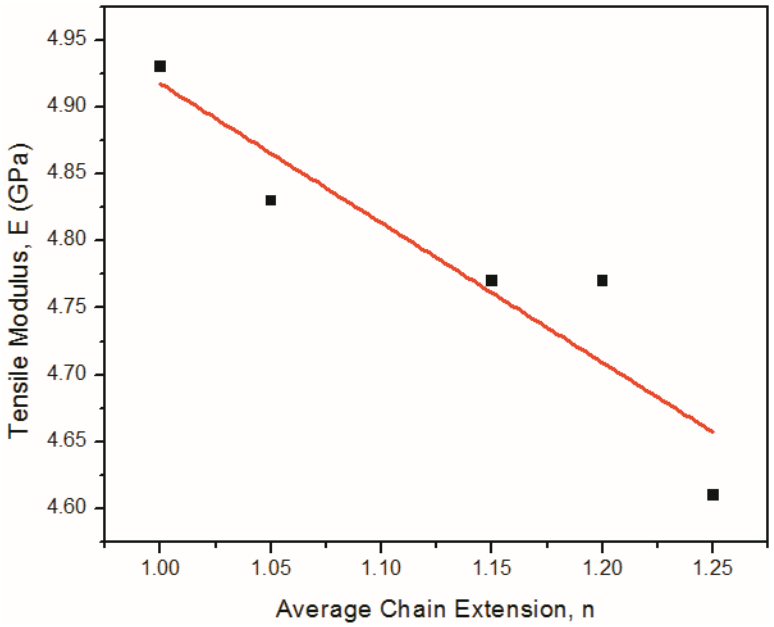

Figure 21. Average tensile modulus of a 33DDS / DGEBA based matrix as a function of average chain length of DGEBA (n). $R^2 = 0.8174$, linear fit.

Stress/strain behavior of the polymer matrix was simulated using a strain controlled approach. The strain controlled simulation process works by either increasing (tension) or reducing (compression) the cell size in the direction of strain. Then, using the Poisson's ratio determined from the previous set of simulations, the two non-principle axes' sizes are adjusted appropriately. A typical Poisson's ratio for this class of material is 0.35. The simulations cannot be performed in a continuous manner, as their analogous experimental technique would, and must instead be performed using a series of discrete intervals. To balance simulation time and useful data resolution, a strain increment of 0.1% was used. The strain was incremented every 7 ps, which results in an effective strain rate of 1.4×10^8 s^{-1}. This process was repeated for all three principle directions (x, y, and z) of the material and averaged. Anisotropy of the polymers are assumed.

A simulated stress/strain curve for a dual epoxide system, containing both DGEBA and DGEBM, is shown in Figure 22. The figure presented is very typical of a

simulation stress/strain curve for thermosetting polymers. Typically, these simulation stress/strain curves do not start at zero values for stress/strain; this is associated with the limited number of atoms used in the simulation. As the simulation size increases, the initial stress/strain values go to zero.[69] It is proposed by the author that, at the small simulation sizes, the residual strains from the simulated cure may not be entirely anisotropic, as assumed during the simulations. In addition to this source of error, in the high strain component of the simulations, the values obtained are most likely inaccurate. This is due to the inability of the simulations to accurately predict material failure and may lead to a distortion of the stress/strain curve at high strain values. Despite these two sources of error, these simulations can effectively simulate the strain at yield of a thermoset polymer, which is the desired component of these simulations. The yield behavior is of importance because it is used as a measure of the ability of thermoset polymer to fail in a distortional mode as opposed to a dilatational mode. [53] The yield point is determined using a polynomial fit of the stress/strain curve and setting the first derivative of the polynomial to zero.

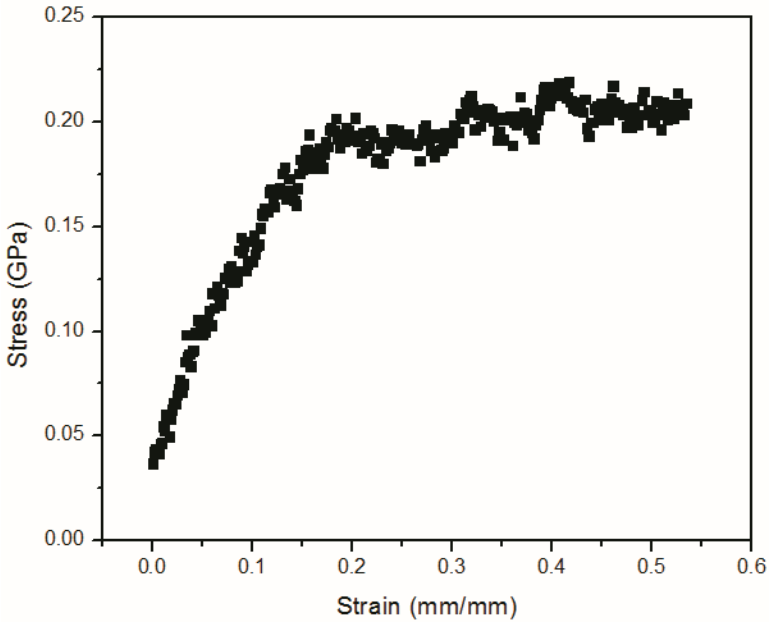

Figure 22. Simulated stress/strain curve for a 50 mol. pct DGEBA and 50 mol. pct. DGEBM matrix polymer with 44DDS as the curative.

Energy Analysis during Strain Deformation

To determine the molecular level events that occur during macromolecular deformation, the potential energy was monitored during the applied stress/strain. In the COMPASS forcefield, the potential energy of a polymeric system is comprised of fourteen individual terms.[83] While all fourteen components of the potential energy are necessary for a realistic simulation of a polymer, the most significant terms are bond angle, dihedral angle, and van der Waals energies. Additionally, these energies are proposed to be the most effected by applied deformation.[84] To test this hypothesis, the potential energy and its significant constituents were monitored during a tensile deformation simulation.

As a result of the stress/strain simulations previously discussed in this chapter, the polymer structures are saved at specific strain values (typically every 0.01 strain). The saved polymer structures include both the positional and energetic information at every

strain. The structures are then used as the input information in a developed programming script to calculate the total potential energy and components. The written script has been sectioned into several parts shown in Figure 23, Figure 24, Figure 25, and Figure 26. The Materials Studio scripting environment uses the PERL languages and compiler. PERL is considered an object oriented language and is similar to others such as C++ or JAVA. The focus of this script is to take the input file, process it, and run an NPT dynamics simulation to determine an average value for the total potential energy, and as many components as specified. All energies will be tabulated in individual tables (.std files) for post-simulation processing. The specifics and significance of this post processing will be discussed in Chapter IV.

The written script contains several sections. The first, shown predominately in Figure 23, contains the initialization and notes section. The initialization calls in lines 1-3 are necessary for the compiler to function properly, while the remainder of this section is for annotation purposes as is customary. The second and smallest section (shown in Figure 24) is the user inputs segment. Suggested values are placed to initialize the script variables but could be changed here if desired. This is the only section that a user of the script would change; the rest of the code is prepared without the need for user variation to minimize compiler errors. The third section of code begins the energy analysis section and is shown in Figure 24 and Figure 25. This section initializes the remaining variables and files for the NVT dynamics calculations to be performed. Contained in this section are two FOR loops, which will iterate through all of the input strain values and their associated structures. The energy analysis section of code also includes the updating of the tables with the proper energy terms. The final section of code is shown in Figure 26 and contains the optimization section of the coding. Due to the extremely large size of

each file and the large number of files generated, the unnecessary files are deleted to conserve space and reduce calculation and download time. If it were necessary to retain the files instead of deleting them, it would be achieved by removal of this section; however, this is not recommended, as the total download directory will exceed one gigabyte of memory.

```
#!perl
use strict;
use MaterialsScript qw(:all);

#-------------------------------------------------------------------------------
#---BEGIN NOTES SECTION---------------------------------------------------------
#-------------------------------------------------------------------------------
#
# Author:       Christopher H. Childers
#
# Version:      v 1.10
#
# Modified:     08/18/2011 v 1.00
#               Christopher H. Childers
#               Original Version
#
#               08/24/2011 v 1.10
#               Christopher H. Childers
#               Added angle, bond, potential, and
 #                van der Waals energies
#                (See Description)
#
# Input:        inputtrajectoryfile.xtd (myStressStrain-* from Polymer Protocol)
#
# Output:       TorsionEnergy.std
#               AngleEnergy.std
#               BondEnergy.std
#               PotentialEnergy.std
#               VanDerWaalsEnergy.std
#               The files are study tables that contain the calculated energies from
#                all the input frames. Each column is for each frame in the input
#                files. Each row is from every created frame from the NVT
#                calculation   run in this script. The Number of rows should equal
#                the number of created frames.  (Duration / NVT Frequency)
#
# Desc.:        The purpose of this script is to take an input file from the
#                stress-strain analysis of the polymer protocol and run and NVT on
#                it. The NVT should be fairly short in order to prevent major
#                structural changes from occurring.  (Duration Recommended
#                <= 5000) This NVT is run on every input. Then on the output
#                NVT information for each frame, Forcite will calculate several
#                energy types. This information is then put into study table
#                documents for ease of access.
#
# Refs.:        Andrea R. Browning, Ph.D.
```

Figure 23. Energy analysis during deformation PERL script section one: document initialization and notes.

```
#                Molecular Modeling: Principles and Applications, 1st Ed.
#                   Andrew R. Leach
#
#-------------------------------------------------------------------------------
#---END NOTES SECTION-----------------------------------------------------------
#-------------------------------------------------------------------------------

#---USER INPUTS-----------------------------------------------------------------

my $inputtrajectoryfile = "myStressStrain-x";
my $numtrajectories = 50;
my $duration = 5000;
my $nvtfrequency = 250;

#---END USER INPUTS-------------------------------------------------------------

#---TORSION ANALYSIS------------------------------------------------------------

# Define Document
my $doc = $Documents{ "$inputtrajectoryfile.xtd" };

# Number of Created Frames
my $numcreated = $duration / $nvtfrequency;

#Define Study Table
my $stdytbl1 = MaterialsScript::Documents->New( "TorsionEnergy.std" );
my $stdytbl1_data = $stdytbl1->InsertSheet( 0, "Data" );
my $stdytbl2 = MaterialsScript::Documents->New( " AngleEnergy.std" );
my $stdytbl2_data = $stdytbl1->InsertSheet( 0, "Data" );
my $stdytbl3 = MaterialsScript::Documents->New( "BondEnergy.std" );
my $stdytbl3_data = $stdytbl1->InsertSheet( 0, "Data" );
my $stdytbl4 = MaterialsScript::Documents->New( "PotentialEnergy.std" );
my $stdytbl4_data = $stdytbl1->InsertSheet( 0, "Data" );
my $stdytbl5 = MaterialsScript::Documents->New( "VanDerWaalsEnergy.std" );
my $stdytbl5_data = $stdytbl1->InsertSheet( 0, "Data" );

# Loop Thru All Trajectories
for (my $ctraj = 1; $ctraj <= $numtrajectories; ++$ctraj)
{
    # Track Current Frame and Update in Dummy File
    $doc -> CurrentFrame = $ctraj;
    my $dummy = $doc -> SaveAs( "Frame_$ctraj.xsd" );

    # NVT On Each Frame
    my $results = Modules -> Forcite -> Dynamics -> Run( $dummy, ([ Quality = "Ultra-
    Fine", NumberofSteps => $duration, TimeStep => 1.00, CurrentForcefield =>
```

Figure 24. Energy analysis during deformation PERL script sections two and three. Sections include the end of notes, user inputs, and the beginning of the energy analysis section.

```
"COMPASS", TotalChargeTolerance => 0.15, TrajectoryFrequency =>
$nvtfrequency, Thermostat => "Andersen", Barostat => "Andersen", Ensemble3D =>
"NVT", Temperature => 300, Pressure => 0.0001,
'3DPeriodicElectrostaticSummationMethod' => "Group based",
'3dPeriodicvdwSummationMethod' => "Group based"]));

my $doc2 = $Documents{ "Frame_$ctraj.xtd" };

# Update Study Table
my $col = $ctraj-1;
$stdytbl1_data -> ColumnHeading( $col ) = "Frame "."$ctraj";
$stdytbl2_data -> ColumnHeading( $col ) = "Frame "."$ctraj";
$stdytbl3_data -> ColumnHeading( $col ) = "Frame "."$ctraj";
$stdytbl4_data -> ColumnHeading( $col ) = "Frame "."$ctraj";
$stdytbl5_data -> ColumnHeading( $col ) = "Frame "."$ctraj";

for (my $newtraj = 1; $newtraj <= $numcreated; ++$newtraj)
    {
    # Track current Frame and Update In Dummy File
    $doc2 -> CurrentFrame = $newtraj;
    my $dummy2 = $doc2 -> SaveAs( "Frame_" . "$ctraj+" "$newtraj.xsd");

    # Forcite Energy Calculation
    my $results = Modules -> Forcite -> Energy -> Run( $dummy2, ([Quality =>
    "Ultra-Fine", CurrentForcefield => "COMPASS", TotalChargeTolerance =>
    0.15, '3DPeriodicElectrostaticSummationMethod' => "Group based",
    '3DPeriodicvdwSummationMethod' => "Group based" ]));

    print "Energy Analysis Frame " . "$ctraj" "$newtraj" " Complete. \n";

    # Update Study Table
    my $row = $newtraj – 1;
    $stdytbl1_data -> Cell( $row, $col ) = $dummy2 -> TorsionEnergy;
    $stdytbl2_data -> Cell( $row, $col ) = $dummy2 -> AngleEnergy;
    $stdytbl3_data -> Cell( $row, $col ) = $dummy2 -> BondEnergy;
    $stdytbl4_data -> Cell( $row, $col ) = $dummy2 -> PotentialEnergy;
    $stdytbl5_data -> Cell( $row, $col ) = $dummy2 -> VanDerWaalsEnergy;

    # Delete Dummy Files
    my $del1 = $Documents{ "Frame_" . "$ctraj" "_" . "$newtraj.xds" };
    my $del2 = $Documents{ "Frame_" . "$ctraj" "_" . "$newtraj.txt" };
    $del1 -> Delete;
    $del2 -> Delete;
    }

# Delete Remaining Dummy Files
```

Figure 25. Energy analysis during deformation PERL script code containing the remainder of section three and the first half of section four. Section three includes the energy analysis during deformation, and section four removes the extraneous information to reduce the overall file size.

```
    my $todel1 = $Documents{ "Frame_$ctraj.xsd" };
    my $todel2 = $Documents{ "Frame_$ctraj.txt" };
    my $todel3 = $Documents{ "Frame_$ctraj Energies.xcd" };
    my $todel4 = $Documents{ "Frame_$ctraj Temperature.xcd" };
    my $todel2 = $Documents{ "Frame_$ctraj.xtd" };
    $todel1 -> Delete;
    $todel2 -> Delete;
    $todel3 -> Delete;
    $todel4 -> Delete;
    $todel5 -> Delete;
    }

# Prevents All Files From Opening On Download
Documents -> CloseAll;

#---END TORSION ANALYSIS-----------------------------------------------------------

#--------------------------------------------------------------------------------
#---END SCRIPT---------------------------------------------------------------------
#--------------------------------------------------------------------------------
```

Figure 26. Energy analysis during deformation PERL script including the remaining code of section four. Section four deletes unnecessary information and concludes the script.

CHAPTER IV

DETERMINATION OF MATRIX POLYMER YIELD BY A NOVEL MOLECULAR DYNAMICS POTENTIAL ENERGY ANALYSIS

Objective

The goal of this chapter is to introduce and discuss a novel approach to the molecular dynamics simulation of thermoset matrix polymer yield point and provide molecular level insight into the possible cause of polymer yield. This will be achieved by the determination of the total matrix potential energy, and its components during applied tensile deformation. The specific components studied were: total potential energy, dihedral angle (torsion) energy, van der Waals energy, and bond stretching energy. The simulated potential energies of the polymer under deformation were then compared to the applied strain to identify any correlations between the two. It was found that the total potential energy, dihedral angle energy, and van der Waals energy were correlated strongly to the amount of deformation applied, while the bond stretching energy was not. Furthermore, the van der Waals energy was found to deviate from a linear correlation with the applied strain at the yield point of the polymer, suggesting that the matrix polymers with molecular units that allow for higher bond rotation and facile molecular level re-arrangements would have a higher yield strain. Lastly, this analysis is also a novel approach for simulation of the yield point of the material that would not have the same drawbacks as the current approach. All polymers simulated were based on 4,4'-diaminodiphenyl sulfone and a series of bisphenol diglycidyl ethers.

Results and Discussion

Simulated Matrix Systems

In all matrix systems studied, 4,4'-diaminodiphenyl sulfone (44DDS) was used as the amine component of the matrix system. The epoxide component of the matrix was varied between the diglycidyl ethers of bisphenols A, C, F, and S. Additionally, the diglycidyl ethers of oxy diphenol (DGEODP) and thio diphenol (DGETDP) were also studied. In all of the simulated matrix systems, the polymer matrix generated was based on a stoichiometrically equivalent simulation. The molecular structures of the simulated epoxy and amine components are shown in Figure 27. During the course of the simulation process, both the amine and epoxy components were modified, as discussed previously in Chapter III, to create accurate chemical structures during the matrix build process.[63,70]

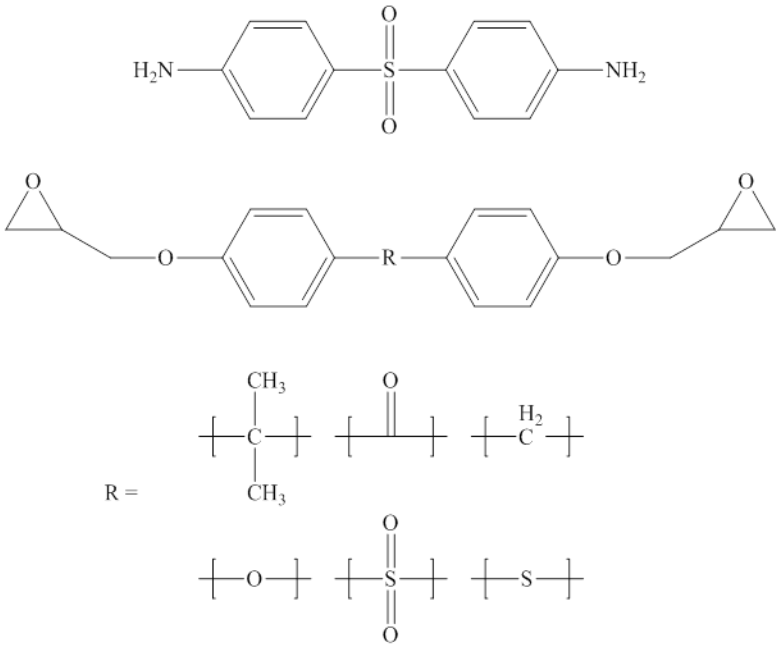

Figure 27. Chemical structures of 44DDS (top) and diglycidyl ethers (bottom) simulated. Top, from left to right, DGEBA, DGEBC, and DGEBF. Bottom, from left to right, DGEODP, DGEBS, and DGETDP.

Material Properties

Material properties for a series of thermosetting matrix polymers were simulated using molecular dynamics. All polymers simulated were similar in their chemical composition, with only the linkage between phenyl rings in the epoxide molecules being varied. These variations were chosen based on their synthetic viability and also to explore the effect of different epoxide linkages on the thermo-mechanical properties of these polymers. Identification of a specific chemical linkage that could be incorporated into future polymer networks which would significantly improve macromolecular performance of the polymer was desired. The specific epoxide linkage variations are shown in Figure 27. It was believed that incorporating chemical linkages that would affect the chain motions of the polymer network, such as the ether or sulfone, would alter the ability of the polymer to dissipate mechanical energy as heat, in turn, changing the mechanical performance of the network.

Table 3

Simulated matrix polymer material properties.

Epoxy	Tg °C	ρ g / cm^3	E GPa	ν	A cm / cm / °C
DGEBA	190	1.2	4.54	0.321	52
DGEBF	194	1.23	4.58	0.343	56.9
DGEBC	206	1.27	5.02	0.342	51.5
DGEBS	222	1.32	5.89	0.313	45.5
DGEODP	192	1.26	4.82	0.334	51.1
DGETDP	188	1.28	4.65	0.353	56.2

Symbols meaning: Tg, glass transition temperature. ρ, density. E, Young's modulus. ν, Poisson's ratio. α, linear coefficient of thermal expansion.

The simulated properties of each of the polymer networks are shown in Table 3. It was observed that the sulfone containing epoxide generated the highest glass transition temperature while also having the highest modulus and density. The observed density was expected with the incorporation of elements of higher atomic mass than carbon. Exactly why the sulfone linkage shows a drastic improvement in glass transition temperature is not clear from this class of simulation. Based on the fundamental definition of glass transition temperature being the ability of long range cooperative chain rotation,[6,85] it is believed that the sulfone linkage requires more thermal energy than the other simulated epoxide spacers for cooperative motions resulting in a higher glass transition. Furthermore, due to how glass transition was determined, there could also be a change in the free volume characteristics of the sulfone matrix polymers that results in an increase in the observed glass transition temperature. The tensile modulus of these thermosetting network polymers also appears to be correlated to the glass transition temperature of the material. Figure 28 shows the observed linear correlation between the two material properties. While this correlation between Tg and tensile modulus is observed, from these simulations, their interdependence is not fully understood; however, it is hypothesized that this dependence is related to the network morphology of the polymer. As the glass transition temperature increases and thus molecular mobility is reduced, the elastic component of the strain behavior would become more rigid, increasing the modulus of the polymer network.

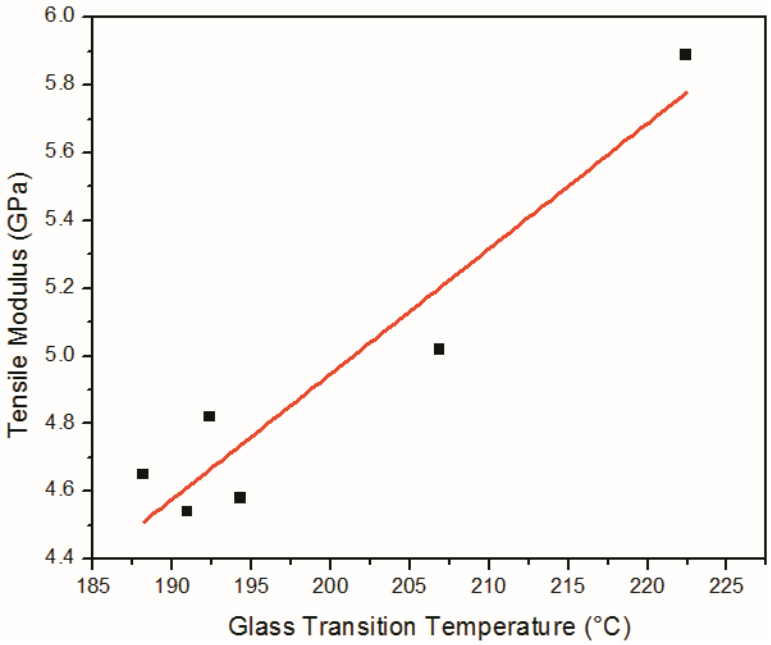

Figure 28. Young's modulus correlation with glass transition temperature. Linear fit with R2 = 0.8852.

In addition to the thermal and mechanical properties previously mentioned and listed in Table 3, the yield behavior of these polymers was also simulated. Stress/strain curves generated by the simulations are shown in Figure 29. While all of the curves are similar in behavior, the specific yield strain for each polymer is unique and presented in Table 4. The yield strains were determined by a third order polynomial fit of each of the stress/strain curves, with the yield strain being taken as the point where the first derivative of the fit was equal to zero. This calculation is convoluted by the nature of the simulations. The simulation design does not allow for material failure due to applied stress or strain to occur. Therefore, toward the end of the simulation, the graphs can begin to become distorted, which will artificially influence the determination of the yield strain when using mathematical determination methods such as polynomial fitting. Also, the stress/strain curve does not aid in the determination of molecular level events that lead to polymer matrix yield. However, from the other material properties simulated, it would

appear that the molecular mechanism for yield may not be related to the mechanism for glass transition or modulus, as DGEODP does not exhibit an exceptionally high glass transition temperature and only an average tensile modulus.

Table 4

Simulated yield strain for all polymer matrix systems using a standard approach.

Epoxy	Yield Strain mm/mm
(a) DGEBA	0.2804
(b). DGEBF	0.361
(c). DGEBC	0.3406
(d). DGEBS	0.3241
(e). DGEODP	0.3501
(f). DGETDP	0.1999

Letters for each system correlate to the labeled stress/strain curves in Figure 29.

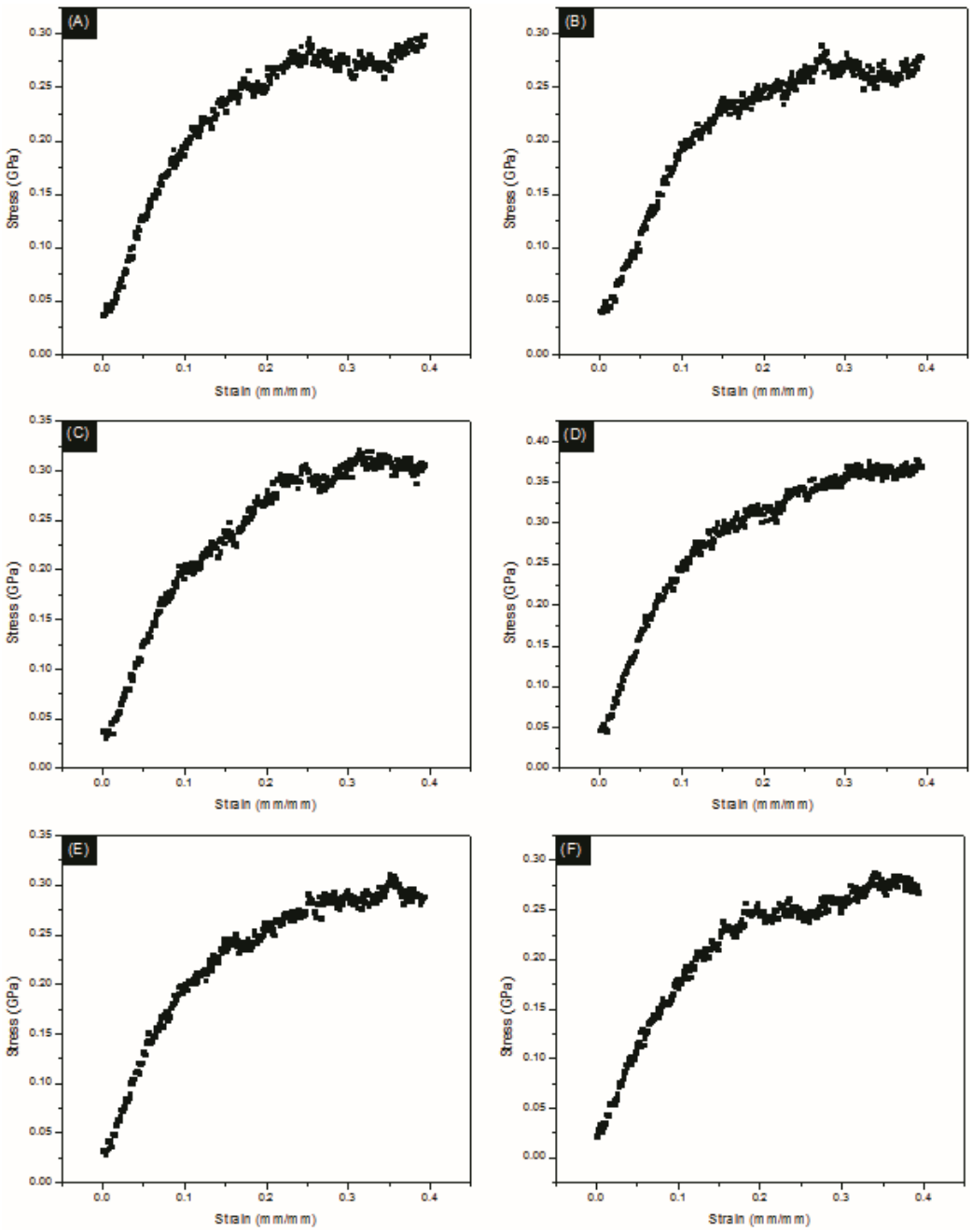

Figure 29. Simulated stress/strain curves for epoxide systems with 44DDS as the amine curative. The epoxide used is as follows: (a) DGEBA (b) DGEBF (c) DGEBC (d) DGEBS (e) DGEODP and (f) DGETDP. [Lettering correlates to Table 4]

Matrix Energy Analysis during Deformation

In an effort to determine molecular level events that lead to thermosetting polymer yield, and ultimately complete failure, the potential energy of the system was calculated during the stress/strain simulation. Specifically, the total potential, bond stretching, dihedral angle, and van der Waals energies were monitored. The results of these calculations for the 44DDS/DGEBA polymer matrix are shown in Figure 30 and are representative of all polymer systems. The simulated matrix energetic responses to deformation for the DGEBF, DGEBC, DGEBS, DGEODP, and DGETDP based polymers are shown in Figure 31, Figure 32, Figure 33, Figure 34, and Figure 35, respectively. While not surprising, it is both important and consistent with previous work, in which the potential energy increases over the entire duration of the stress/strain calculation.[84] While the results are consistent, it is interesting that there appears to be a linear increase in total potential energy as a function of strain, despite material yield occurring over the observed strain. No deviation is present. Therefore, it stands to reason that either the total potential energy of the system is unrelated to the applied strain, or a component of the total potential energy must be related to material yield. For this reason, the individual components of potential energy were calculated. Figure 30b shows the bond stretching energy component of the potential energy. Interestingly, there appears to be no correlation between the bond stretching energy and the applied strain. The lack of correlation is interesting because if the culprit for material yield or ultimate failure were to be the rupture of intramolecular bonds, there should be a fairly strong correlation between the applied strain and the bond stretching energy. Since this is not the case, some other contribution of potential energy may be the primary cause of material yield and/or ultimate failure. Furthermore, since the bond stretching energy is unrelated to the applied

strain, it would support the hypothesis that when this class of polymer does yield or fail, it does so not by breaking of chemical bonds but by loss of intermolecular cohesion between highly cross-linked regions.[86]

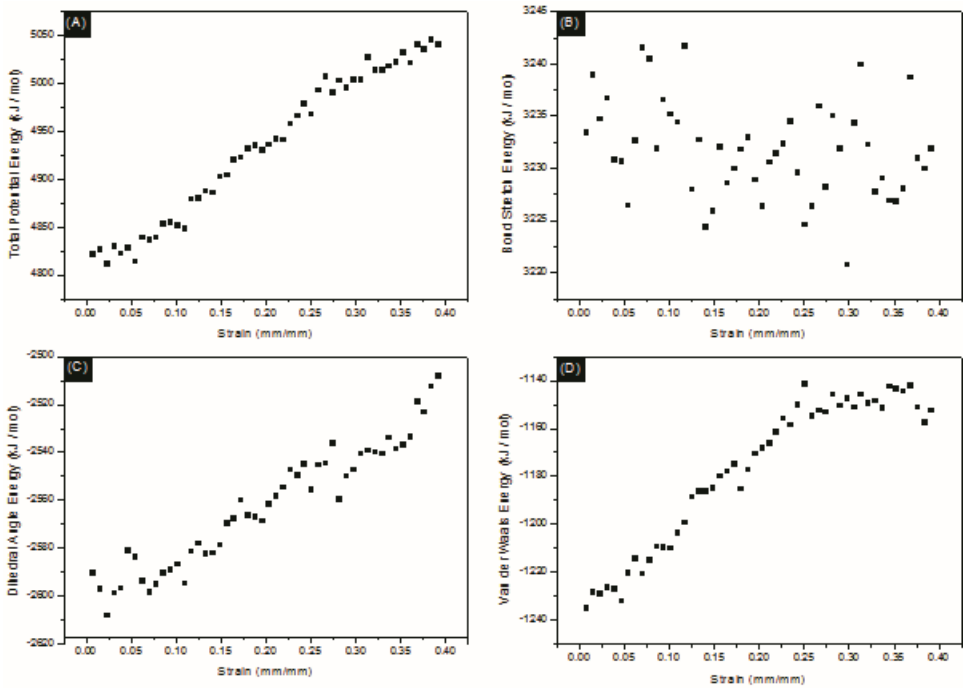

Figure 30. For the DGEBA/44DDS matrix polymer (a) Total potential energy versus strain. Linear regression with $R^2 = 0.9770$. (b) Bond stretching energy versus strain. (c) Dihedral angle energy as a function of strain. Linear regression with an $R^2 = 0.9269$. (d) van der Waals energy versus strain. Linear regression with an $R^2 = 0.9719$.

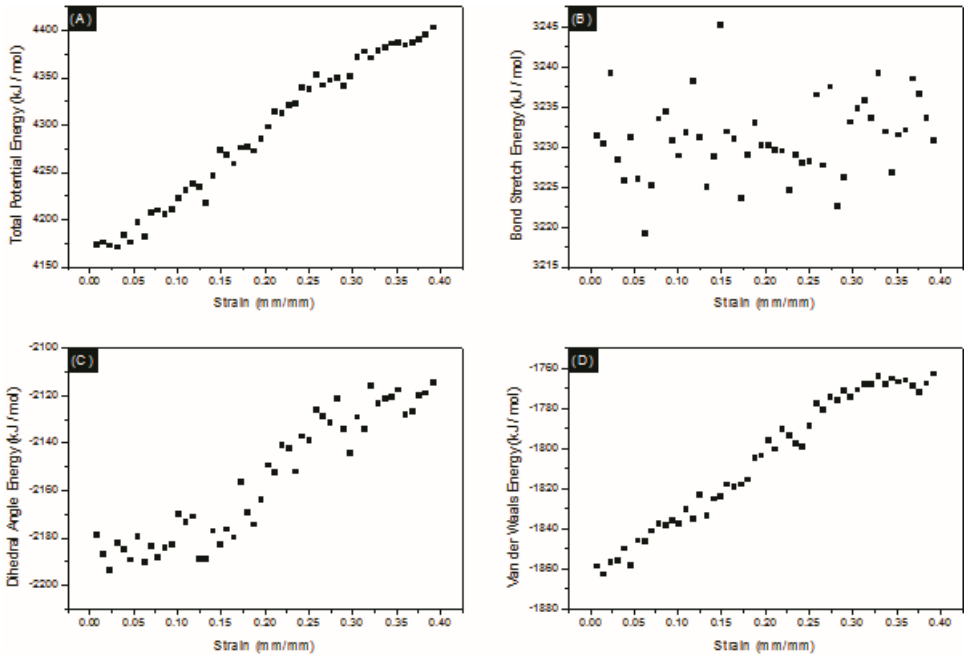

Figure 31. For the DGEBF/44DDS matrix polymer (a) Total potential energy vs strain. (b) Bond stretching energy vs strain. (c) Dihedral angle energy as a function of strain. (d) van der Waals energy vs strain.

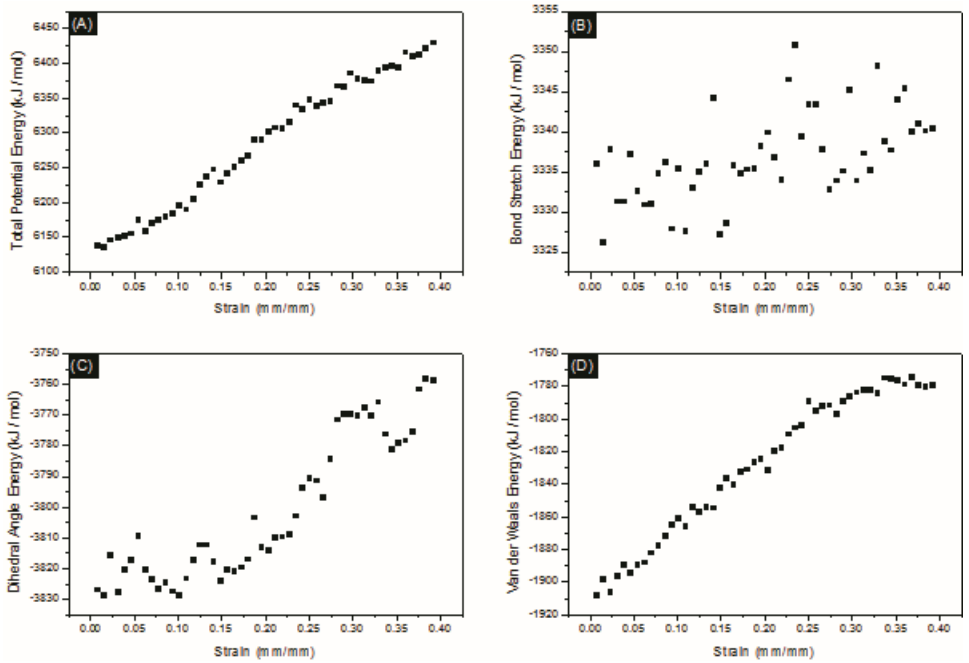

Figure 32. For the DGEBC/44DDS matrix polymer (a) Total potential energy vs strain. (b) Bond stretching energy vs strain. (c) Dihedral angle energy as a function of strain. (d) van der Waals energy vs strain.

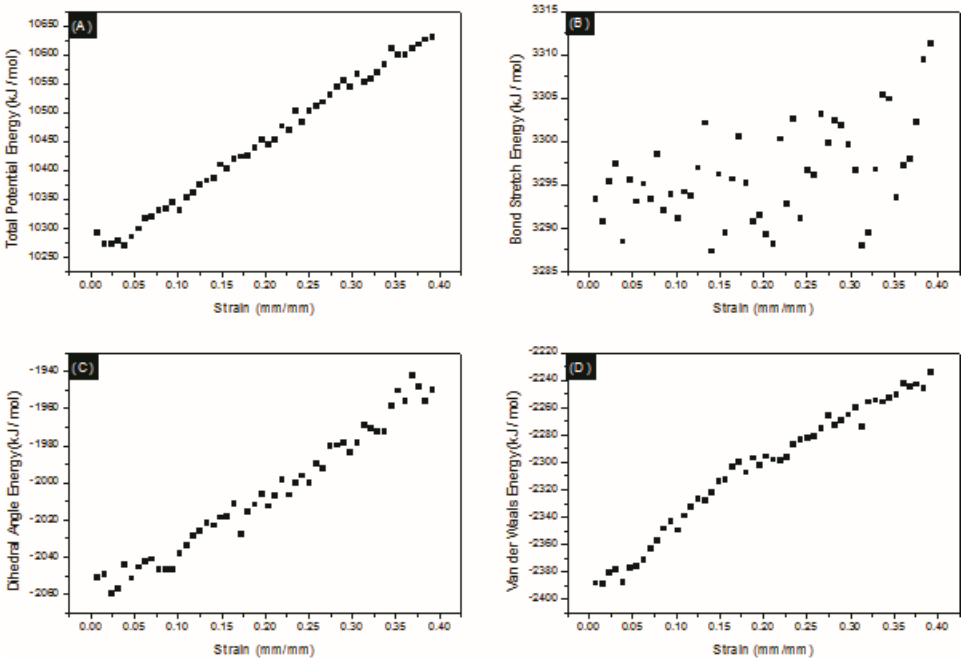

Figure 33. For the DGEBS/44DDS matrix polymer (a) Total potential energy vs strain. (b) Bond stretching energy vs strain. (c) Dihedral angle energy as a function of strain. (d) van der Waals energy vs strain.

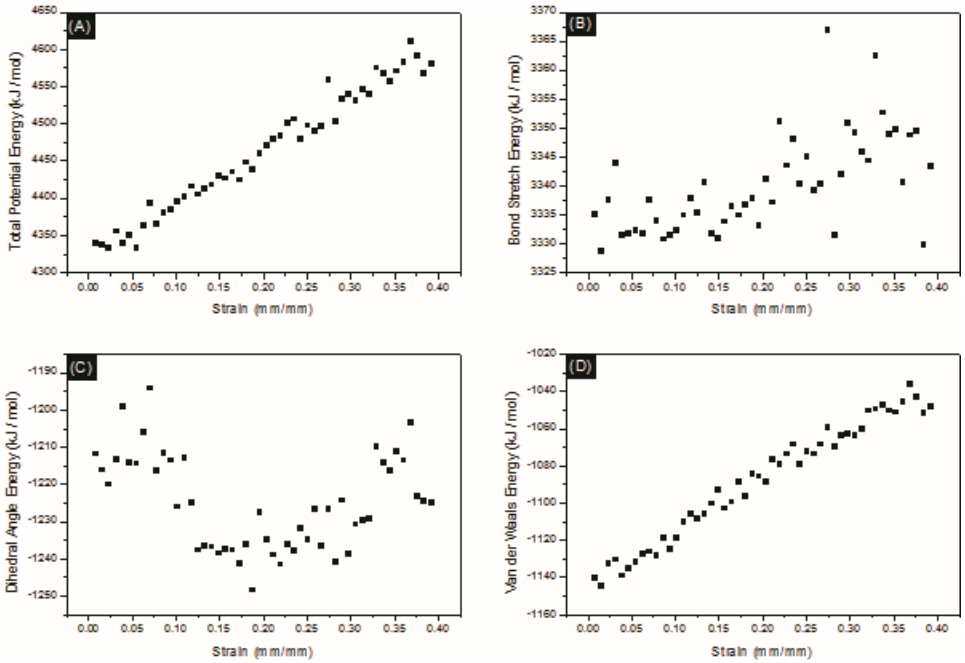

Figure 34. For the DGEODP/44DDS matrix polymer (a) Total potential energy vs strain. (b) Bond stretching energy vs strain. (c) Dihedral angle energy as a function of strain. (d) van der Waals energy vs strain.

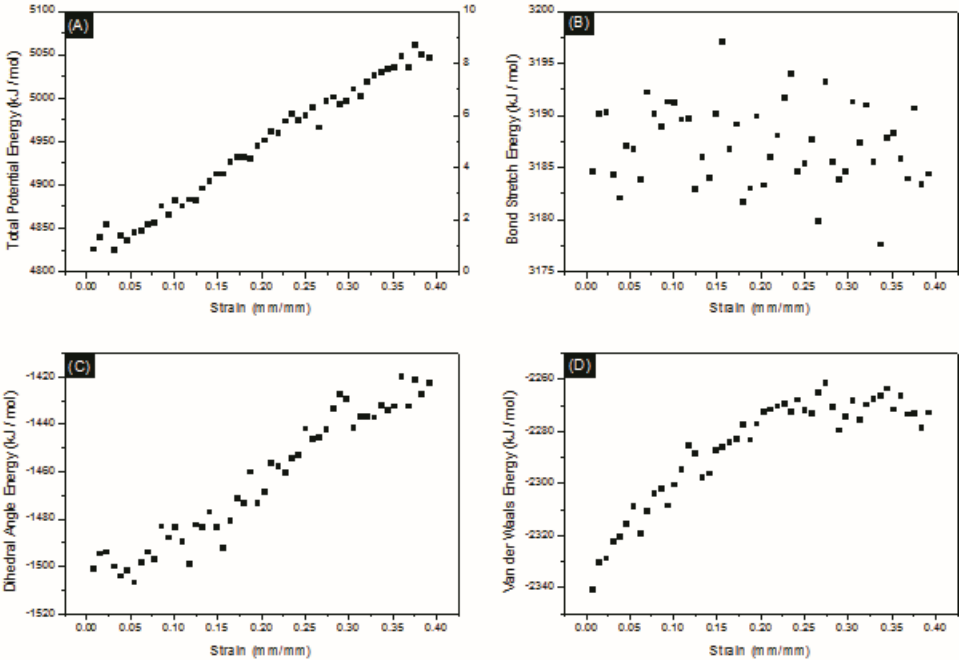

Figure 35. For the DGETDP/44DDS matrix polymer (a) Total potential energy vs strain. (b) Bond stretching energy vs strain. (c) Dihedral angle energy as a function of strain. (d) van der Waals energy vs strain.

The second component of potential energy investigated was the dihedral angle energy. Figure 30c shows a plot of dihedral angle energy as a function of the applied strain. While this energy does appear to be related to the applied strain and a linear increase in energy is observed, similar to the total potential energy, there appears to be no deviation from linearity, despite material yield occurring. Therefore, while this energy may be an important contribution to how the polymer matrix absorbs energy, in the form of strain, it is not the limiting factor of the material that will cause yield in tension.

Table 5

van der Waals energy deviation point from linearity for all simulated matrix polymers.

Epoxy	VDW Deviation mm/mm
DGEBA	0.2583
DGEBF	0.3601
DGEBC	0.3281
DGEBS	0.3293
DGEODP	0.3763
DGETDP	0.2038

The third component of potential energy calculated was the van der Waals energy of the molecule. The van der Waals energy is associated with the distance between either inter- or intramolecular atoms, specifically their ability to be in close proximity to one another as the electron clouds begin to overlap.[54,55] Figure 30d shows a plot of the van der Waals energy as a function of strain for the 44DDS/DGEBA system, and Figure 36 shows the plots for the entire polymer matrix materials studied. It was found that the van der Waals energy increases linearly as a function of the applied strain; however, after a deviation point is reached, there exists no correlation between the two. A deviation point was observed for all of the systems studied (Figure 36) and varies based on the composition of the matrix material. This suggests that the various chemical linkages allow the polymer to dissipate different amounts of mechanical energy before yield. Because this deviation from linear dependence was only observed in the case of the van der Waals energy, it suggests that the molecular level event responsible for the material yield would be related to the ability of the matrix polymers to accommodate a changes in molecular orbital overlap, possibly by bond rotation.[56] The plateau in van der Waals energy would also imply that the polymer yielding process would be constant volume

process. The van der Waals energy versus strain plots are shown in Table 5. It was found that the epoxide molecule containing an ether linkage (DGEODP) had a deviation from linearity in its vdW versus strain behavior at a higher strain than the other epoxide networks. The DGEBF based system also demonstrated deviation from linearity of the vdW versus strain plot at a high strain. Both of these molecules contain a fairly small, flexible spacer between the aromatic rings that is capable of significant bond rotation: an ether linkage in the case of DGEODP and a methylene linkage in the case of DGEBF. This suggests that the ability for a molecule to allow for more facile molecular level rearrangements might generate a polymer network with improved yield performance.

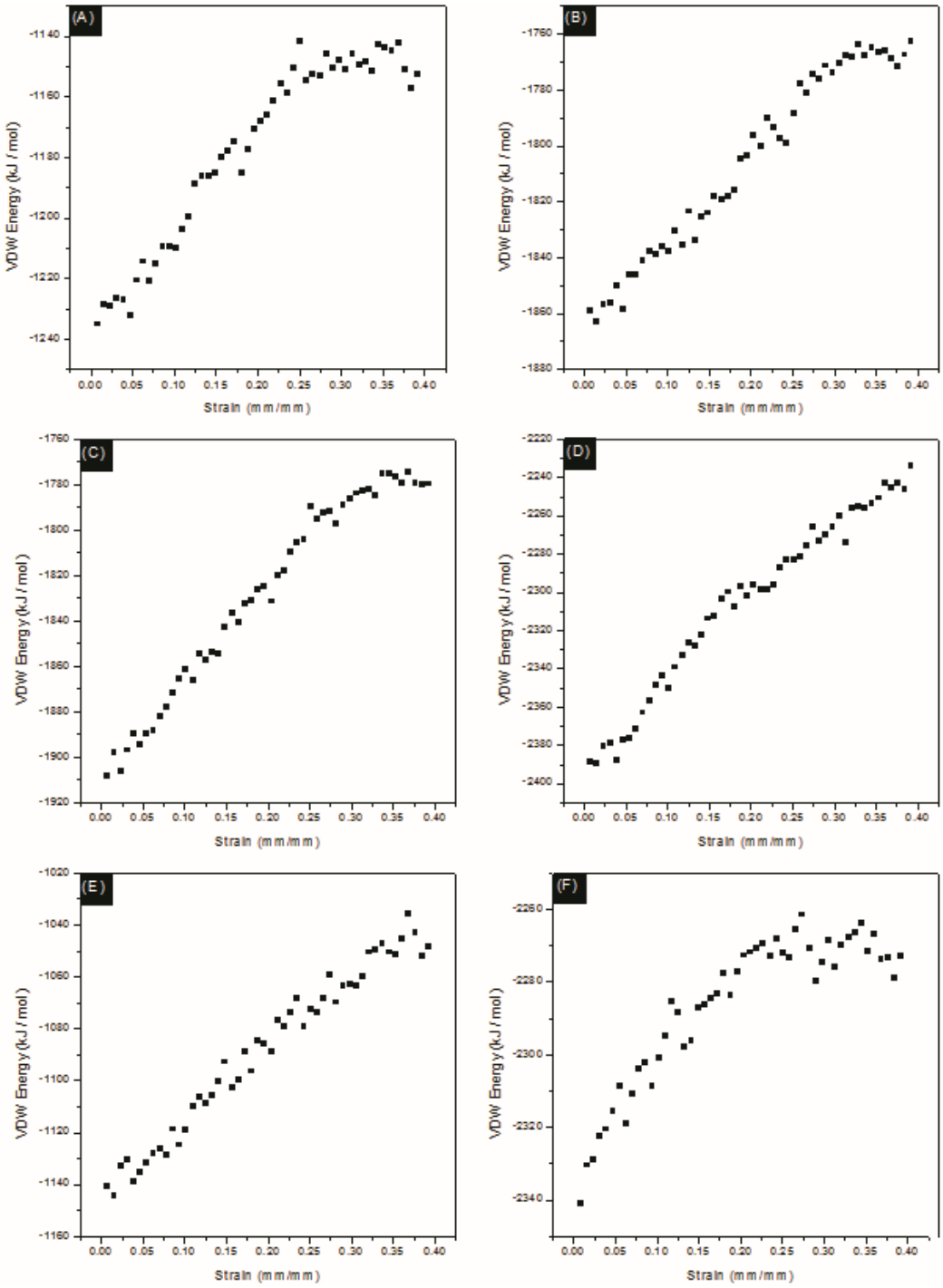

Figure 36. van der Waals energy as a function of strain for (a) DGEBA (b) DGEBF (c) DGEBC (d) DGEBS (e) DGEODP and (f) DGETDP as the epoxide component with 44DDS as the amine component.

Energy Deviation Correlation to Yield

In order to determine molecular level causes for macro-scale events, such as material yield, it is necessary to determine what factor or factors influence the event. To this end, potential energy and its components were studied in the previous section under applied stain deformation. It was noted that the van der Waals energy was the only limiting factor found. If there exists a correlation between the van der Waals deviation from linearity and the strain at yield for a material, then it is reasonable to suggest that the ability for a molecule to undergo facile molecular level rearrangement is a molecular level cause for yield. Furthermore, this information can be used to design matrix polymer molecules in such a way to maximize the strain at yield and as a novel method for determining the strain at yield in molecular dynamics simulations.

The correlation between the van der Waals deviation strain and the calculated strain at yield is shown in Figure 37. In this figure, an overlay of the stress/strain curve and the van der Waals energy is shown. In every instance, the observed strain at yield from the stress/strain curve and the van der Waals deviation energy are similar to one another. The calculated values for the van der Waals deviation point are listed in Table 5, and the strain at yield values are listed in Table 4. The correlation between the two is demonstrated in Figure 38, where a linear relation between the two factors with an R^2 greater than 0.9 is observed. Because the van der Waals deviation and strain at yield are related, then it stands to reason that a primary cause on the molecular level of the macromolecular yield could be an inability of the polymer matrix to accommodate further molecular orbital overlap. To overcome the inability to accommodate more van der Waals energy, the material becomes mobile on a more global scale, or yields. Additionally, this information could be employed in the future rational molecular design

of molecules that display enhanced yield performance. This would be achieved by the incorporation of molecular units that exhibit improved flexibility through bond rotation. However, units such as a sulfone linker in the bisphenol also increase the density of the material which may not be desired.

In addition to providing insight on a molecular level to macro-scale events, monitoring of the van der Waals energy provides a method of determining the strain at yield using Molecular Dynamics simulations. As previously mentioned, the current approach of yield strain determination involves either a visual determination or the implementation of a mathematical model. The mathematical determination of yield, however, is currently limited by the simulations inability to accurately predict material failure. As a result, much past yield the curves begin to lose coherence, reducing the accuracy of a polynomial fit. Conversely, monitoring of the van der Waals energy and determination of the deviation from linearity is not effected by the lack of accurate failure predictions. Moreover, the analysis is easily incorporated into the original simulation and would add minimal time to the simulation, while allowing for a much simpler determination of yield strain for polymeric systems.

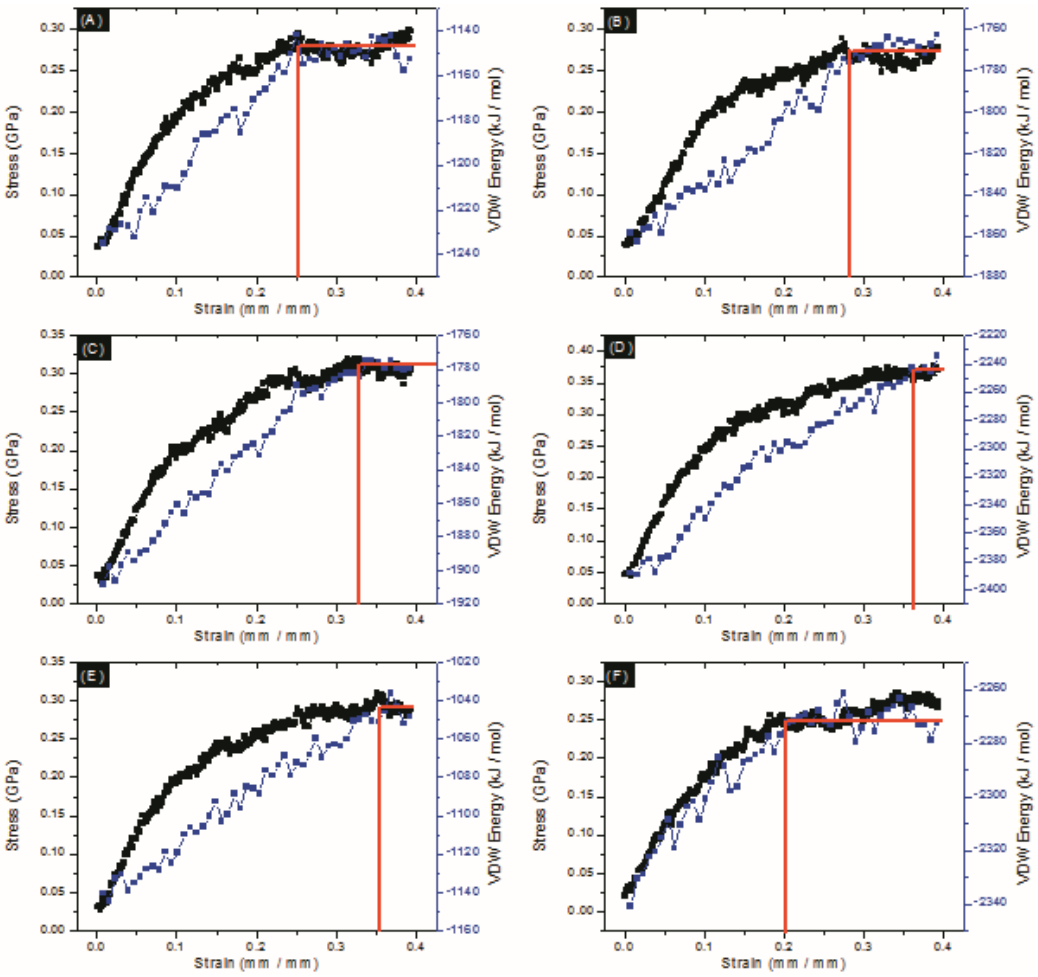

Figure 37. Simulated stress/strain curve plotted with calculated van der Waals energy overlay for the following systems: (a) DGEBA (b) DGEBF (c) DGEBC (d) DGEBS (e) DGEODP and (f) DGETDP. Lines are guide lines drawn for visual assistance.

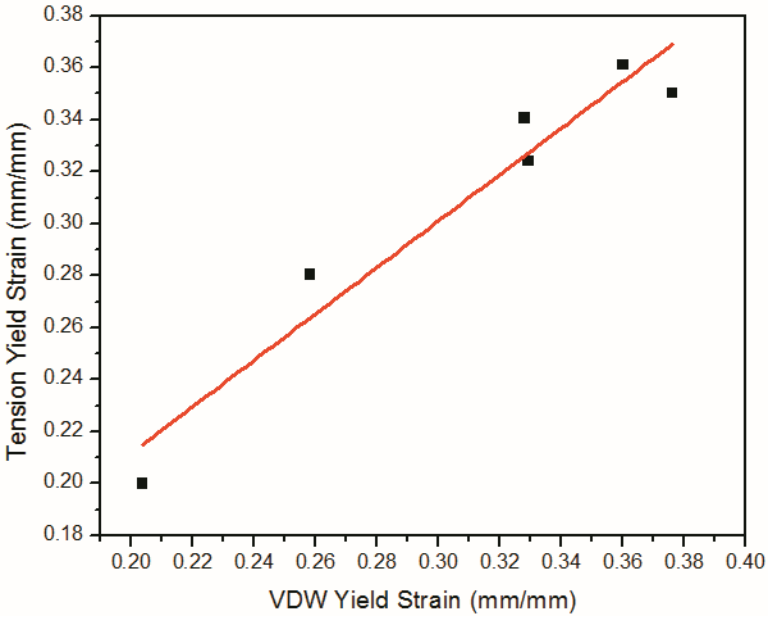

Figure 38. Yield strain calculated from a simulated stress/strain curve vs the yield strain calculated from the van der Waals critical point. Linear regression with $R^2 = 0.9230$.

Conclusions

Thermosetting polymer matrix materials based on 44DDS and several diglycidyl ethers were used to study the molecular level effect of applied strain on a composite matrix polymer via the employment of molecular dynamics simulations. The strain at yield was simulated using a standard applied strain analysis where a stress-strain curve was generated and the yield calculated from the curve. Additionally, the potential energies of all the systems were calculated using the COMPASS® forcefield. This forcefield allowed the observation of how the polymer matrix energy will change as a function of applied strain. These studies showed that the van der Waals energies associated with each of the polymer matrices under applied strain correlated to the yield point of the polymer. Furthermore, it was observed that the van der Waals energy would increase linearly during strain until the yield point was reached. At the yield point, the van der Waals energy became independent of strain, which generated a more precise

method for determination of yield strain for this class of material. These results also suggest that the inclusion of molecular units which allow for higher bond rotation can be included to accommodate more changes in the van der Waals energy, thermosetting polymer matrices to allow for higher macromolecular performance. Analysis of the van der Waals energy of a given system can also be incorporated into the Molecular Dynamics simulations to aid in the simulation's determination of material yield as it does not suffer from the drawbacks associated with the traditional method.

CHAPTER V

DIFUNCTIONAL EPOXIDE NETWORK POLYMER FORMATION DEPENDENCE ON CURE HEATING RAMP RATE

Objective

The objective of this chapter is to discuss the cure heating ramp rate dependence of the properties of thermosetting epoxy/amine polymers for high performance composite matrix applications. Before this work, little agreement can be found in literature on a cure heating ramp rate dependence. I propose that a cure heating rate dependence on matrix polymer formation exists, but limited agreement has been found for two reasons. Firstly, the dependence is chemistry specific. Secondly, the dependence for the more traditional chemistries is on a size scale that relates only to molecular level events and cannot directly be observed on a macro-scale. To that end, several thermal and spectroscopic techniques have been employed to explore cure rate dependence. The polymer matrix studied was based on DGEBF/33DDS and was formulated with cure heating ramp rates varying from 1–25 °C/min. It was found that all of the glass transition temperatures of the polymer matrices were similar; however, NIR, free volume analysis, density analysis, and DES, revealed a strong correlation for how these networks grow in relation to the cure heating ramp rate. Furthermore, a relationship on the molecular level between cure heating ramp rate and polymer matrix properties. The two subsequent chapters also relate to the study of this phenomenon with advanced DES analysis (Chapter VI) and analysis of an additional chemistry (Chapter VII).

Results and Discussion

Thermal Network Evolution

The chemical reaction between an epoxide ring and either a primary or secondary amine is fairly exothermic. Due to this exothermic nature, when exploring network development at various cure heating ramp rates, it is necessary to first study the evolved heat in the reaction. Since there is a large evolution of heat associated with this reaction, enough thermal energy could be released from the reaction and provide a pathway for reaction that is undesired and uncontrolled. These so called "run-away" reactions could lead to polymer degradation. Secondly, since in asymmetric amines there is a difference in activation energies between primary and secondary amine reaction, [4] by changing the ramp rate and the associated exotherm intensity, it might be possible to add enough thermal energy to overcome the higher secondary amine activation energy. This would lead to a competitive reaction between primary and secondary amine.

Figure 39 shows the DSC thermograms of the reaction between 33DDS/DGEBF at ramp rates that vary from 1–15 °C/minute. For this experiment, the amine was pre-dissolved in the epoxide monomer at 125 °C and quenched in liquid nitrogen. It is assumed that a negligible amount of reaction occurred before the DSC experiments were conducted. It was observed that only the slowest heating ramp rate of 1 °C/min exhibited an exothermic peak, indicating that a majority of the reaction occurred. The remaining ramp rates only showed an initial exotherm that did not reach a maximum during the heating process. This is expected due to the reduction in elapsed time between the slowest and fastest ramp rates. Due to the differences in primary and secondary amine reactivity and differences of each sample at different temperatures, it was believed that the formation of the network may be different as the ramp rates are increased.

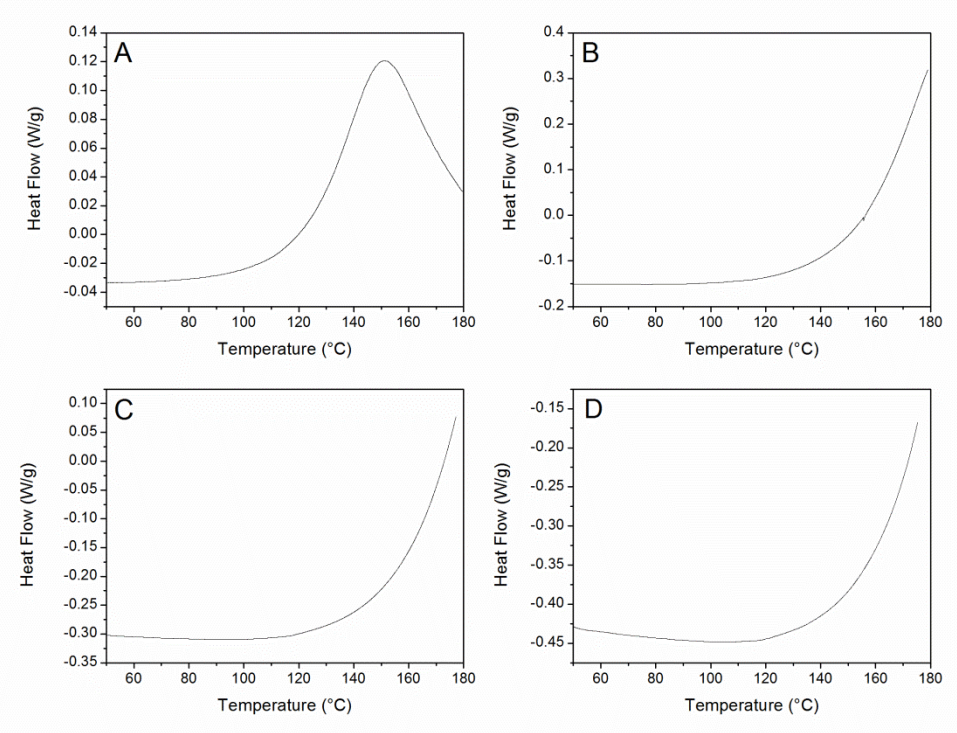

Figure 39. DSC thermograms of 33DDS/DGEBF curing at a series of ramp rates from 35-180 °C. (a) is 1 °C/min, (b) 5 °C/min, (c) 10 °C/min, and (d) 15 °C/min. (Exotherm is up.)

Using the various ramp rate DSC thermograms shown and discussed above, the temperature at which reaction begins, or onset temperature, and the completion time of reaction were explored. These are valuable parameters from a process design view where the exotherm could be harnessed to reduce the cycle time of part processing while preventing polymer degradation due to excess thermal energy. Figure 40 shows the onset temperature (temperature at which the exotherm begins) as a function of cure heating ramp rate, and the exponential dependence that it exhibits. There is little advantage from an onset point of view for heating at a rate above 10 °C/min, indicating that above this ramp rate, sufficient thermal energy is applied to the system that the exotherm energy of the polymerization reaction now drives the cure. The completion time, displayed in Figure 41, also supports this conclusion. Again, an exponential dependence is observed

for the system where, above a 10 °C/min cure heating ramp rate, no reduction in completion time is observed. Therefore, for this matrix polymer, no advantage would be observed for heating at rates faster than 10 °C/min, and, as will be discussed in a subsequent section of this chapter, may be detrimental and lead to polymer degradation above this ramp rate.

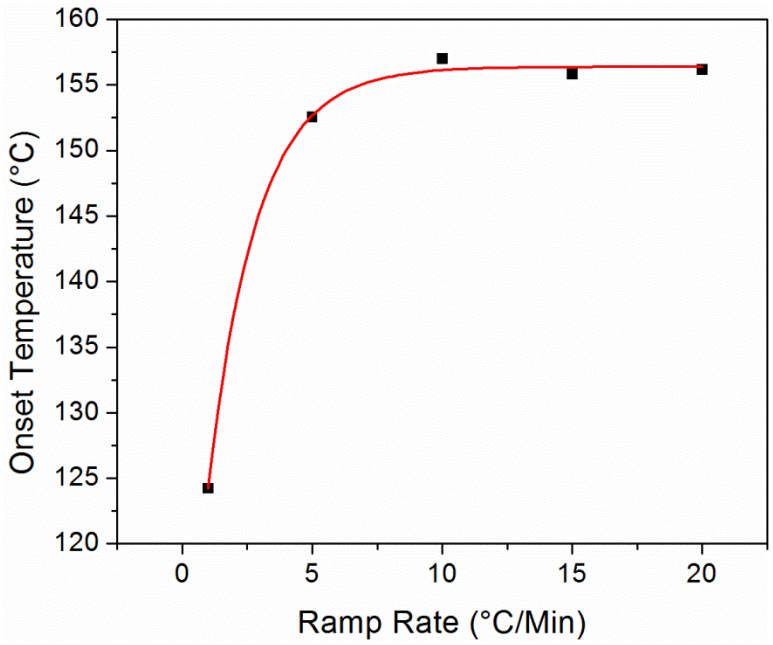

Figure 40. Onset temperature of reaction as a function of cure heating ramp rate. R^2 = 0.9973, exponential fit.

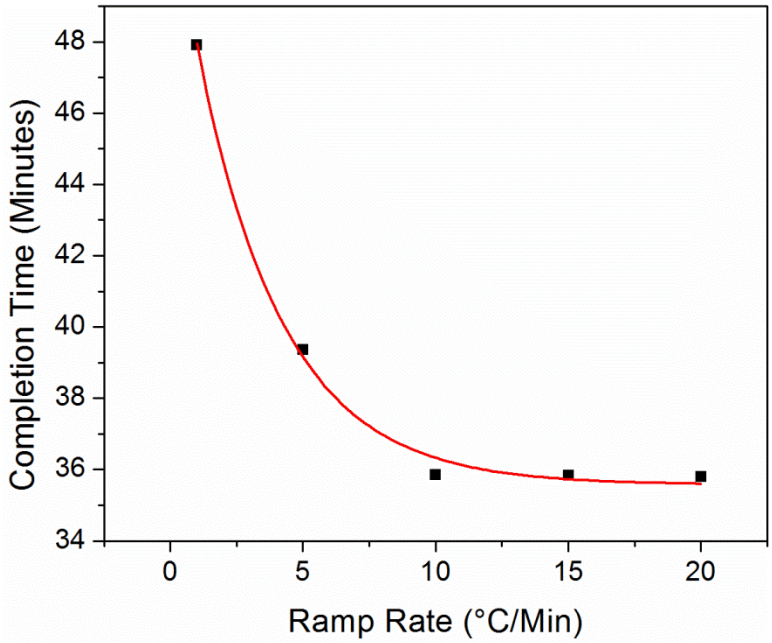

Figure 41. Reaction completion time as a function of cure heating ramp rate. R^2 = 0.9982, exponential fit.

To further explore the extent of reaction that occurs during the heating ramp, a correlation between the exotherm intensity and the ramp rate was found. Figure 42 shows a plot of the exotherm intensity as a function of ramp rate. Exotherm intensity was taken as the integral of the DSC exotherm peak from the onset of reaction to 180 °C. From this graph, it is observed that, at the higher ramp rates, there is little to no reaction occurring in the sample. Due to the differences in elapsed time between the heating rates, this also means that the slower heating rate samples had time for a reaction to occur, and at lower temperatures, it is possible that this reaction was limited to only consumption of the primary amine.

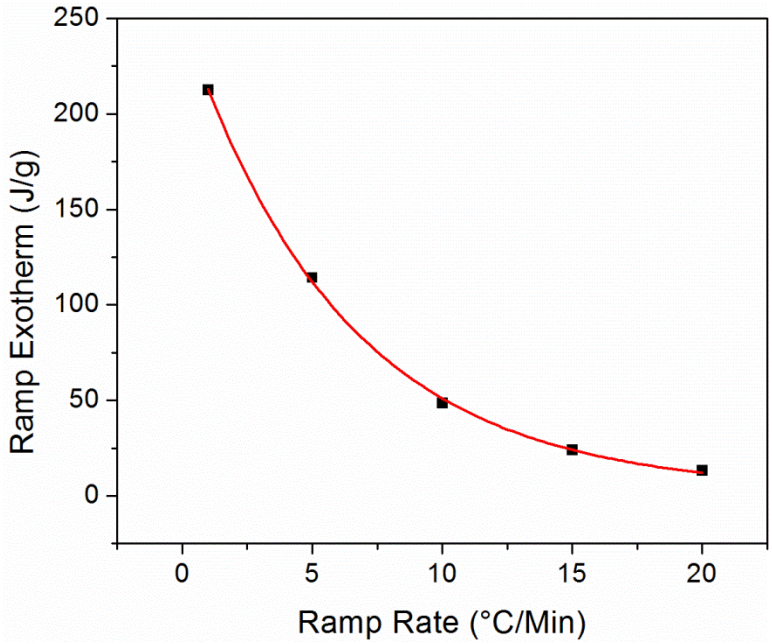

Figure 42. Heating ramp exotherm intensity as a function of cure heating ramp rate. R^2 = 0.9991, exponential fit.

In addition to the heating ramp DSC experiments, DSC heat and hold experiments were conducted. In these experiments, the samples were heated from 35–180 °C, similarly to the previous samples. However, they were allowed to isotherm at 180 °C for a period of 3 hrs. In this set of experiments, the residual exotherm after the heating ramp could also be determined. Figure 43 is a plot of the hold exotherm intensity as a function of cure heating ramp rate. In this case, the fastest ramp rate shows the highest hold exotherm intensity. Because the thermal energy release is so high, enough heat would be present to overcome the activation energy for reaction and the exotherm energy should now drive the reaction. This could dramatically impact the network architecture of the resulting system due to the differences in activation energy between primary and secondary amine for the asymmetric amines.[4] These differences in network connectivity would be most pronounced at the slowest ramp rates because there should be some critical ramp rate and/or critical temperature where primary and secondary amine

reactivity becomes competitive (either from the thermal energy of the oven or the reaction). Below this critical ramp rate/temperature, reaction of primary amine would be favored. While this is not to say that no reaction of secondary amine would occur; it is the opinion of the author that the difference is pronounced enough to make molecular level differences in the polymer network architecture, which will be focus of discussion in the subsequent sections of this chapter.

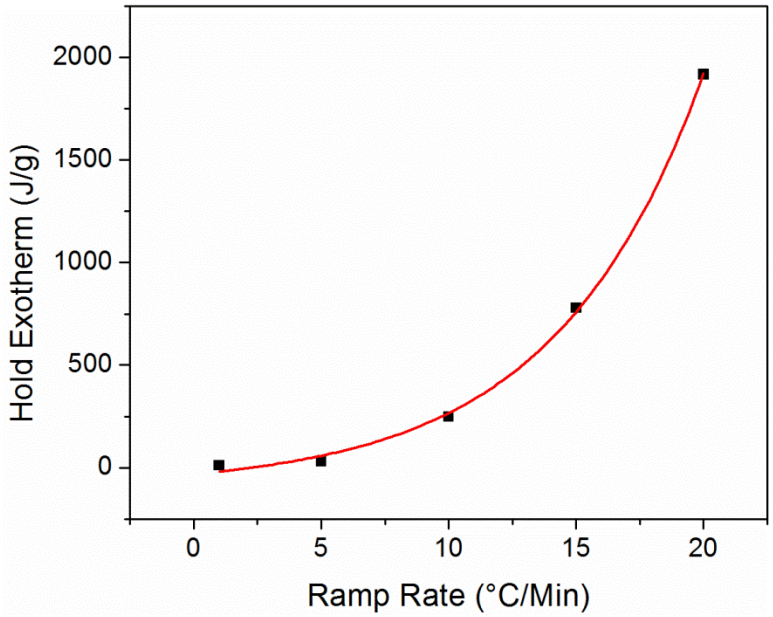

Figure 43. Hold exotherm intensity as a function of cure heating ramp rate. $R^2 = 0.9941$, exponential fit.

While all of the aforementioned data suggest that there could be differences in network growth and the resulting polymer network architecture, it is necessary to determine if the apparent differences will result in macro-molecular differences for the polymer. Thermally, this is most easily observed by measurement of the glass transition temperature, Tg. To determine the glass transition temperature for these materials, a heat/cool/heat DSC experiment was conducted on the heat and hold samples. The Tg

determined was an average between the first and second heating cycles. The observed glass transition temperatures are shown in Table 6. Additionally, a complete cure was verified by the change in the glass transition between the first and second heating cycles. No quantifiable change was observed between the heating cycles.

Table 6

Thermoset polymer glass transition temperature for a series of cure heating ramp rates.

Ramp Rate °C / Min	Tg °C
1	148.82
5	148.49
10	148.39
15	148.26
20	148.67

Iso-Conversional Analysis

In addition to the more standard DSC experiments discussed in the previous section, iso-conversional analysis was also conducted. Essentially, iso-conversional analysis relies on the principle that as you increase the heating rate in the DSC, the peaks will shift to a higher temperature. This allows approximations to the Arrhenius equation to be made and approximations for apparent activation energy to be determined. While the exact method is discussed in Chapter II, it is important to note that the term "apparent activation energy" must be used because the methods employed are only approximations to the Arrhenius equation and not mathematical equivalents.

The FWO plot of natural log of heating ramp rate (β) versus the inverse of temperature (in Kelvin) is shown in Figure 44. A strong linear agreement is found from which the activation energy is calculated as detailed in Chapter II. The KAS plot, which

is a modified form of the FWO equation, is shown in Figure 45. Again, a strong linear agreement is found from which the apparent activation energy is calculated. The apparent activation energies for the FWO and KAS analysis methods were found to be 64.11 and 59.70 kJ/mol, respectively. These two values are similar to previously reported literature on similar epoxy/amine thermoset polymers. [19,75,76]

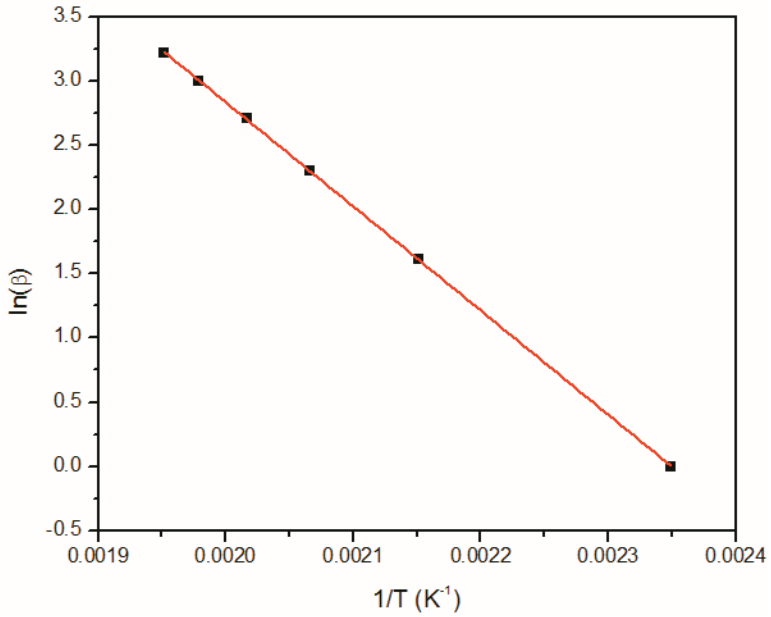

Figure 44. FWO activation energy plot for 33DDS / DGEBF at a variety of cure heating ramp rates. $R^2 = 0.9999$.

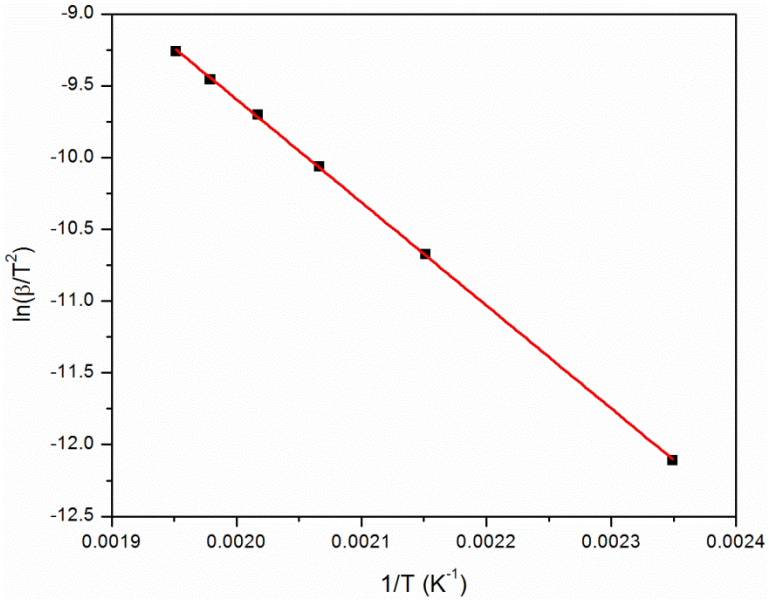

Figure 45. KAS activation energy plot for 33DDS / DGEBF at a variety of cure heating ramp rates. $R^2 = 0.9998$.

In addition to the determination of apparent activation energy for a reaction, iso-conversional analysis can also be applied to show the relative amount of conversion as a function of the current temperature. This is achieved by the integration of the DSC thermograms for every time/temperature. A plot of the relative conversion as a function of temperature for a series of cure heating ramp rates is shown in Figure 46. Initially from the plot, it is observed that all of the ramp rates have a similar shape to them, indicating a similar reaction pathway. Additionally, the iso-conversional analysis confirms previous DSC experiments for reaction completion time and onset of reaction.

While this method is valuable, it does not give strong indications to any molecular level architectural differences for various cure heating ramp rates. However, the application of this method and the high degree of correlation for the FWO and KAS methods support the validity of the original DSC experiments and provide information about how conversion is related to temperature in this polymer matrix.

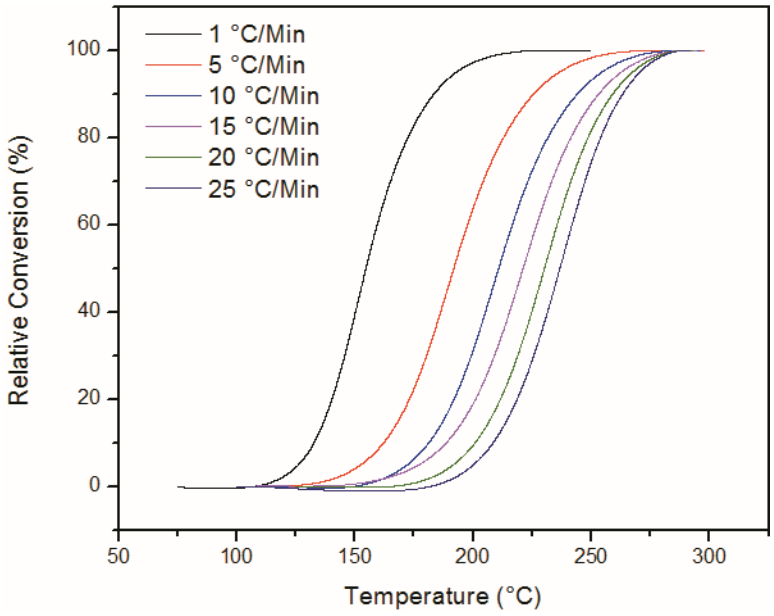

Figure 46. Isoconversional analysis of conversion as a function of temperature for a series of cure heating ramp rates.

NIR Network Growth Analysis

To further explore the nature of matrix network development, NIR was used to monitor concentrations of primary, secondary, and tertiary amines, and epoxide groups concentration as a function of time/temperature. This technique has been proven invaluable as a way to determine both network growth and conversion.[11,15,87] Figure 47 shows plots of concentration of epoxide, primary, secondary, and tertiary amine as a function of time for a series of cure heating ramp rates. All of the plots are similar in behavior; however, as the heating ramp rate is increased, the reaction progresses much more quickly. Despite differences in the apparent kinetic rate of reaction, all systems appear to reach full conversion, within the detection limits of the instrumentation.

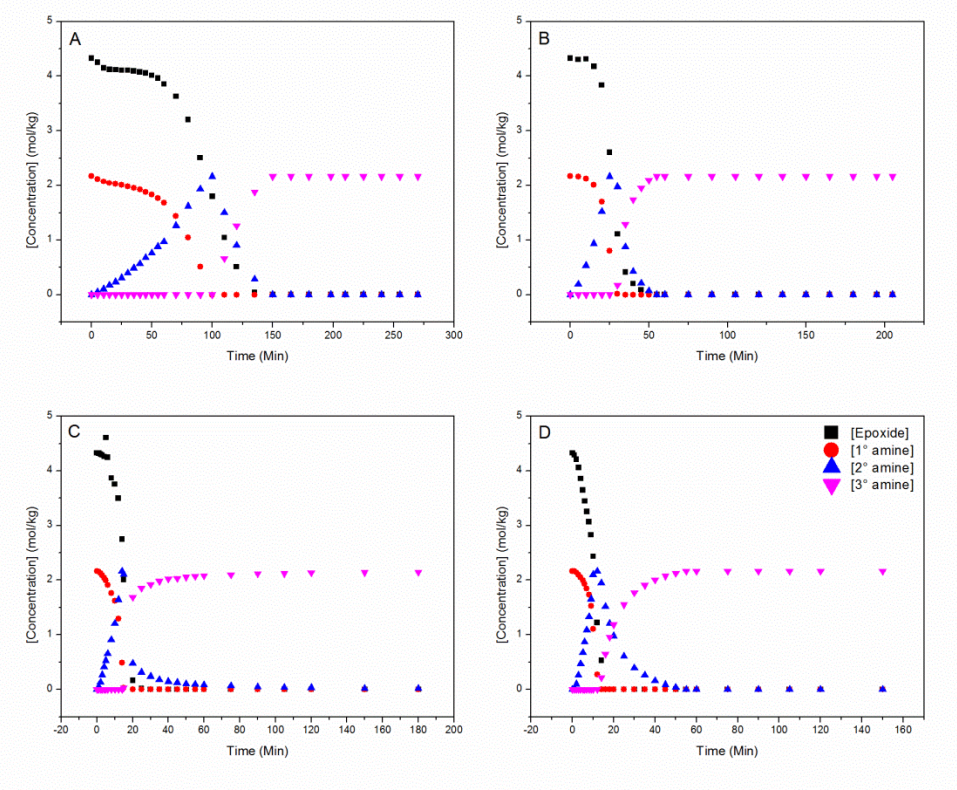

Figure 47. NIR conversion plots of 33DDS/DGEBF curing at a series of ramp rates from 35-180 °C. (a) is 1 °C/min, (b) 5 °C/min, (c) 10 °C/min, and (d) 15 °C/min.

Similar to previously observed experimentation, it appears that the primary amine is mainly consumed before secondary amine. This is inferred from the linear increase in secondary amine concentration over time. In all cases, when the primary amine is completely consumed, the secondary amine begins to be consumed. Even near complete consumption of the primary amine, the secondary amine concentration continues to increase in a linear fashion, despite the substantial increase in statistical likelihood of reaction between epoxide and secondary amine. This suggests that the relative reactivities between primary and secondary amines are not equal in this case, or that the reaction between primary and secondary amines have different energies of activation. Furthermore, this suggests that for the slower ramp rates, on average, a more linear network develops that then cross-links after primary amine conversion. At the faster ramp

rates, it is most likely that the reaction between primary and secondary amines becomes competitive. This is illustrated in Figure 48 and Figure 49 and will be discussed in further detail below.

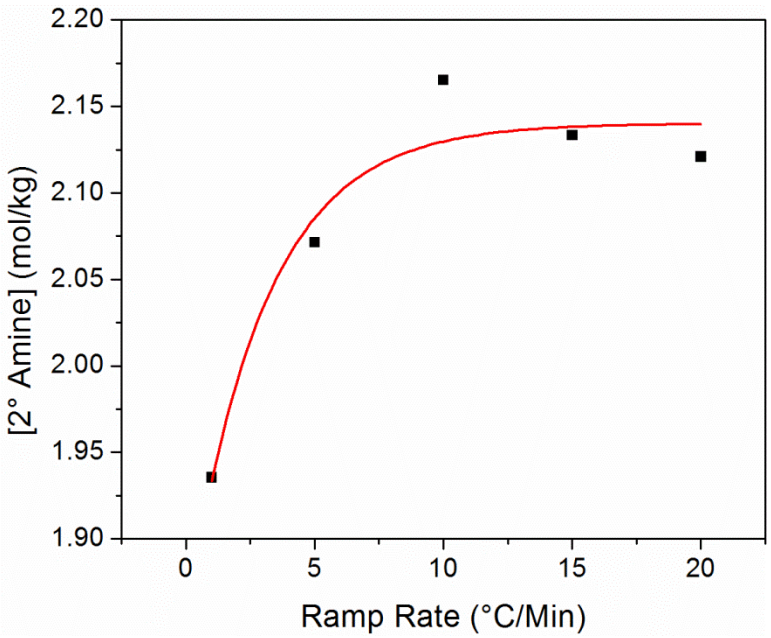

Figure 48. Secondary amine concentration at 75% conversion of primary amine. R^2 = 0.8874, exponential fit.

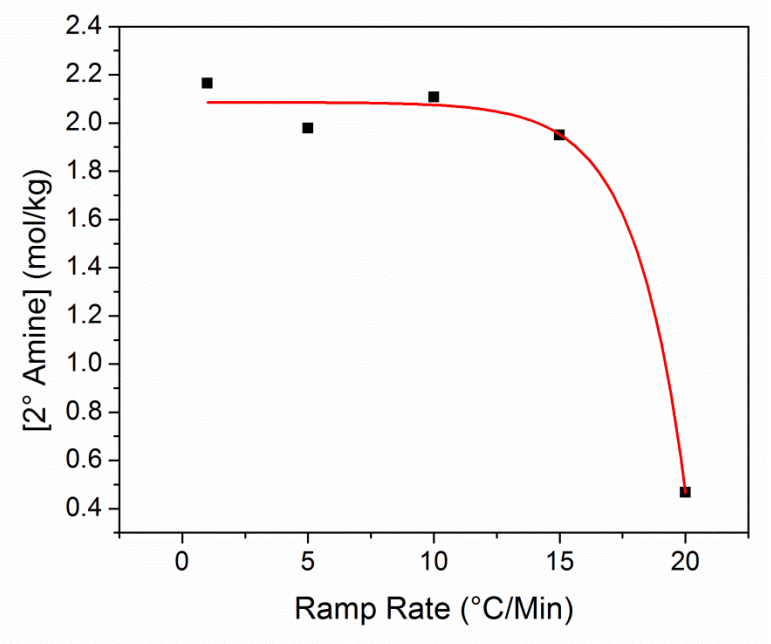

Figure 49. Secondary amine concentration at 95% primary amine conversion. R^2 = 0.9817, exponential fit.

It is believed that the differences in activation energy between the primary and secondary amine reaction with epoxide will cause differences in network growth. As previously suggested, this effect can be identified in Figure 48-49. When monitoring the secondary amine conversion at 75% primary amine conversion, if the networks were growing in exactly the same manner, it would be expected that all networks would have the same concentration of secondary amine. However, this is not the case. Similarly, for secondary amine concentration at 95% conversion of primary amine, all systems would be expected to have the same concentration of secondary amine. While this expectation is more closely satisfied at complete primary amine conversion, there are still substantial differences in secondary amine concentrations. For this to be the case, the networks must be growing in a different manner. To attempt to validate the previous hypothesis of a more linear network growth in the slower ramp rate systems, the tertiary amine concentration must also be monitored. Shown in Figure 50 is a plot of tertiary amine concentration at 75% secondary amine conversion. For the slowest ramp rate system, the most well-defined pattern of network growth emerges. As expected at 75% secondary amine conversion, approximately 80% of the maximum possible tertiary amine is achieved. A one-to-one correlation would suggest that a perfectly linear system, which then cross-links, is generated. However, for the faster ramp rates, the concentration of tertiary amine decreases. As amine can only be primary, secondary, or tertiary, this implies that there must be more primary amine present in the system while secondary amines are reacting, indicating a more globular network growth.

Despite differences in network growth and formation, all of the cure ramp rates explored achieve full conversion to tertiary amine. This is best illustrated in Figure 51 which shows a plot of tertiary amine concentration as a function of both cure ramp rate

and secondary amine concentration. The plot indicates that, while the rate of coversion is different with cure ramp rate, eventually the polymers all achieve full conversion and would have the same overall cross-link density which accounts for the similar glass transition temperatures observed via DSC. Thus, if a cure rate dependence is observed for this matrix polymer, it must exist on a size scale smaller than either NIR or DSC can determine. As a result, dielectric spectroscopy and free volume hole size characterization were used to probe the molecular level size scale.

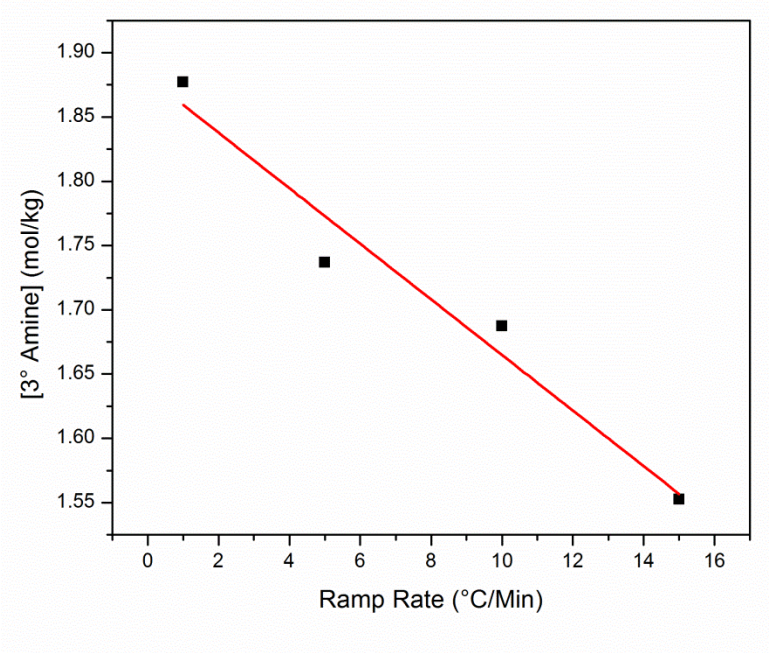

Figure 50. Tertiary amine concentration at 75% secondary amine conversion. $R^2 = 0.9399$, exponential fit.

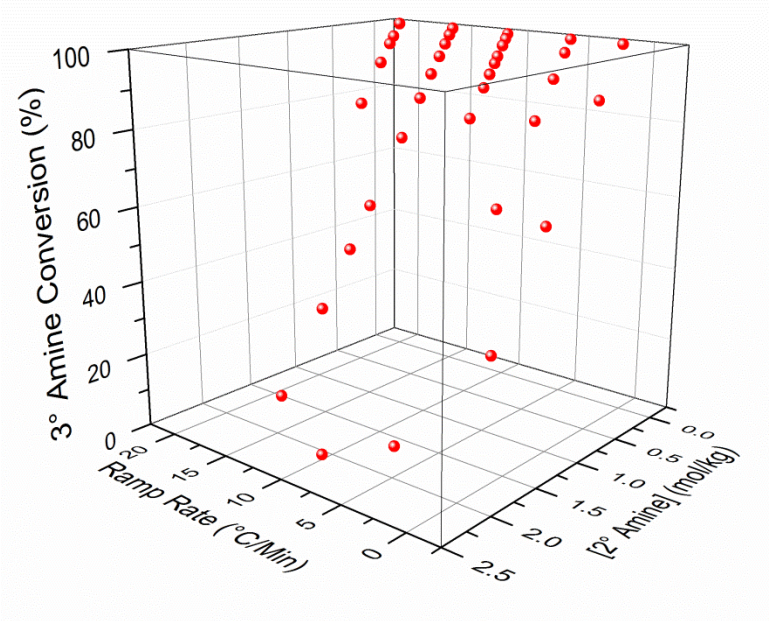

Figure 51. Tertiary amine concentration plotted as a function of both cure heating ramp rate and secondary amine concentration. $R^2 = 0.9998$, 2D surface fit.

Density Cure Rate Dependence

In addition to a thermal (DSC) and NIR spectroscopic investigation of polymer growth, a study of the final polymer properties is necessary to determine a cure heating rate dependence. As the glass transition temperatures for these polymers are similar, but the NIR suggests that the networks are growing differently, the first analysis method to explore a difference that was employed was density determination. As mentioned in Chapter II, the density measurements were conducted through collaboration with Deakin University on an ultrapycnometer. An interesting trend with density and cure heating ramp rate was observed and is shown in Figure 52. While the variation in density may seem small, it could have significant effects on the free volume and molecular level rotations of these polymers. It is interesting that the density initially decreases and then slowly begins to increase with increasing ramp rate. This supports the researcher's theory of network growth. As the polymers switch from a more linear type growth to a globular

growth, the chain packing of the polymers is altered causing a reduction of density at lower ramp rates. At higher ramp rates, the number of globular structures forming has become so large that the density starts to increase due to very tight chain packing in the system. If this is the case then, a similar observation with the free volume characteristics will be observed, and differences in short range molecular motions should also be observed via DES.

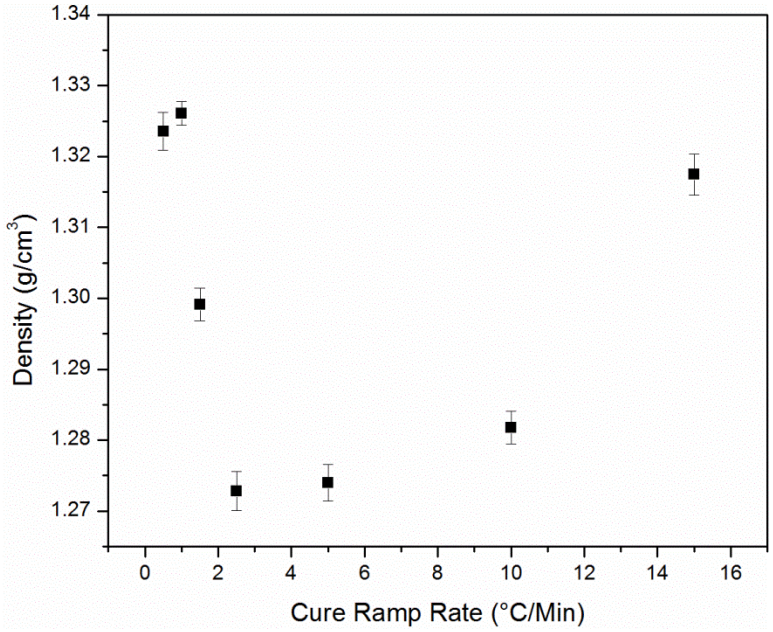

Figure 52. Density as a function of cure heating ramp rate.

Free Volume Hole Size Analysis

To determine if there are local differences in polymer network growth and final structure, the most effective way to observe any changes is by determination of the free volume average hole size, Vh. Inherently, there is always empty space (free volume) between atoms, and this is observed using Positron Annihilation Lifetime Spectroscopy (PALS). In PALS, a positron is generated which will interact with the matter around it. As a result of the lifetime of this interaction, the Vh can be calculated using a variety of models. The Vh for each cure heating ramp rate is shown below in Figure 53. While

changes from approximately 65 to 50 $Å^3$ may seem minimal, this can have a large effect on macro-scale properties such as solvent uptake.[11,15]

When looking at the network growth data in conjunction with the PALS analysis, specifically the NIR data, the differences in Vh can be explained. As discussed in the NIR section, at the slower ramp rates, there is most likely a major portion of the ramp rate where the activation energy for secondary amine conversion has not been overcome. In this case, the network would, on average, grow in a more linear manner that would cross-link after the activation energy barrier was overcome at high temperatures. For the fast heating ramp rates, the primary and secondary amine reactions would, on average, occur simultaneously. If this occurs, then a more globular network growth would be observed, and a difference in free volume would be found over the slower ramp rates that would show a more linear type network growth. This phenomenon would account for the changes in Vh. Interestingly though, where the DSC data suggests that it is the exotherm of the reaction driving conversion at ramp rates above 10 °C/min, there is a difference between the Vh for the 10 and 15 °C/min samples. The author attributes this to an increase in the number of nucleation sites for reaction at the very high ramp rates leading to an increased number of regions with increased free volume between them.

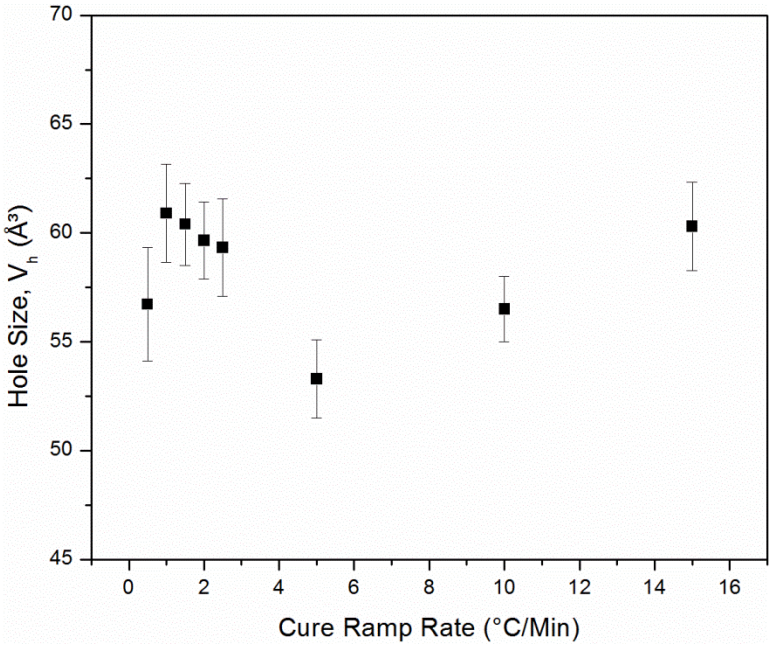

Figure 53. Free volume hole size, Vh, for a series of cure heating ramp rates. Hole sizes shown were determined at room temperature.

Preliminary DES Analysis

While the majority of the broadband and *in situ* dielectric analysis will be discussed in the subsequent chapter, it is important to introduce it here in the context of network growth and formation. Based on the results from the NIR, free volume, and density already discussed, there is considerable support for molecular level differences in polymer network architecture while maintaining similar overall cross-link density in the polymers. If this is truly the case, then B-DES should be able to observe differences in the molecular scale relaxations of the network polymers.

Figure 54 shows the B-DES spectra for six different cure heating ramp rates at both 1 Hz and 1 kHz. Both frequencies are shown to illustrate the differences in time scale of these relaxations. On the figure, each of the regions is labeled, and similar peak shapes and maxima are observed for the Tg region, corroborating the DSC data. However, for both the β and γ relaxations, the peak shapes and maxima change with

respect to cure heating ramp rate. This phenomenon is more easily observed in Figure 55. As the heating ramp rate increases, a distinct change in peak shape for the β transition is observed at 1 kHz. Similarly, as heating ramp rate increases, an upward shift in relaxation temperature is observed for the γ transitions. As previously mentioned, the impact of the changes in relaxation time with respect to molecular architecture will be discussed in greater detail in the next chapter; however, it is sufficient to qualitatively conclude that the short range molecular motions for these network polymers have a dependence on cure heating ramp rate and warrants further study with DES.

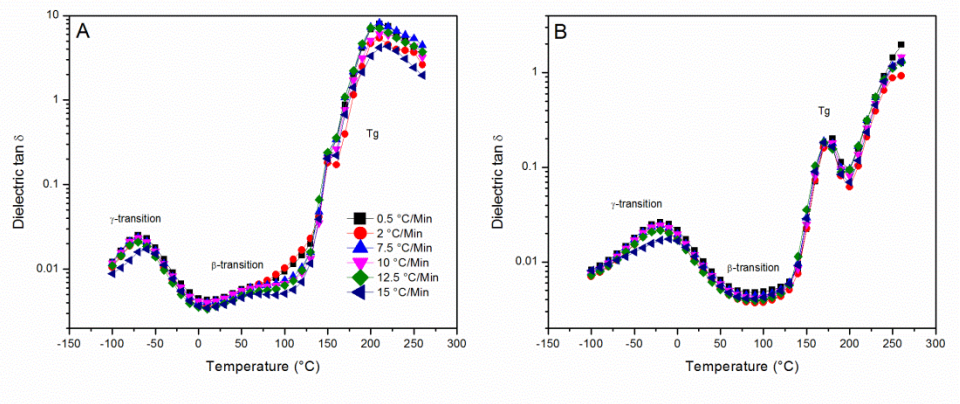

Figure 54. Broadband DES spectra at (a) 1 Hz and (b) 1 kHz for a series of cure heating ramp rates.

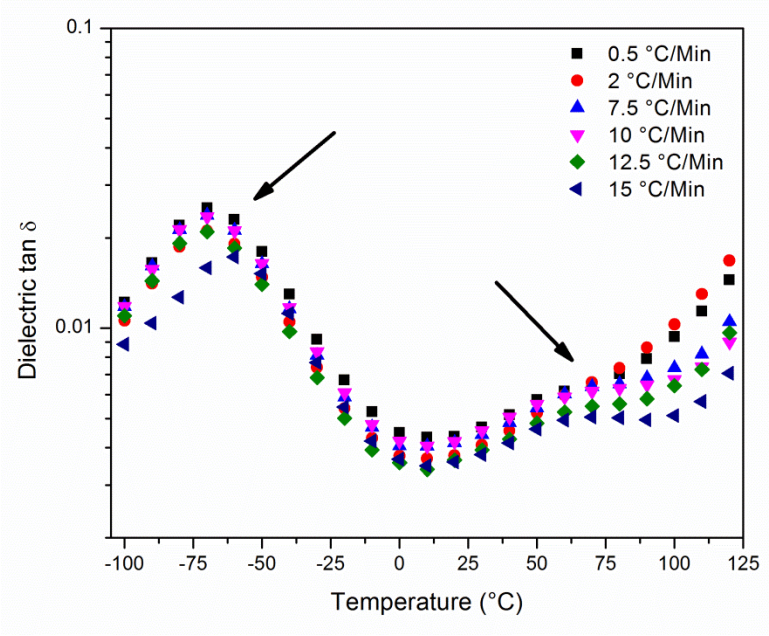

Figure 55. Broadband DES spectra at 1 kHz highlighting differences between the (left) gamma transition and the (right) beta transition for several cure heating ramp rates.

Summary

In conclusion, it has been determined that there does exist a cure heating rate dependence for thermoset polymer matrix polymers. The cure rate dependence that exists for this polymer was found to be on a molecular level. The free volume hole size, density, and network growth were all found to be significantly impacted by cure heating ramp rate. Differences in molecular motions were qualitatively observed via DES and will be discussed further in the next chapter of this work. The impact of this dependence may, however, be chemistry specific, which will be explored in subsequent work.

CHAPTER VI

DIFUNCTIONAL EPOXIDE CURE RATE DEPENDENCE CHARACTERIZED BY DIELECTRIC SPECTROSCOPY

Objective

The purpose of this chapter is to introduce and discuss an in-depth analysis of the DES data and results in light of the information learned from the previous chapter of this dissertation. This chapter will use dielectric spectroscopy to solidify some conclusions previously drawn. Specifically, this chapter will reinforce the hypothesis that there is a molecular size scale dependence on the cure heating ramp rate of thermoset polymers based on the chemistry of DGEBF/33DDS. Of importance in this discussion will be the α transition, the distribution of relaxation times of the α transition, and the γ transition. Additionally, *in situ* dielectric analysis will also be introduced to reinforce conclusions drawn in the previous chapter. Finally, this chapter will conclude with a summary of the cure rate dependence of di-functional epoxide thermoset polymers and a hypothesis for network growth as it relates to the cure heating ramp rate of this polymer matrix.

Results and Discussion

DES Spectra Analysis

Dielectric analysis was employed with the goal of determining if the molecular architecture and any molecular level motions are dependent on the cure heating ramp rate. To do this, dielectric spectra were collected at a variety of temperatures and frequencies ranging from -70 to 250 °C and 0.001 Hz to 1 MHz. By varying both the temperature and frequency in a systematic manner, both short range (generally fast) and longer range (generally slower) molecular motions can be observed.

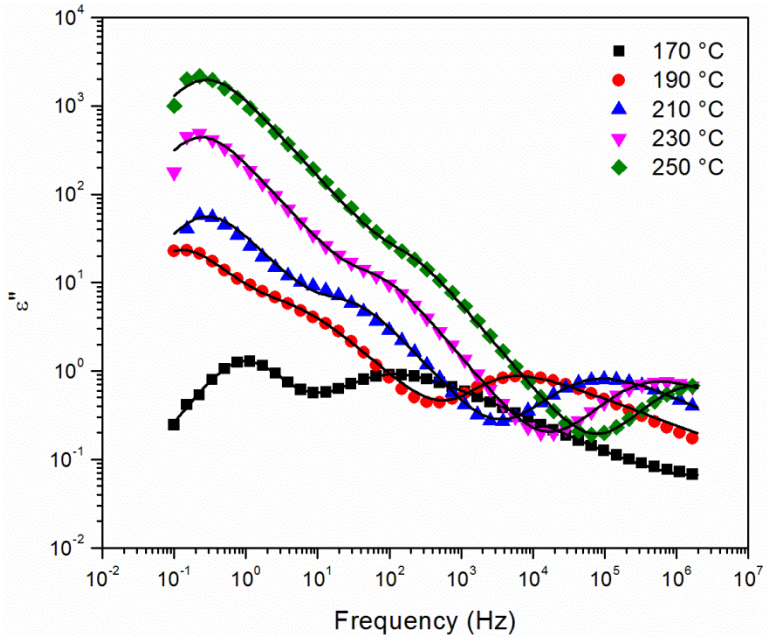

Figure 56. Dielectric loss vs frequency for DGEBF/33DDS at various temperatures. Cure rate of 0.5 °C/min. Fitting lines are the HN fit.

While the dielectric spectra for the temperature sweep at a constant frequency has been shown in the previous chapter, the spectra for the frequency sweep at a series of temperatures for the 0.5 °C/min sample are shown in Figure 56. The figure shows a shift to higher frequency of the relaxation peak maxima, which is common for glassy state polymers. Additionally, there are two peaks at lower frequencies that cannot be resolved without the implementation of the HN fit (described in Chapter II) and will be discussed in the Peak Assignments section of this chapter.

Figure 57 shows the plot of dielectric loss versus frequency at several cure heating ramp rates. Similarly, to the dielectric storage peak, the HN analysis was conducted and the fitting lines are shown for the dielectric loss. As the cure heating ramp rate is increased, both peaks increase in intensity, and the higher frequency peak shifts slightly to an even higher frequency. This means that as the ramp rate is increased, the molecular motions occur more rapidly. This could be due to a reduction in free volume or

changes in the relaxation time distribution. When increasing the analysis temperature to 210 °C (Figure 58), a third peak becomes evident, but also the electrode polarization increases. In the figure at low frequencies, a large increase in dielectric loss is observed; this is caused by the electrode polarization. Despite the evidence of electrode polarization, three peaks are still found in the HN analysis of the sample. Causes and implications for these peaks will be discussed in the next section.

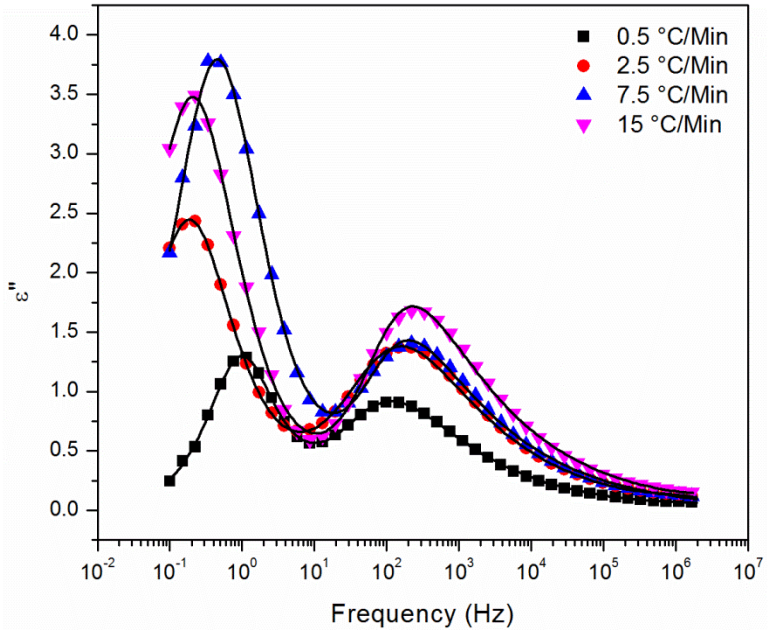

Figure 57. Dielectric loss vs frequency for DGEBF/33DDS at 170 °Cfor various cure rates. Fitting lines are the HN fit.

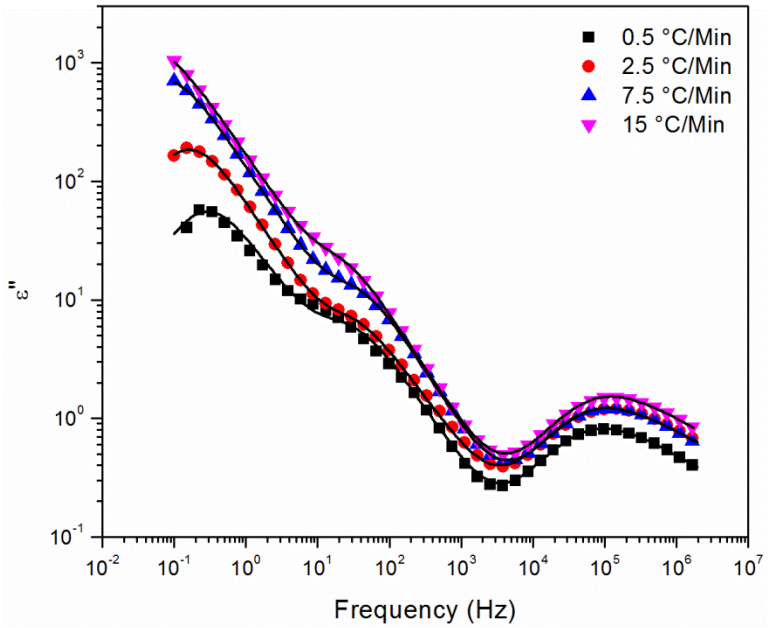

Figure 58. Dielectric loss vs frequency for DGEBF/33DDS at 210 °Cfor various cure rates. Fitting lines are the HN fit.

To prove that the increase in both dielectric loss and storage at low frequencies is due to electrode polarization, three-dimensional plots of either storage or loss versus frequency and temperature were generated. These plots allow for the resolution of both peaks growing with temperature, but also the determination of the temperature at which electrode polarization occurs. Specifically, the peaks for molecular motion are most evident in the dielectric loss plots and the electrode polarization in the dielectric storage plots. These plots are shown over the next several pages in Figure 59 and Figure 60 for the 0.5 °C/min samples; Figure 61 and Figure 62 for the 7.5 °C/min samples; Figure 63 and Figure 64 for the 10 °C/min; and finally, Figure 65 and Figure 66 for the 15 °C/min samples. While the analysis of each figure is similar, all were included for completeness.

In the 0.5 °C/min samples, the dielectric storage plots at low temperature are independent of frequency. As the temperature is increased closer to the glass transition temperature, a peak does appear to grow, but most important is the peak for the highest

temperature below the Tg (140 °C). The dielectric storage is almost constant except for a large increase at the very lowest frequencies. This is a classic representation of electrode polarization and is evident for all of the samples. Once the presence of electrode polarization is confirmed, the HN fitting analysis can then remove it from the calculations of the characteristic relaxation time.

As previously mentioned, the dielectric loss plots are useful for determining any transitions as changes to, or additions of peaks are more easily identified. In the case of all heating ramps, a new peak can be found forming at around the glass transition temperature. The HN analysis at this temperature will then yield the characteristic relaxation time for each sample.

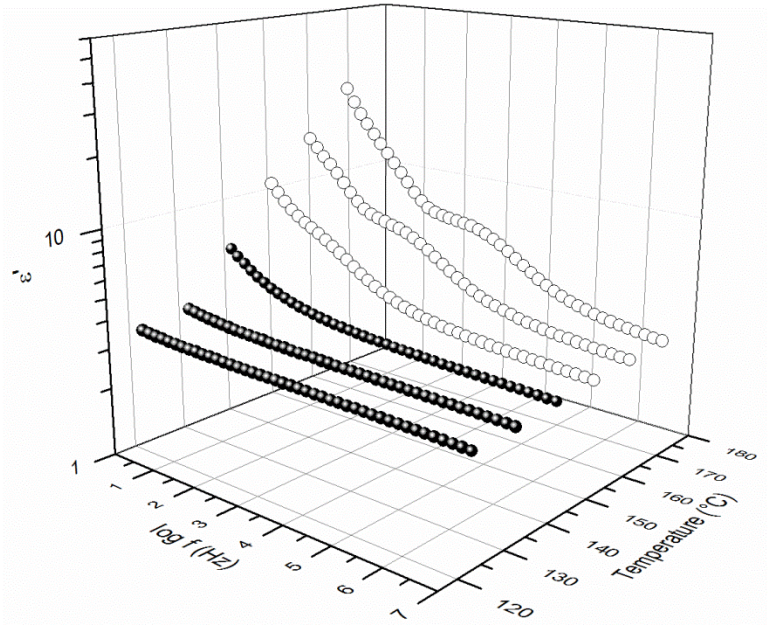

Figure 59. Plot of dielectric storage vs frequency and temperature for a 0.5 °C/min cure rate.

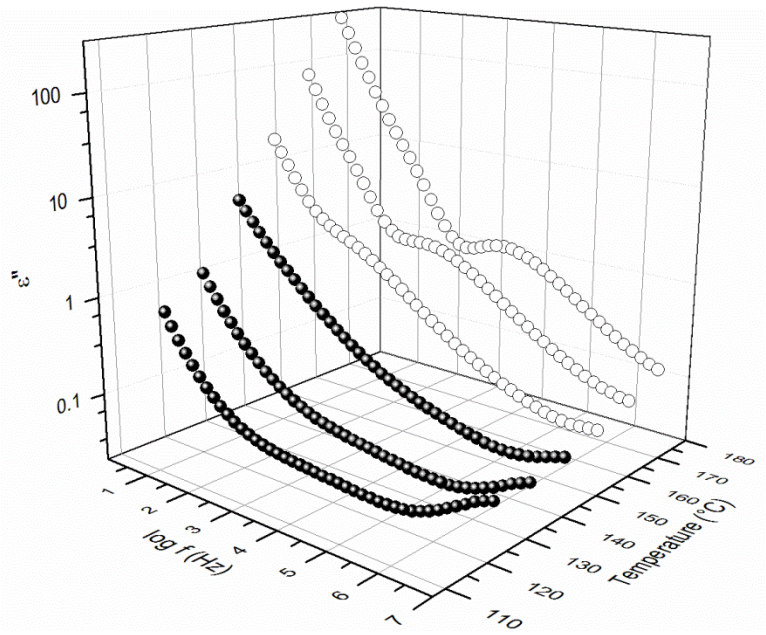

Figure 60. Plot of dielectric loss vs frequency and temperature for a 0.5 °C/min cure rate.

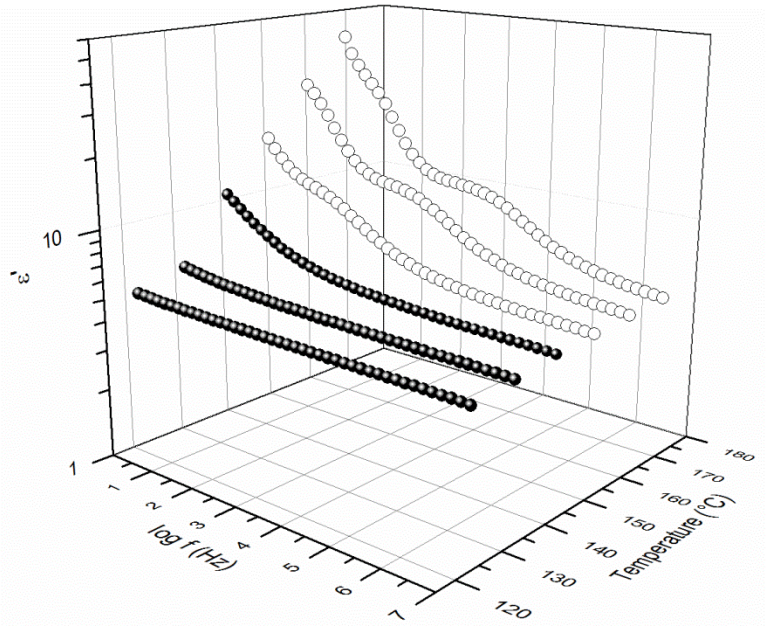

Figure 61. Plot of dielectric storage vs frequency and temperature for a 7.5 °C/min cure rate.

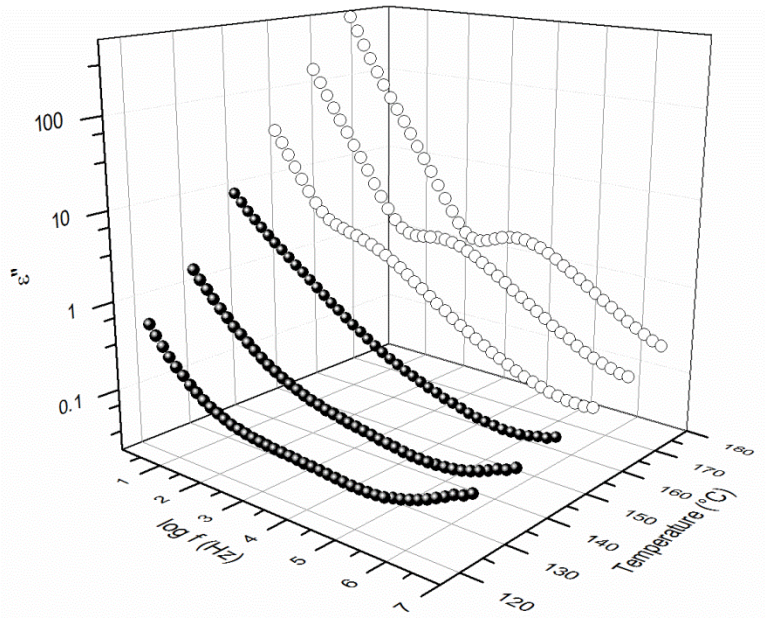

Figure 62. Plot of dielectric loss vs frequency and temperature for a 7.5 °C/min cure rate.

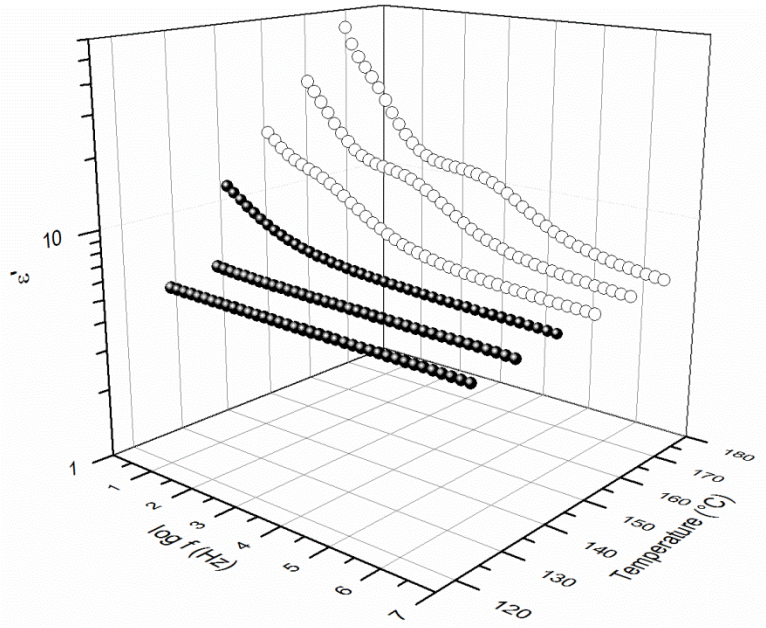

Figure 63. Plot of dielectric storage vs frequency and temperature for a 10.0 °C/min cure rate.

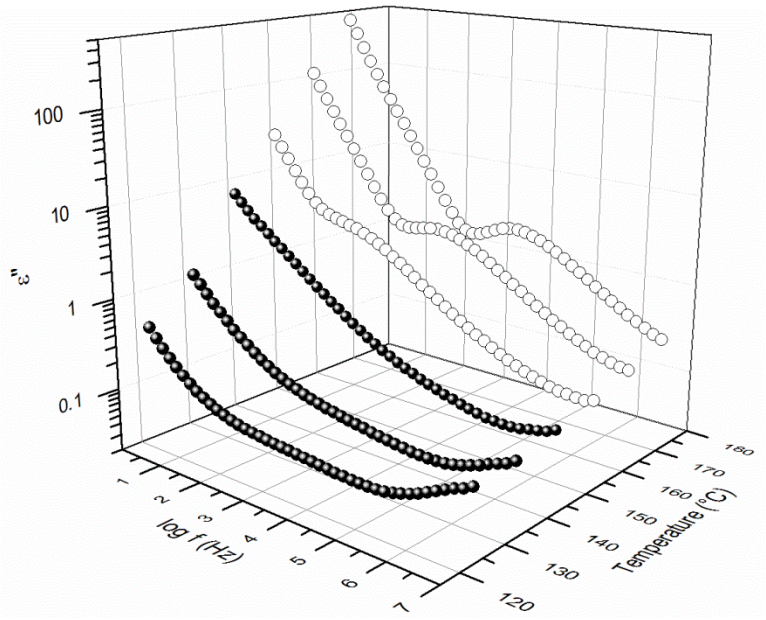

Figure 64. Plot of dielectric loss vs frequency and temperature for a 10.0 °C/min cure rate.

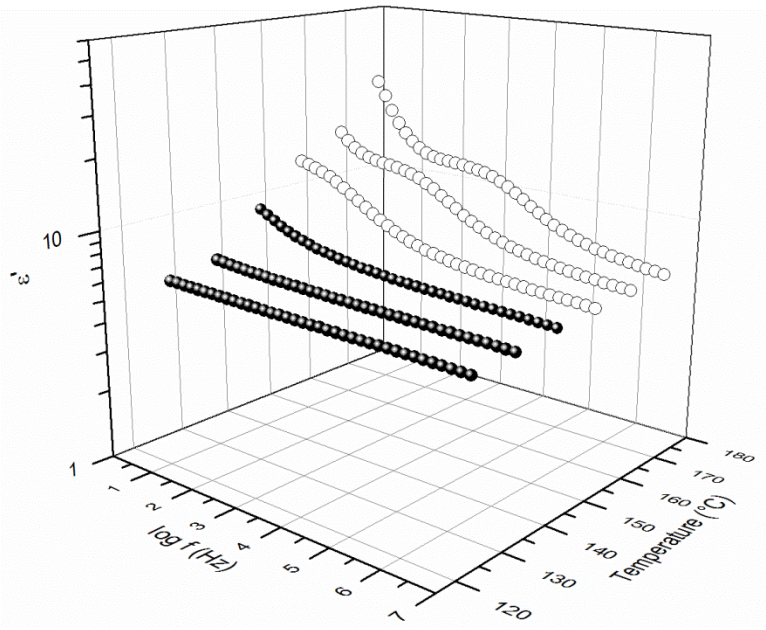

Figure 65. Plot of dielectric storage vs frequency and temperature for a 15.0 °C/min cure rate.

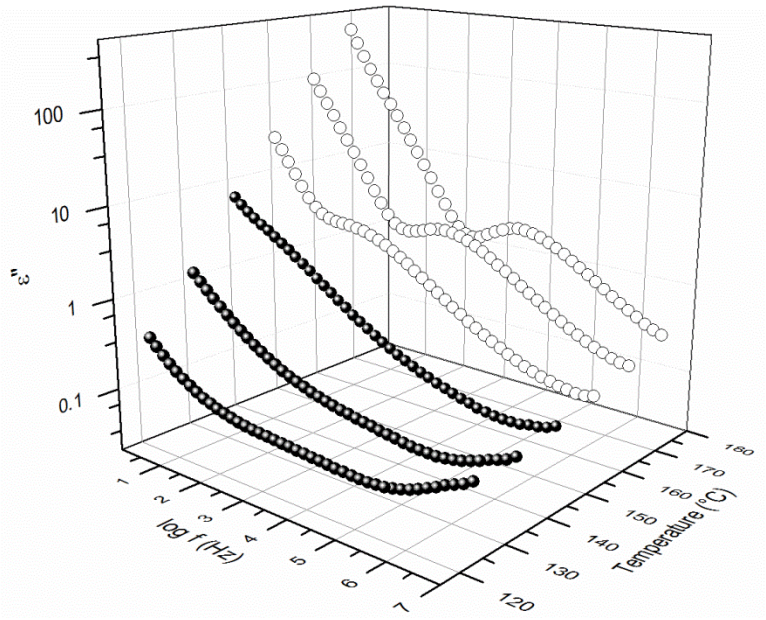

Figure 66. Plot of dielectric loss vs frequency and temperature for a 15.0 °C/min cure rate.

DES Peak Assignments

For the entire range of cure heating ramp rates, the characteristic relaxation time, τ_{Max}, was calculated from the HN equation fitting of the data. It was found that there were three characteristic peaks for the glass transition (refer to Figure 58). To determine the type of relaxation associated with each peak, a series of analysis methods were employed, beginning with the standard fitting for the glass transition. For the peak labeled Tg_1, T\the τ_{Max} data was plotted versus the reciprocal of temperature and fitted with the Vogel-Fulcher-Tamman-Hesse (VFTH) equation as follows:[88]

$$\tau_{Max} = \tau_0 \exp\left(\frac{E_a}{[k_b(T - T_v)]}\right)$$

where k_b is the Boltzmann constant, τ_0 is the relaxation time at infinite temperature, Ea an apparent activation energy for the motion, and Tv is the Vogel temperature. The Vogel temperature is considered to be the glass transition temperature that would be observed if the polymer were to be cooled at an infinitely slow rate. The plot of τ_{Max} data was then

plotted versus the reciprocal of temperature to assign the transition. The plot is shown below in Figure 67. The data was found to follow the VFTH fitting, and the calculated Vogel temperatures are shown in Table 7.

It was found through the fitting that the first peak analyzed, Tg_1, is then the transition associated with the glass transition temperature and long range cooperative molecular motion. In all cases, the Vogel temperatures were very similar, as were the curve parameters, indicating that the chain motions for the glass transitions were similar. This is consistent with the previously conducted DSC experiments which also suggested similar glass transition temperatures.

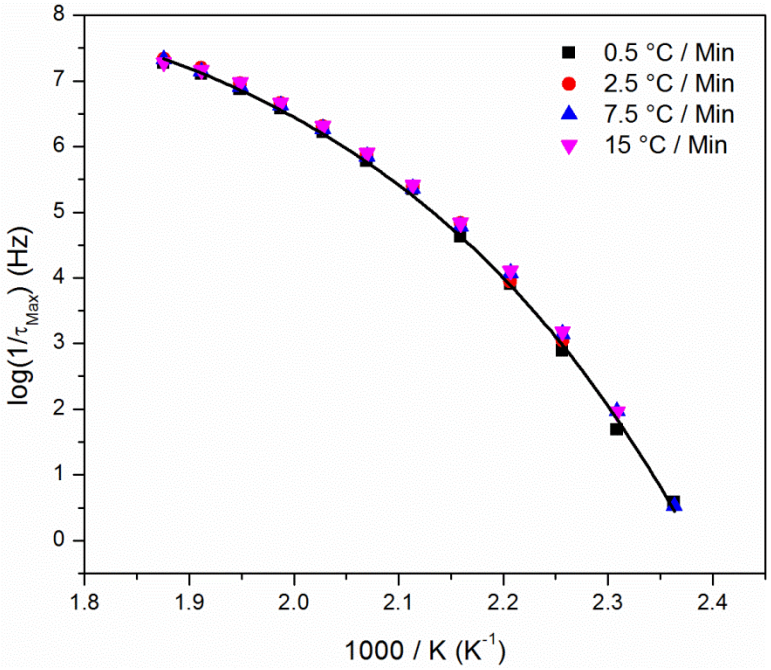

Figure 67. VFW plot of peak Tg_1 for a series of cure heating ramp rates.

Table 7

Tv for matrix polymers of various heating ramp rate.

Ramp Rate °C/Min	Tv °C
0.5	146.88
2.5	148.84
7.5	145.84
15	143.19

Calculated from the VFW fit of peak Tg_1.

The second peak found in the glass transition temperature region, labeled Tg_2, was also plotted versus reciprocal temperature, and is shown in Figure 68. Unlike the previous transition that was found to follow VFTH fitting, this plot is linear, indicating an Arrhenius relationship. Since the data does not follow the Vogel relationship, the cause of this peak is unclear and could either be a result of electrode polarization or a molecular motion. Due to the strong Arrhenius dependence of this peak, however, the peak is most likely associated with a molecular motion. Utilizing the Arrhenius relationship, the activation energies associated with each cure heating ramp rate are shown in Table 8.

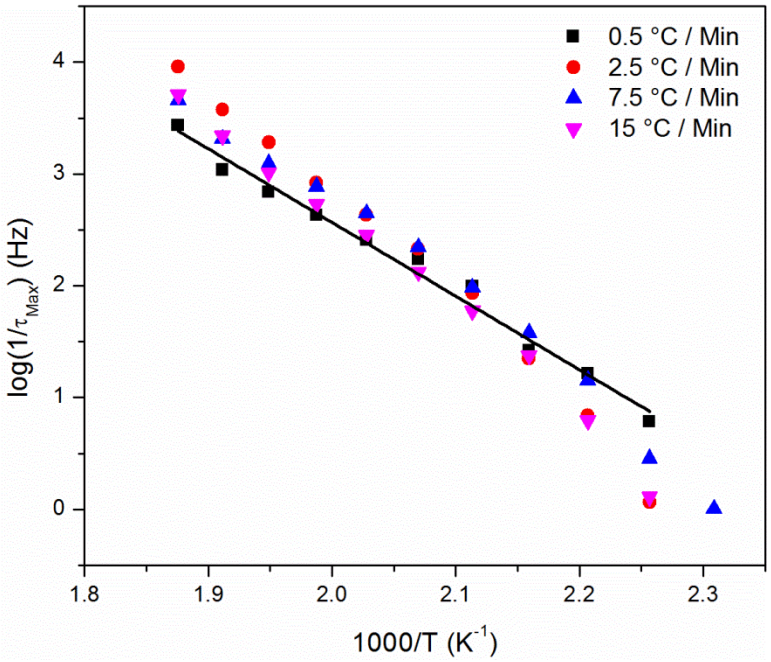

Figure 68. Arrhenius plot of peak Tg_2 for a series of cure heating ramp rates.

In this case, the activation energies do seem to vary greatly between the samples; however, no correlation was found, indicating that the differences were more than experimental error associated with variations in sample thickness and instrumental error. Despite these changes, however, the general region for the activation energies for these molecular motions is in line with those previously reported. [12]

Table 8

Activation energy and residual fit for a series of cure heating ramp rates.

Ramp Rate °C/Min	Ea kJ/mol	Fit R^2 ---
0.5	125.97	0.9854
2.5	185.25	0.9854
7.5	157.44	0.9822
15	169.72	0.9871

Finally, the plots of all three peaks were combined together to determine the cause of the third peak (labeled MWS in the figure) and are shown in Figure 69. Displayed in this plot, the VFTH dependence of Tg_1 and the Arrhenius dependence of Tg_2 are again observed. The third peak is also seen in this plot and has been attributed to Maxwell-Wagner-Sellars, or MWS, polarization. The assignment is made due to the linearity associated with the curve combined with the small change in the associated τ_{Max} when compared to the other two peaks. The existence of a MWS polarization is encouraging in that MWS polarization only occurs when electric charge builds up internally in the sample, (i.e. not at the electrode interface) and must be a result of heterogeneity within the network structure. While the specific heterogeneities cannot be identified by this specific method, the fact that they exist and were present in all samples indicates that there must be regions within the matrix polymer of high cross-link density and regions of different cross-link density. This then may help to explain the differences in the relaxation distribution function that will be introduced in the subsequent section of this chapter.

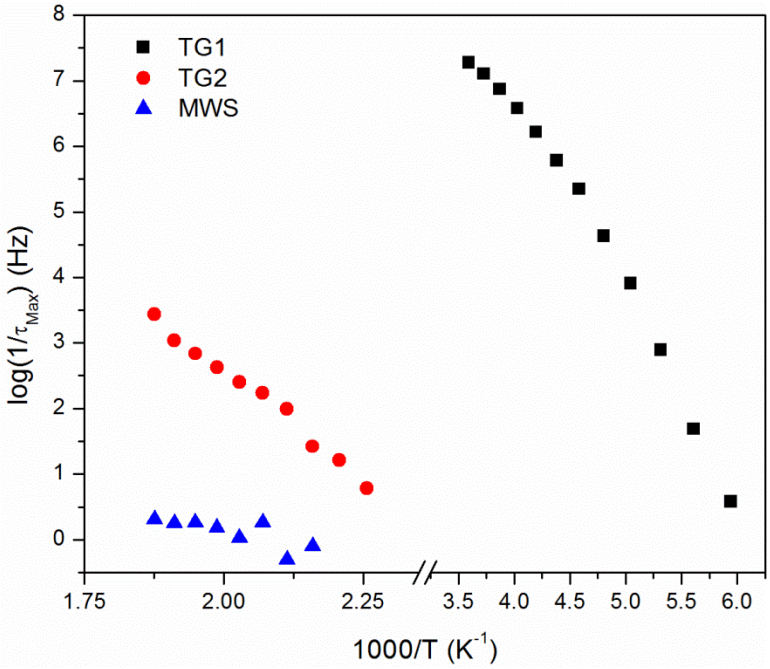

Figure 69. τ_{Max} plot for the 0.5 °C/min cure ramp rate sample.

Relaxation Time Distribution

By using the HN equation to fit the data for the glass transition peak, or the α transition peak, it is also possible to calculate a distribution of the relaxation times for that specific transition. The distribution of relaxation times, also referred to as G(τ), can easily show differences between the same transition for different cure heating ramp rates, by showing a change in either intensity, peak maxima, or addition/subtraction of peaks. For this work, the relaxation time distribution has been calculated at two temperatures, the glass transition temperature and 210 °C. The second temperature was chosen because it is well above the Tg and is representative of molecular motion at elevated temperatures. The plot for the relaxation time distribution at 170 °C is shown in Figure 70. This figure illustrates well the molecular level differences that are present when curing at different ramp rates and can also be used to help understand the free volume data presented in the previous chapter.

Figure 70 shows the addition of a new peak in the relaxation time distribution as the cure heating ramp rate is increased and a slight shift in the peak at approximately 10^{-3} sec. First and foremost, this data strongly supports the hypothesis that the polymer network architecture is different for each of the cure heating ramp rates, at least on a short range size scale The data also suggests that the modes of molecular motion at the glass transition temperature are different for each heating ramp rate. This data together suggests that although the temperature of the molecular motion and the transition are the same, the local environments of the reacted monomers within the network are different, and as the ramp rate is increased, the motions become more varied. Ultimately, this difference could have an impact on the mechanical performance and free volume characteristics at elevated temperatures.

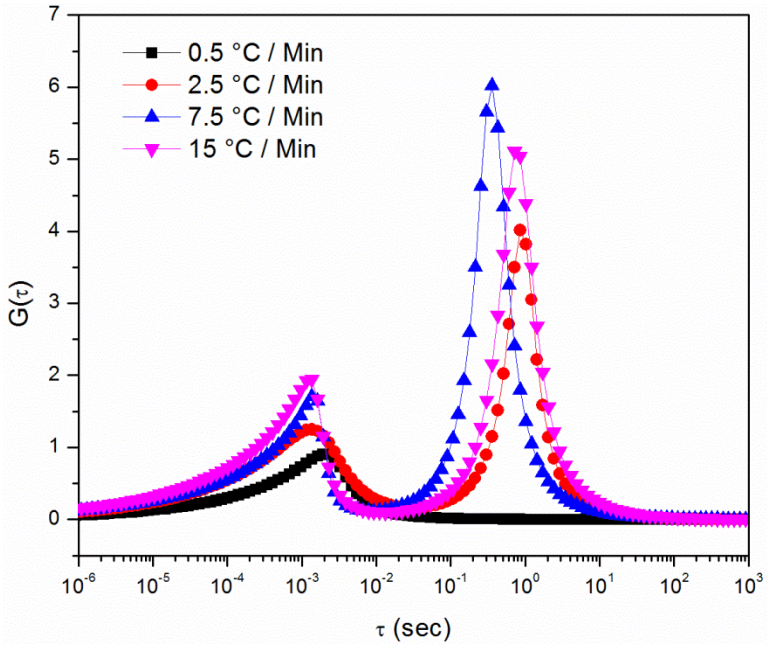

Figure 70. G(τ) at 170 °C for 0.5 °C/min cure heating ramp rate.

In addition to the relaxation time distribution at 170 °C, the distribution at 210 °C was calculated and is shown in Figure 71 and Figure 72. The distributions are for the same set of data; however, they have been split to be able to see the entirety of the data as the distribution for Tg_1 is several orders of magnitude higher than Tg_2 at this temperature. As with the lower temperature distribution, the higher temperature distributions clearly show a dependence on cure heating ramp rate. For the Tg_1 peak (Figure 71), the intensity, peak maxima, and peak height all increase with increasing cure heating ramp rate. This supports the hypothesis of an increase in network heterogeneity with increasing heating ramp rate. Essentially, the networks grow so quickly that they are not able to reorganize into their most efficient state (lowest energy) before being locked in due to the speed of the reaction. This makes the local environments very different from one another at the faster heating ramp rates, again suggesting that short range molecular events such as free volume or fluid sensitivity may be greatly impacted by the cure heating ramp rate. The peak for Tg_2 at 210 °C also shows a similar trend to Tg_1 with increasing intensity for increasing ramp rate. However, in this case, the peak maxima position does not change greatly for the network.

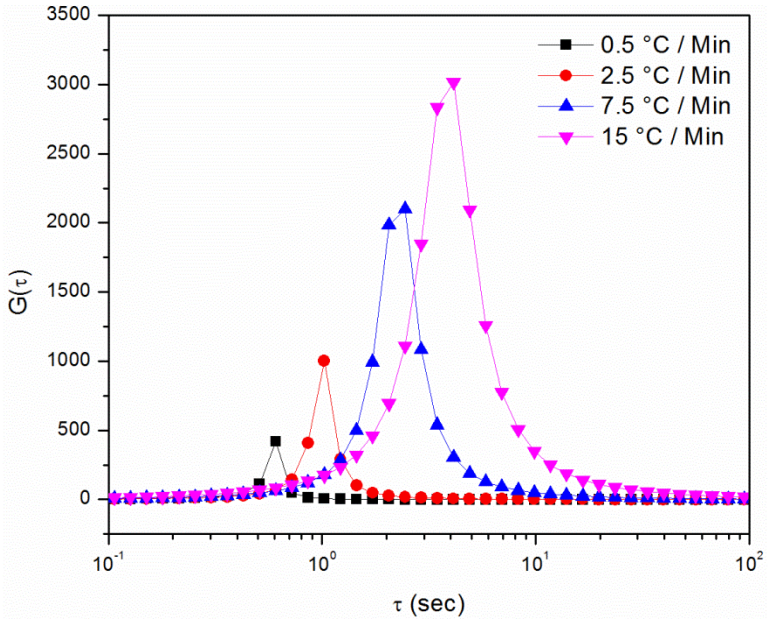

Figure 71. G(τ) at 210 °C for 0.5 °C/min cure heating ramp rate, peak Tg_1.

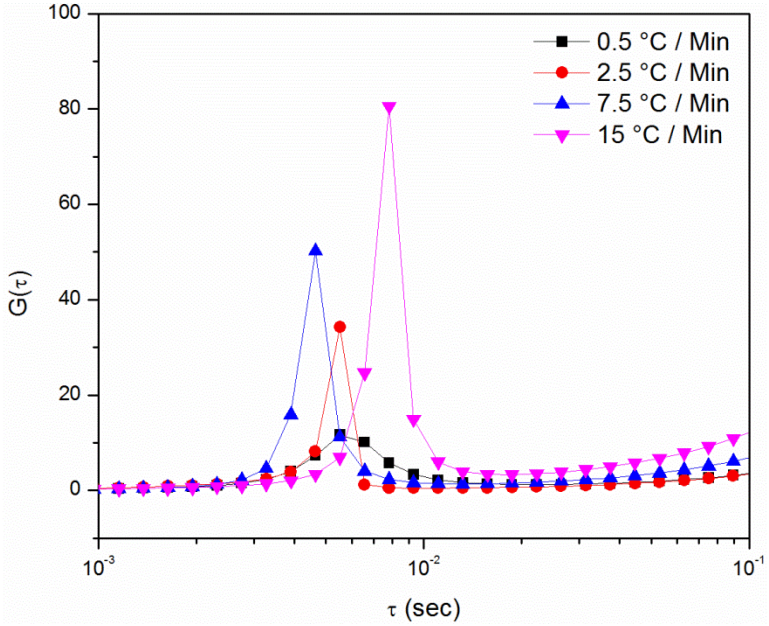

Figure 72. G(τ) at 210 °C for 0.5 °C/min cure heating ramp rate, peak Tg_2.

γ Relaxation

While the primary transition is of importance to study for thermoset polymer networks, they will be utilized well below their glass transition temperature, and thus understanding the secondary transitions and their molecular motions are also vital for evaluating the mechanical performance of these polymers. Specifically, it is reported that this transition involves as few as four carbon atoms,[89] and can play a significant role in the mechanical relaxation of these materials. At the end of the previous chapter were introduced two DES figures. In both of those figures, multiple transitions are visible; further, these transitions appear to be slightly different with varying cure heating ramp rate. A plot of the γ relaxation loss is shown below in Figure 73, with respect to frequency and temperature for the 0.5 °C/min heating ramp rate.

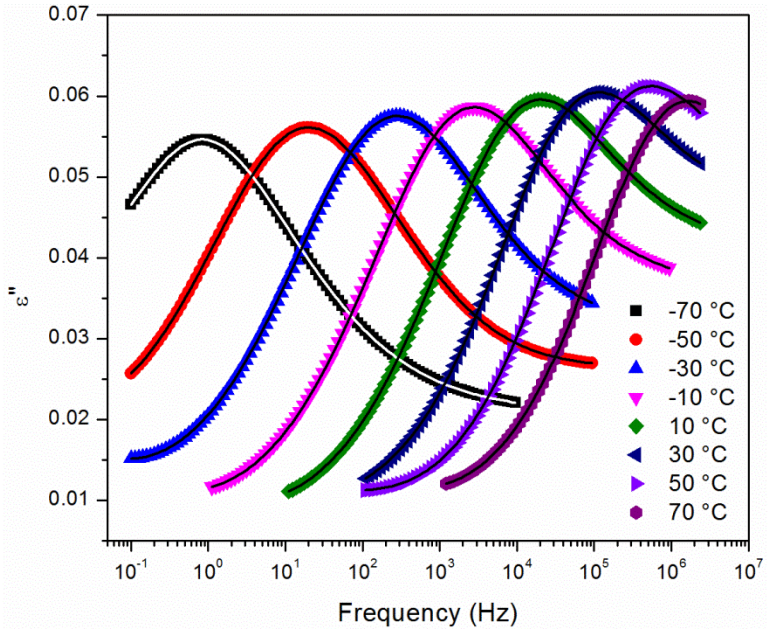

Figure 73. γ relaxation dielectric loss vs temperature.

This standard plot can then be reformatted into an Arrhenius plot for the transition, and an activation energy be calculated. The Arrhenius plot for each cure heating ramp rate is shown in Figure 74, and the activation energies tabulated in Table 9.

It was found that all of the activation energies for this molecular motion were similar to one another. This is not entirely unexpected because the specific motions occurring are identical to one another. Specifically, it has been found by other work conducted in the Wiggins Research Group using deuterium NMR that these molecular motions are due to phenyl ring rotations on both the amine and the epoxide.

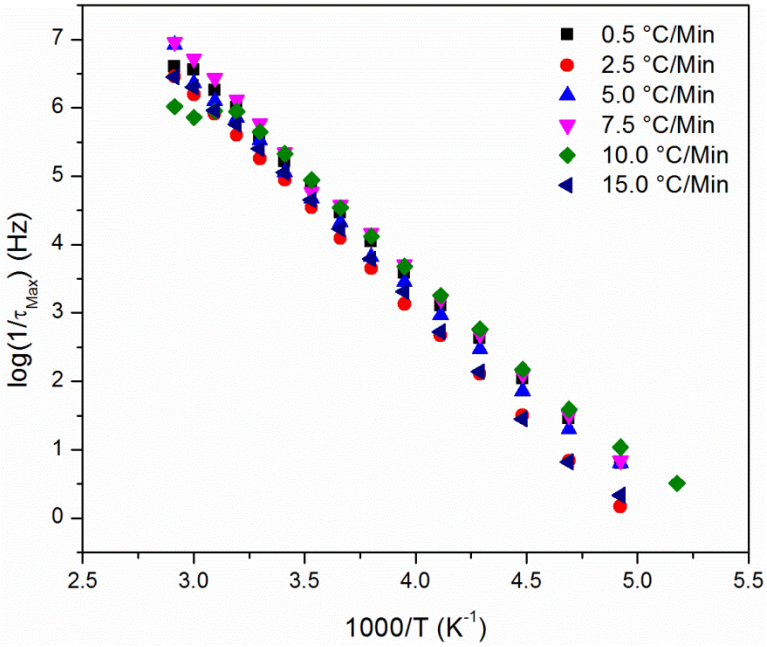

Figure 74. γ relaxation Arrhenius plot for a series of cure heating ramp rates.

Table 9

Calculated activation energies for the γ transition for a series of cure heating ramp rates.

Ramp Rate °C/Min	Ea kJ/mol	Fit R^2 ---
0.5	56.99	0.9988
2.5	60.51	0.9998
5	57.85	0.9961
7.5	58.67	0.9979
10	55.36	0.9977
15	60.93	0.9984

Unlike for the glass transition, for the secondary transitions, the distribution of relaxations cannot be calculated. However, if differences were to be observed in the dielectric storage, loss, or tan δ, inferences could be made as to network differences. These could only be identified at a sufficiently low enough temperature to ensure that the entire relaxation would be observed for all heating ramp rates. To that end, the remainders of the γ relaxation experiments to be discussed here were conducted at -60 °C.

The dielectric storage versus frequency for each of the cure heating ramp rates is shown in Figure 75. In the case of the dielectric storage there is little variation to be observed; however, differences would be clearer in either the loss or tan δ curves. The vertical shift of this plot is due to variations in sample thickness.

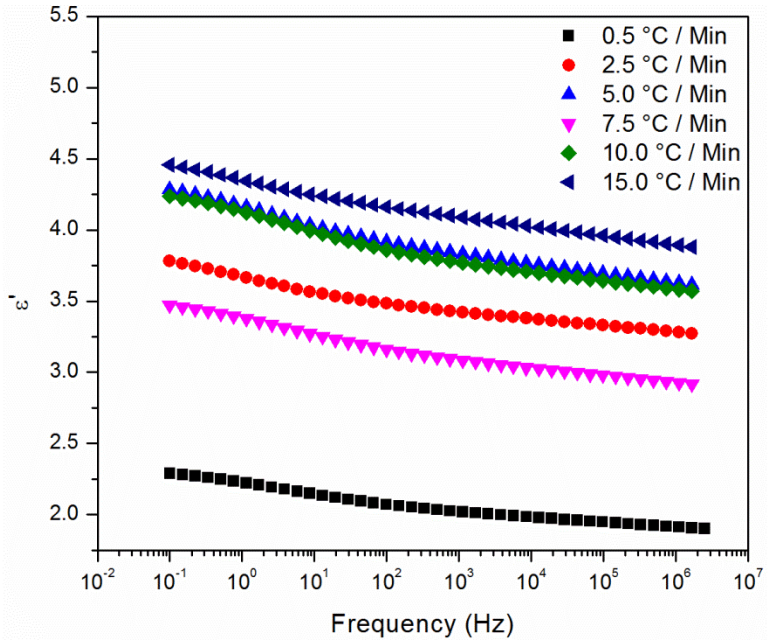

Figure 75. γ relaxation storage at -60 °C for a series of cure heating ramp rates.

While little change is observed in the dielectric storage plots, significant changes can be seen in both the dielectric loss and tan δ curves with respect to cure heating ramp rate. The plot of dielectric loss is3 shown in Figure 76. In this plot, the dashed guide line is to represent the relaxation frequency for the 0.5 °C/min sample; the solid lines are the HN fit lines. There is clearly some deviation from the 0.5 °C/min relaxation time in this plot, especially for the 2.5, 5.0, and 15.0 °C/min samples. The tan δ plot shown in Figure 77 shows a similar trend to the dielectric loss plot. The exact trend cannot be currently explained; however, differences are found for the peak maximum in each cure heating ramp rate. Interestingly, the trend seems to coordinate with that found in the free volume hole size. As the ramp rate increases, the tan δ peak shifts to lower frequency until at approximately 10.0 °C/min where the frequency seems to return to the original. This was the same trend observed in the free volume; thus, the peak shifts could have to do with the molecular architecture or organization of the molecules in space since the motions

themselves must be the same. Despite this claim, at the time of this work, a specific method to test this hypothesis has not been devised.

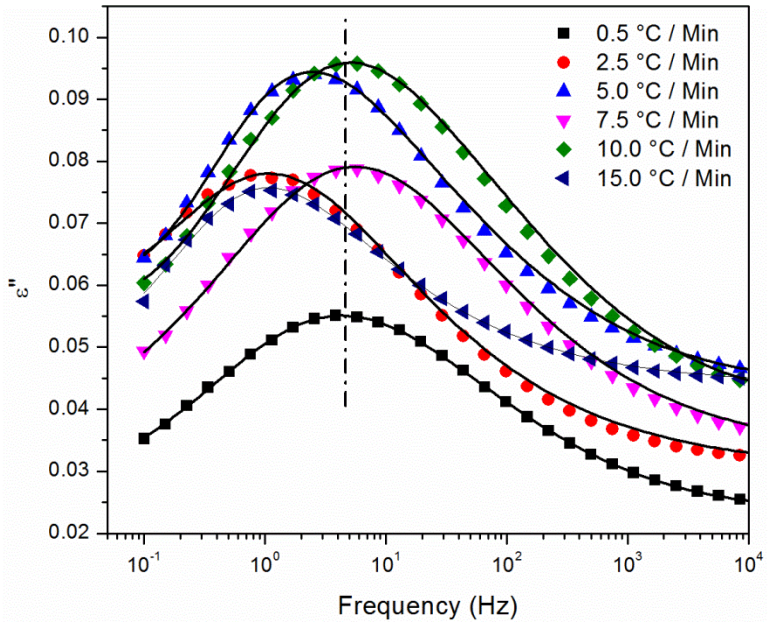

Figure 76. γ relaxation dielectric loss for a series of cure heating ramp rates.

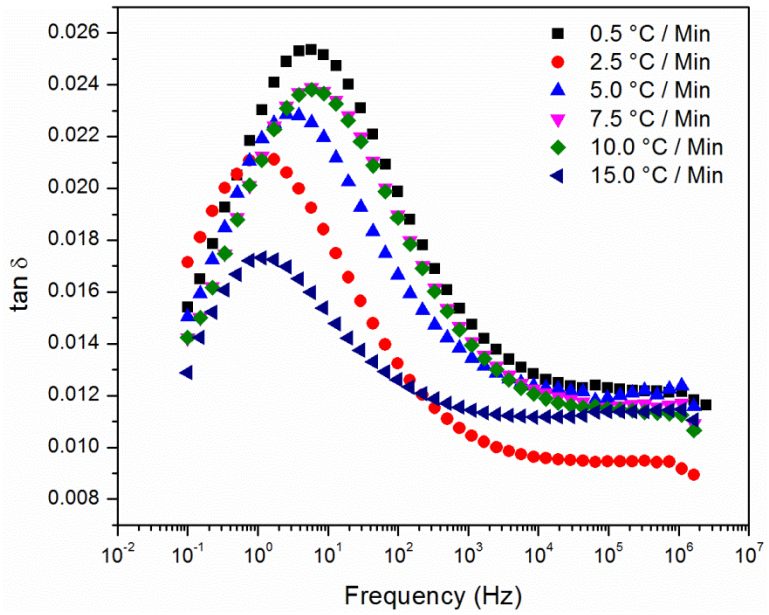

Figure 77. γ relaxation dielectric tan delta for a series of cure heating ramp rates.

While this transition is slightly dependent on cure heating ramp rate, it is unsurprising that when attempting to observe a cure rate dependence correlation with mechanical properties it cannot be found. With the results for the γ relaxation, no or very little difference in mechanical properties would be expected to be found unless the sensitivity of the test was on par with that of DES. This result could also explain why there has been much debate in the field of thermoset materials as to if there is or is not a cure rate dependence of these materials and why it is so chemistry specific. If chemistry were to be found where the cure heating ramp rate would alter the transitions that occur during the operating/testing window, then a difference would be observed. If this were not the case, then some subtle differences, such as free volume, might be observed even when large scale differences were not. This would be especially relevant for epoxy/amine polymers that exhibit a glass transition temperature at or below room temperature.

in situ DES

In addition to the more traditional dielectric analysis discussed above, *in situ* dielectric analysis was also conducted. While this is a newer method of analysis, it can provide considerable information to support both the previous dielectric work, as well as other analysis techniques discussed in the previous chapter. As mentioned previously in this dissertation, *in situ* DES tracks the ion mobility, which is directly related to the ion viscosity of the matrix during its cure. Essentially, ion viscosity is a measure of the mobility of ionic impurities present in the system (and is related to the rheological viscosity of the matrix). In the near future, this technique will realize wide use in the composites field due to its versatility and the ability to be incorporated into a wide variety of material structures and chemistries.

The plot of log ion viscosity versus cure time for a series of cure heating ramp rates is shown in both Figure 78 and Figure 79. Figure 79 is formatted to allow for easier viewing of the faster heating ramp rates. For all systems, the initial decrease in ion viscosity is related to the increasing temperature of the heating ramp. These plots are used to determine the vitrification time of the polymer matrix as well as a relative view of the kinetics of the polymerization reaction. Figure 78 highlights the vitrification time for the various cure heating ramp rates, and aside from the slowest ramp rate of 1 °C/min, is identical for each of the systems. The kinetic component of the analysis is related to the linear region of the second increase in ion viscosity. In all cases the kinetics of the reaction appear to be similar, which is consistent with the DSC iso-conversional analysis discussed in Chapter V.

Despite differences in vitrification time and kinetics, there are subtle differences in these polymers that is detected with *in situ* DES. The first interesting piece is the initial increase and then decrease of ion viscosity in these polymers. The spectra are shown at 1 Hz, which is related to the longer range molecular motion in these polymers and are a manifestation of the linear growth of the 33DDS polymer before the majority of the crosslinking reaction occurs. In the case of the slowest ramp rate, this is a fairly well-defined process that takes a considerable amount of time; while for the faster ramp rates this process occurs fairly quickly. This difference in time indicates that the reaction is happening quicker, which leads to a more rapid formation of crosslinking that makes the molecular size scale of the matrix polymers unique (as seen in PALS data and the distribution of relaxation times).

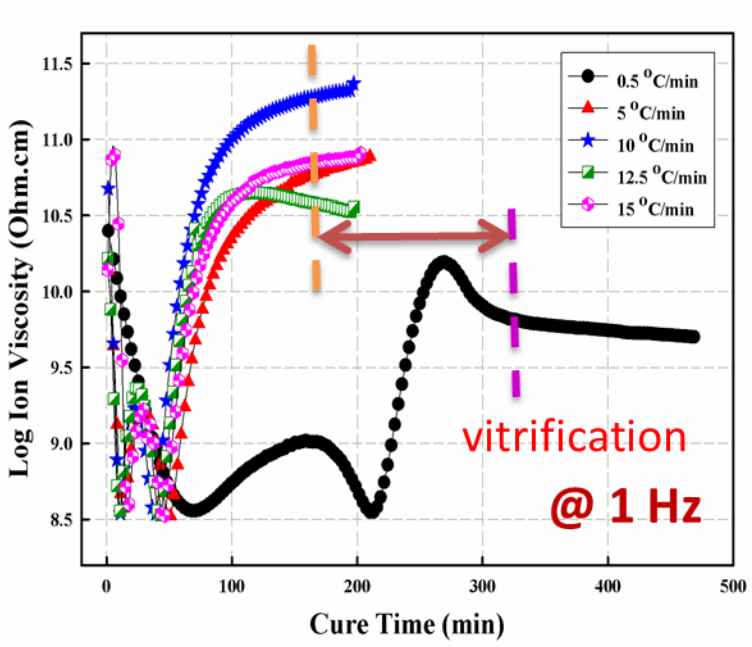

Figure 78. in situ dielectric analysis for a series of cure heating ramp rates.

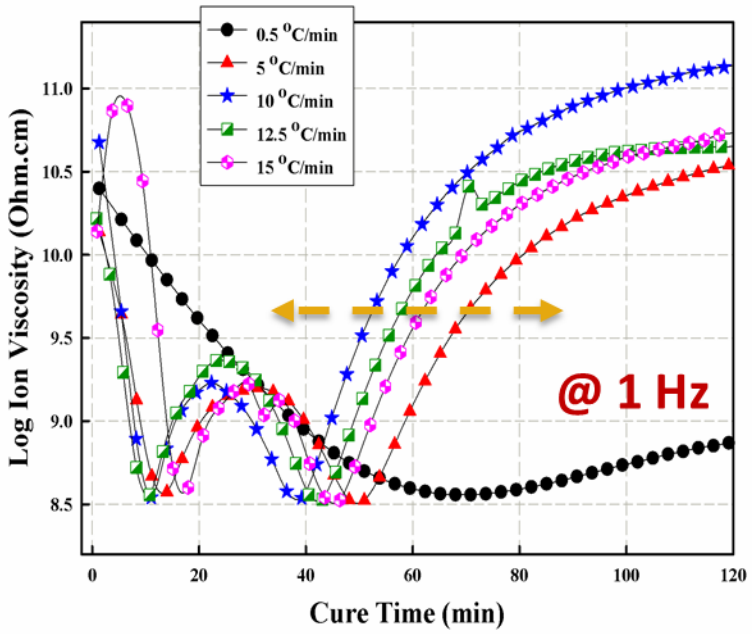

Figure 79. in situ dielectric analysis for a series of cure heating ramp rates, highlighting the faster ramp rates.

Summary

In conclusion of this chapter, dielectric spectroscopy is a power tool to analyze the molecular level structure for thermoset polymer networks. It was used to show a unique difference in the distribution of relaxation times for the glass transition that solidifies cure rate dependence for this specific thermoset polymer. Furthermore, differences in the γ transition were also shown. However, these were not as clear as for the glass transition. DES also found that there were several peaks for the glass transition, only one of which can be currently identified as a MWS polarization event. The other two peaks could not be identified at this time. However, that two peaks were present in the first place, one which closely follows the standard VFW trend for glass transition and one that shows an Arrhenius dependence, is quite interesting and bears further analysis.

CHAPTER VII

THERMAL EVALUATION OF MULTIFUNCTIONAL EPOXIDE POLYMER FORMATION DEPENDENCE ON CURE HEATING RAMP RATE

Objective

The purpose of this chapter is to discuss a preliminary evaluation of the cure rate dependence for an epoxy/amine thermoset polymer network comprised of either TGDDM/33DDS or TGDDM/44DDS. These specific monomers were selected for several reasons but first and foremost to elucidate if the previously exhibited cure rate dependence is unique to that chemistry or if all epoxy/amine thermoset polymers show similar behavior. Additionally, TGDDM was chosen as the epoxide component of the polymer because previous work from this research group has demonstrated differences in free volume, fluid uptake, and mechanical performance over di-functional epoxide monomers.[5,11] It has also previously been established that no matter the cure profile, complete conversion of epoxide and amine cannot be achieved. This is due to the high cross-link density and the early onset of vitrification of the network polymer. It is proposed that differing cure heating ramp rates may alter the final conversion of the polymer and magnify any dependence on the cure heating ramp rate.

As with the previous chemistry explored in Chapters V and VI, the initial evaluation of cure heating ramp rate dependence for both TGDDM/33DDS and TGDDM/44DDS will be done thermally using DSC. Unlike the previous experiments, however, an emphasis has been placed on conversion of the network and any dependence on cure heating ramp rate. Finally, both isomers of amine monomer (33 and 44DDS) will be studied to determine any influence of isomer reactivity or rotational degrees of freedom on conversion and cure rate dependence.

Results and Discussion

Uncured Heat of Reaction

Determination of conversion via DSC is a relative method, not an absolute one; therefore to use DSC to determine conversion, an initial baseline for the exotherm intensity must be chosen. Traditionally, the accepted method for the determination of cure conversion has been to determine the exotherm intensity at a heating ramp rate of 10 °C/min. However, the intensity of the exotherm is directly related to the cure heating ramp rate of the polymer sample. To eliminate this problem, the exotherm intensity of an uncured polymer sample at a series of cure heating ramp rates from 1–65 °C/min was determined. This value was called ΔH_{uc}, or the uncured heat of reaction. The values for ΔH_{uc} for the TGDDM/33DDS polymer and their dependence on cure heating ramp rate are shown in Figure 80. The values for the TGDDM/44DDS polymer are shown in Figure 81. In both cases, a strong exponential dependence in observed between the heat of reaction and the cure heating ramp rate with the following equations:

$$[33DDS]: \quad \Delta H_{uc} = -97.16 * \exp\left(-\frac{\beta}{20.50}\right) + 549.90$$

$$[44DDS]: \quad \Delta H_{uc} = -291.09 * \exp\left(-\frac{\beta}{9.94}\right) + 529.97$$

where β is the cure heating ramp rate in °C/min. By taking the limit of both these equations as β approaches infinity, the uncured heat of reaction of an infinitely fast ramp rate can be approximated. Since the uncured heat of reaction increases as the heating ramp rate increases, the limit value should be the maximum possible eliminating any complications for the determination of cure conversion.

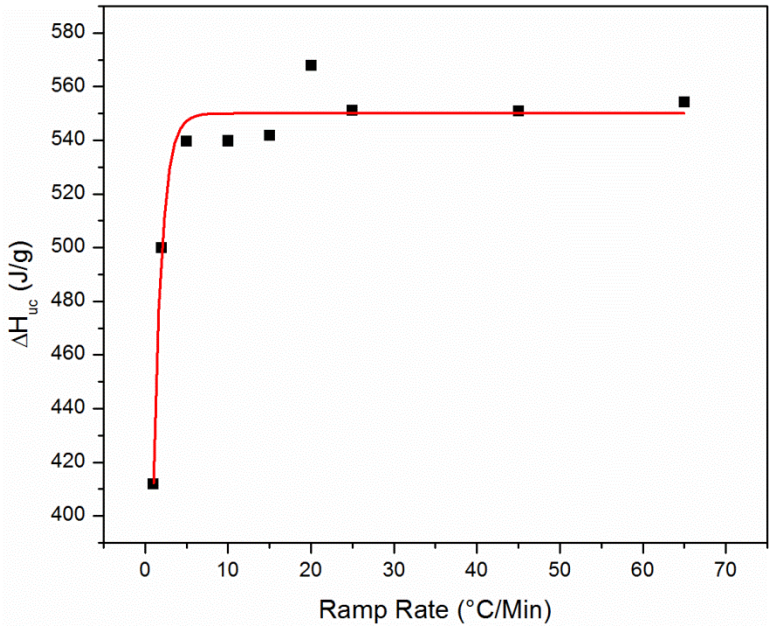

Figure 80. ΔH_{uc} for 33DDS/TGDDM for a series of cure heating ramp rates. $R^2 = 0.9844$, exponential fit.

It is also important to note that despite the concentrations of chemical equivalent amine are present in each polymer; the 33DDS matrix polymer has a larger uncured heat of reaction, suggesting that a higher conversion is possible for the 33DDS polymer than the 44DDS analogue. While it is still unclear as to why the 33DDS system would reach a higher conversion, it is suspected that either the isomerization of the DDS causes a delay in vitrification, allowing more conversion, or by releasing more thermal energy earlier on in the reaction (seen when comparing the increase in ΔH_{uc} for both figures) causes more reaction to be achieved before vitrification.

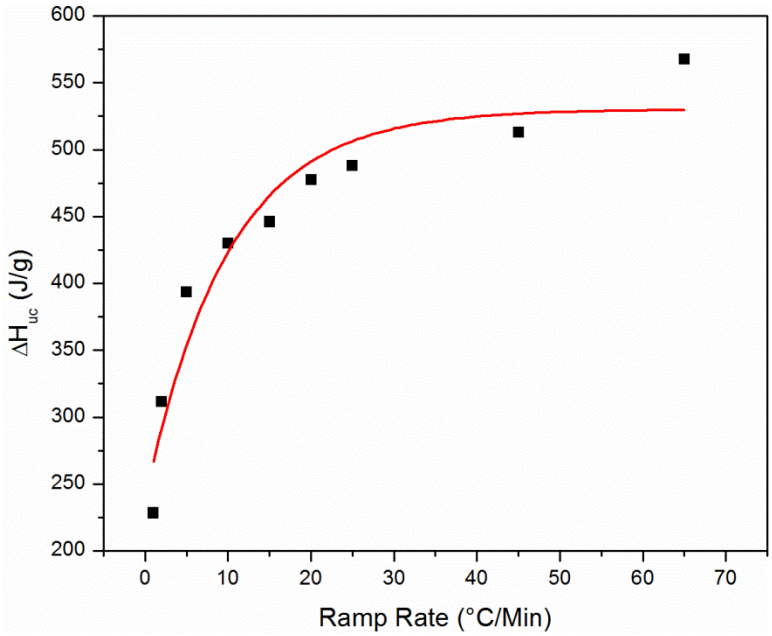

Figure 81. ΔH_{uc} for 44DDS/TGDDM for a series of cure heating ramp rates. $R^2 = 0.9086$, exponential fit.

Thermal Profile

In addition to the determination of the uncured heat of reaction, the initial heating ramp rate DSC experiments can also be used to determine other factors of the polymer thermal profile such as onset of reaction, peak exotherm temperature, and reaction completion time. The importance of these parameters has already been discussed in Chapter V, however, it is essential to compare these parameters for TGDDM/33DDS and TGDDM/44DDS to DGEBF/33DDS to attempt to distinguish a chemistry dependence on the cure heating ramp rate.

The plots for onset of reaction versus ramp rate for TGDDM/33DDS and TGDDM/44DDS are shown in Figure 82 and Figure 83, respectively. These figures both show a different trend than previously seen for DGEBF/33DDS (see Chapter V). In the case of the DGEBF chemistry, an upper limit to the onset reaction temperature was observed at approximately 10 °C/min; however, in the case of both TGDDM network

polymers, no such maxima is observed over the temperature range. The data does suggest that in both cases, at 65 °C/min the upper limit is being established. While unexpected, this effect is most likely related to the reactivity of the monomers. Since the profiles for 33DDS and 44DDS are similar, the epoxide monomer specifically must dominate the onset profile; however, the specific cause is not well understood at this time.

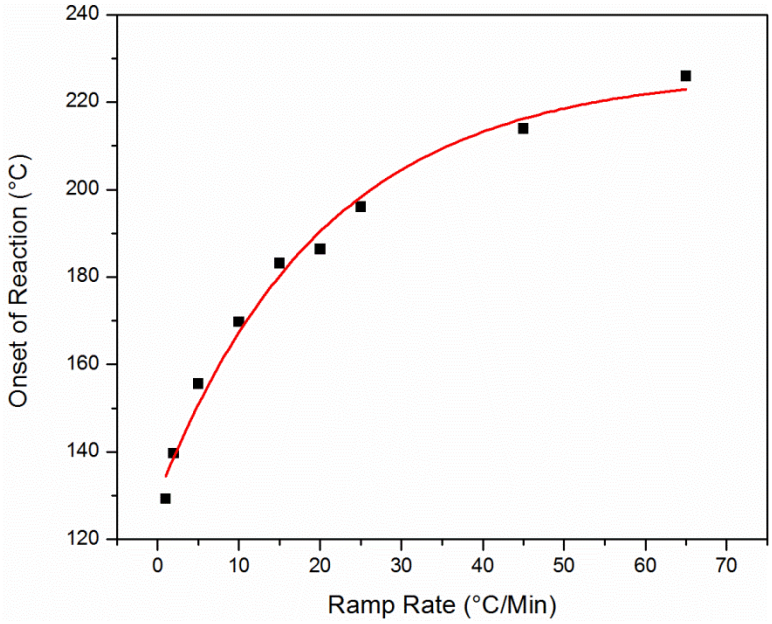

Figure 82. Onset of reaction for 33DDS/TGDDM as a function of cure heating ramp rate. R^2 = 0.9736, exponential fit.

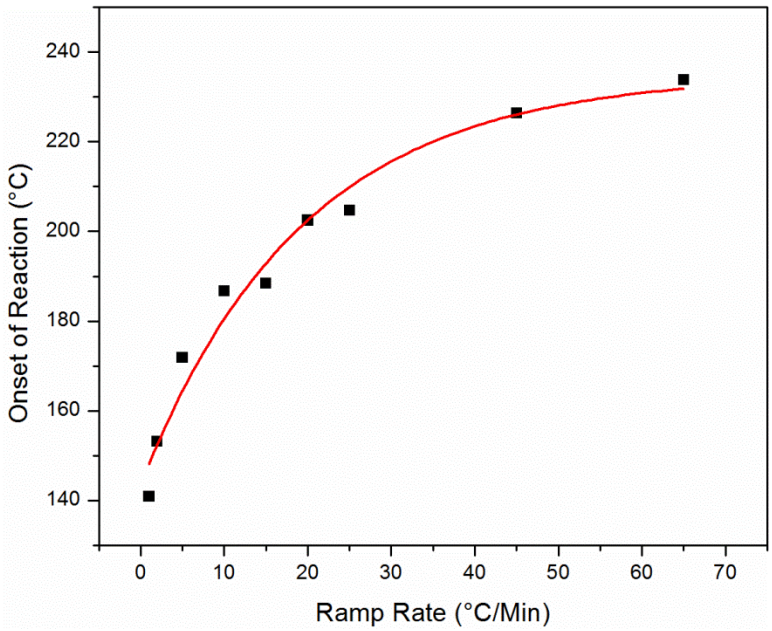

Figure 83. Onset of reaction for 44DDS/TGDDM as a function of cure heating ramp rate. R^2 = 0.9657, exponential fit.

The peak exotherm temperatures for these polymers were also compared to the DGEBF baseline system. Shown in Figure 84 and Figure 85 are the plots of peak exotherm temperature versus the cure heating ramp rate for TGDDM/33DDS and TGDDM/44DDS polymers, in that order. Both plots are extremely similar, supporting the belief that for these polymers, it is the epoxide component driving the thermal profile of the polymers. But it is important to note that while these curves are similar, they provide an important piece of the picture when determining how to process thermoset polymers very quickly. While it may be that the very fast ramp rates are advantageous from a processing point of view, that may not be the case when considering the temperatures to which these polymers would have to be heated, in order to achieve similar conversions (assuming a non-isothermal process).

This data is also useful when considering the degradation temperature of these polymers. While this was not specifically studied in this work, it is known that

epoxy/amine based polymers tend to degrade at temperatures in excess of 350 °C, if not sooner. These peak exotherm temperatures are pushing dangerously close to the degradation range of epoxy/amine polymers, and as a result of their cure may begin to undergo degradation. However, to reach any specific conclusions on this, additional work is required.

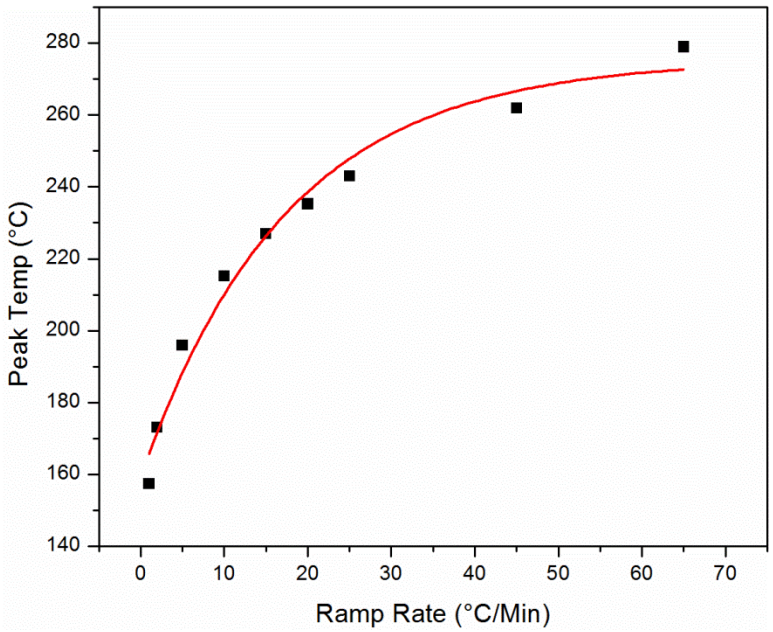

Figure 84. Peak exotherm temperature as a function of cure heating ramp rate for 33DDS/TGDDM. R^2 = 0.9598, exponential fit.

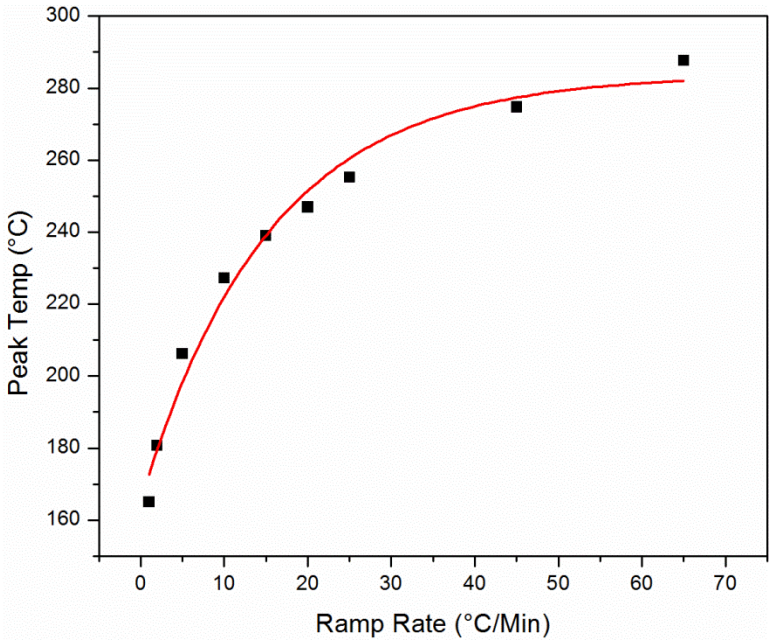

Figure 85. Peak exotherm temperature as a function of cure heating ramp rate for 44DDS/TGDDM. R^2 = 0.9762, exponential fit.

From a processing point of view, completion time is perhaps the most important factor of the polymer's thermal characterization that was conducted. This is also true from a network architecture perspective. When the DGEBF/33DDS matrix polymer was studied, it was found that, below the exponential limit of completion time, the network grew in a more linear fashion first, then cross-linked. Above the heating ramp rate associated with the critical completion time (10 °C/min for DGEBF/33DDS) the network was found to grow differently. Beyond that, it was found that heating above this ramp rate caused a further change in network formation. Thus, in order to compare the TGDDM based polymers to the previously studied system it is important to determine if there is a point where the completion time becomes independent of cure heating ramp rate.

A plot of completion time versus cure heating ramp rate for the TGDDM/33DDS polymer is shown in Figure 86. A similar plot for TGDDM/44DDS is shown in Figure

87. Both matrix polymers exhibit a similar trend to the DGEBF/33DDS polymers, with only a variation in the cure heating ramp rate for which completion time becomes independent. For the TGDDM/33DDS polymer, the cure heating ramp rate that leads to independence is higher, around 20 °C/min, and for the 44DDS analogue, around 10-15 °C/min. This is interesting when conducting a thought experiment to compare the TGDDM/33DDS matrix polymer to the DGEBF/33DDS matrix polymer. In both cases, at some point, enough thermal energy will be placed into the polymer matrix to cause a change in network growth from a more linear to a more globular type growth. From the research conducted on the DGEBF based polymer, which would appear to be around 10 °C/min. The reasonable question then is to ask is how would this affect network architecture for this polymer system when the cutoff ramp rate and ramp rate of equal amine reactivity are not the same. While more work is necessary to reach a conclusion, it is proposed that this difference would lead to one of two possible outcomes: either there is no difference between the TGDDM and DGEBF systems, or this difference leads to a change in network formation. It is the opinion of the author that this deviation is too subtle to drastically alter the network formation and would not be noticed. But again, more work is necessary to solidify this hypothesis, specifically DES and NIR kinetics analyses.

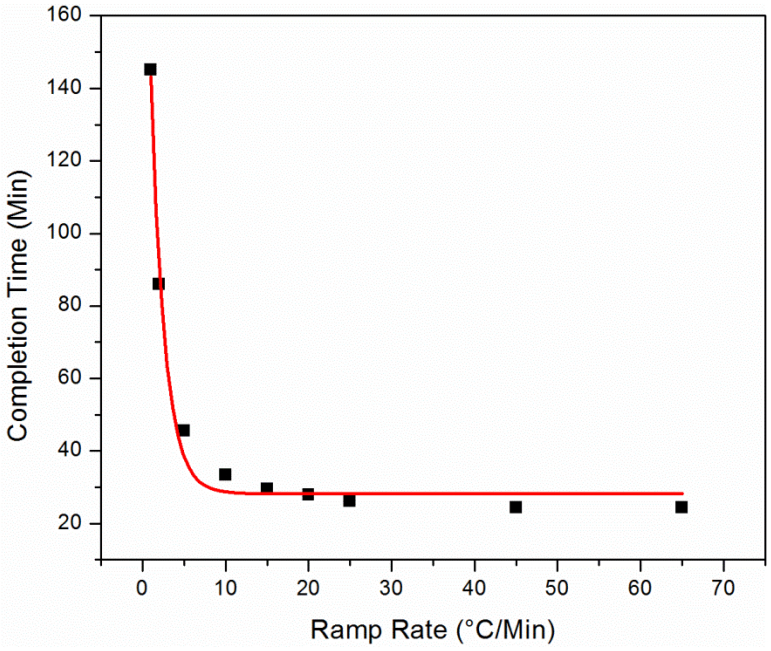

Figure 86. Completion time vs cure heating ramp rate for 33DDS/TGDDM. R^2 = 0.9357, exponential fit.

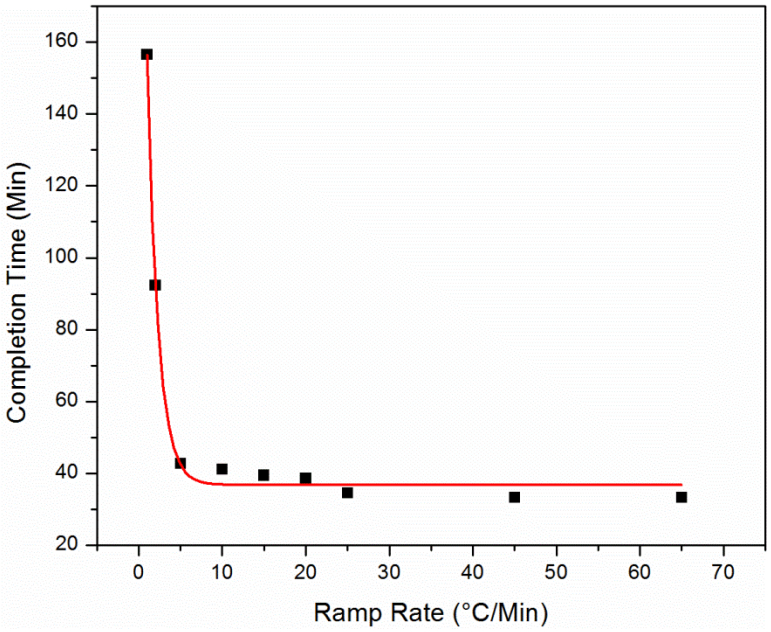

Figure 87. Completion time vs cure heating ramp rate for 44DDS/TGDDM. R^2 = 0.9945, exponential fit.

Iso-conversional Analysis

With the peak exotherm temperature data previously discussed, it is possible to perform a kinetics analysis that is commonly shown for thermoset polymers to determine the activation energy and the progression of cure. While the method has been previously discussed (Chapter II) and employed (Chapter V), to validate the DSC experimental data and for consistency, the analysis will also be employed here.

Using both the FWO and KAS approximations for the Arrhenius equation, plots versus reciprocal temperature have been generated, resulting in a linear correlation for both the 33DDS and 44DDS matrix polymers. FWO and KAS plots for TGDDM/33DDS are shown in Figure 88, and similar plots for TGDDM/44DDS are shown in Figure 89. Strong linear agreements, with a square residual of greater than 0.98, were found for both polymers resulting in a high degree of confidence that the DSC experiments were valid for the remainder of the data.

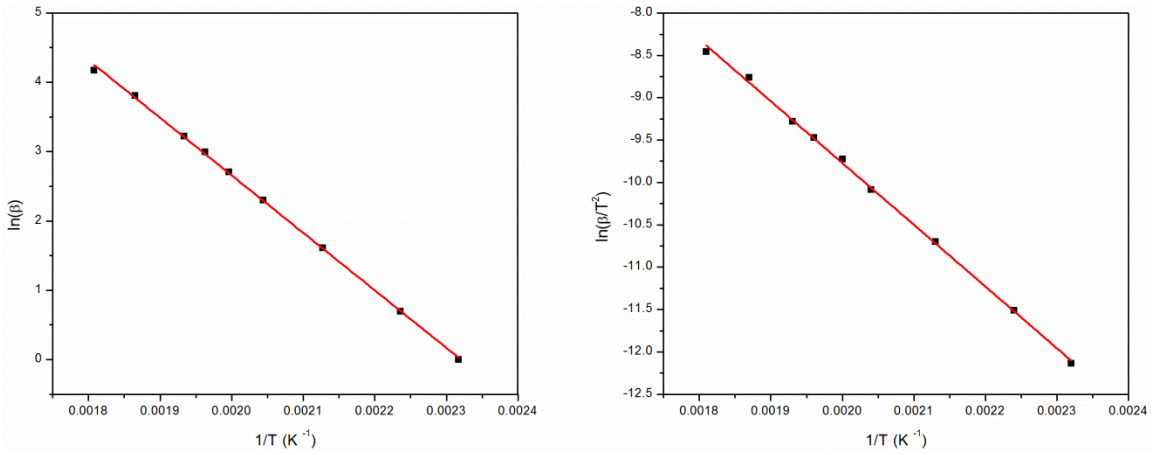

Figure 88. FWO (left) and KAS (right) plots for 33DDS/TGDDM. R^2 = 0.9988 and 0.9993, respectively, linear fit.

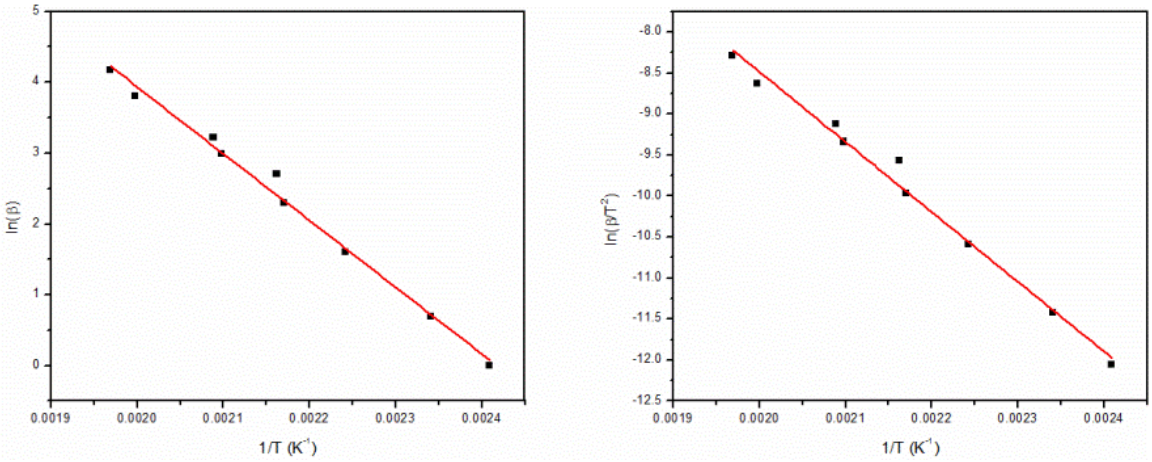

Figure 89. FWO (left) and KAS (right) plots for 44DDS/TGDDM. R^2 = 0.9897 and 0.9869, respectively, linear fit.

The calculated activation energies shown in Table 10 are consistent with previous work. It is interesting to note that despite the slightly larger activation energy for the 44DDS polymer matrix, the completion time becomes independent of cure heating ramp rate at a slightly lower temperature than the 33DDS matrix polymer. This is consistent, however, with the lower uncured heat of reaction, ΔH_{uc}, for the 44DDS polymer and is most likely an effect of electrostatics of the 44DDS molecule. Since the alpha carbon to the amine is slightly electronegative for the 44DDS monomer, more electron density remains on the amine. This stability results in a more labile isomer for the 44 than for the 33DDS, resulting in a higher activation energy. Furthermore, with differing reactivities between the primary and secondary amine on the 33DDS, more facile reaction of the primary amine is expected, resulting in lower activation energy (due to the opposite electrostatic effect of the 44DDS monomer). At the same time, when the secondary amine reacts, more energy is required to overcome the difference in reactivity, resulting in a stronger dependence on the applied thermal energy, or the cure heating ramp rate.

Table 10

Apparent activation energies for two amines cured with TGDDM epoxide.

Amine	Ea (FWO) kJ/mol	Ea (KAS) kJ/mol
33DDS	65.56	60.89
44DDS	74.59	70.84

When the DSC exotherm intensity data is integrated over time, relative conversion can be determined according to the iso-conversional analysis method. Similar to the activation energy discussion, this method has already been introduced; however, a more complete understanding of the reaction of the matrix polymer can be had with its inclusion.

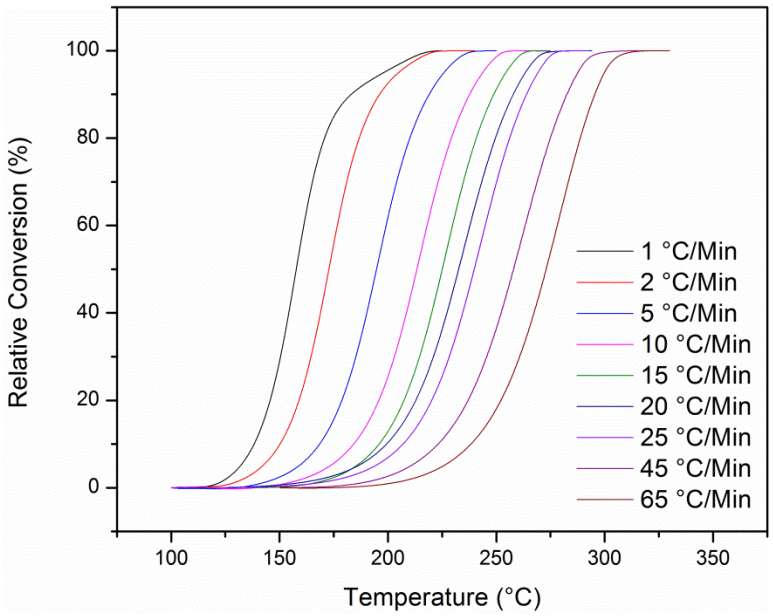

Figure 90. Iso-conversional analysis of 33DDS/TGDDM.

Figure 90 and Figure 91 show the iso-conversional analysis for the TGDDM/33DDS and TGDDM/44DDS polymers, respectively. The trend of increasing onset of reaction and reaction completion is illustrated well with both of these figures,

and the plots are similar to the DGEBF/33DDS matrix polymer. In the case of the 33DDS polymer, there appears to be no general change in the shape of the iso-conversion curves with the exception of the 1 °C/min ramp rate. The difference in line shape could be related to a change in mechanism of reaction or could be an artifact of using a non-modulated DSC; however, no conclusion can be reached at this time. For the 44DDS matrix polymer, there does not appear to be major differences among the various heating ramp rates, suggesting a similar mechanism across the spectra of heating ramp rates.

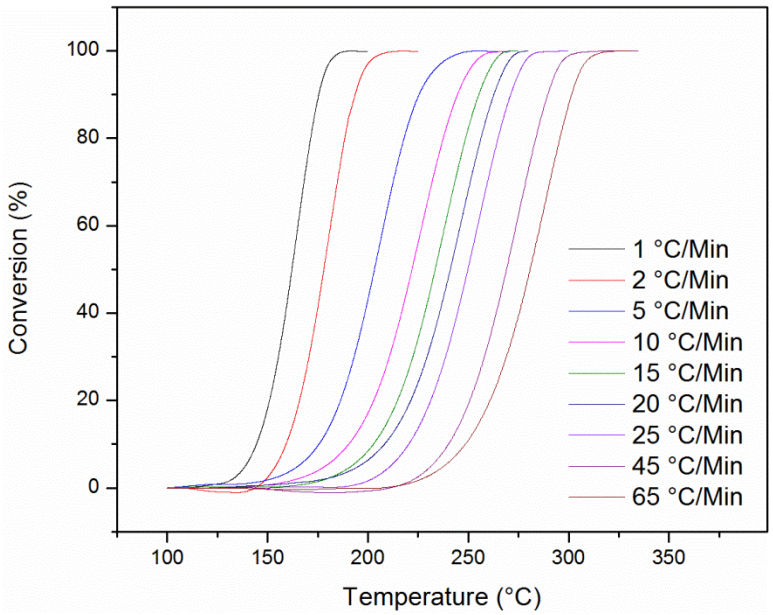

Figure 91. Iso-conversional analysis of 44DDS/TGDDM.

Cure Rate Heat of Reaction

Now that the other thermal characteristics and their relation to the cure heating ramp rate are understood, the final two areas to explore are the exotherm intensity of cure and the resulting cure conversion of the reaction. The first to be discussed will be the exotherm intensity during the cure.

The exotherm intensity during the cure also called the cured heat of reaction, ΔH_c for short. It is characterized as the integral under an exothermic event in a DSC trace for the residual cure. This value is determined by first heating the sample at a specified cure ramp rate to 180 °C, isothermal hold if necessary, then quenching the reaction and heating again at a standard ramp rate to 300 °C. The second peak is then integrated and called the cured heat of reaction. This process allows for the study of the residual cure, or additional cure, during the second heating cycle and can then be used to calculate the relative degree of conversion. Specifically, the cured heat of reaction was explored for just the heating ramp rate, or from 35-180 °C, and then also for 30 and 60 min isotherms after the heating ramp. Isothermal holds above 60 minutes were not necessary because the reaction had been completed in all cases (see Figure 86 and Figure 87).

The cured heat of reaction for the heating ramp only versus cure heating ramp rate for TGDDM/33DDS is shown in Figure 92. As expected, the faster cure heating ramp rates reach a much higher exotherm intensity for the cure, but it is worthy of note that for these experiments, time is not constant. In the case of the 65 °C/min ramp rate, little more than 2 min pass between the start and end of the experiment versus nearly 145 minutes for the 1 °C/min ramp rate. This time difference leads to a much larger concentration of exotherm intensity in the polymer sample. It will be discussed later in this chapter, but this could lead to variations in the amount of cure achieved or degradation of the polymer sample.

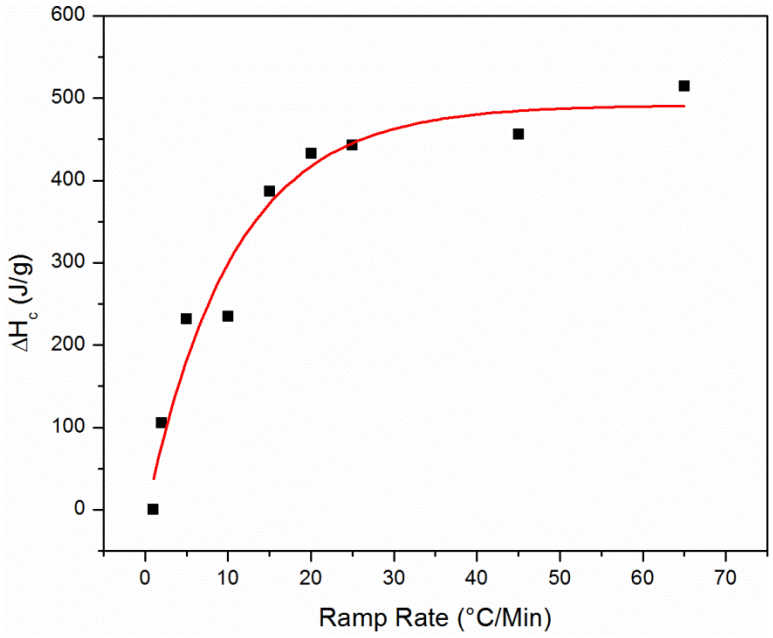

Figure 92 .ΔH_c after 0 min of cure at 180 °C for 33DDS/TGDDM. R^2 = 0.9433, exponential fit.

After the initial cured heat of reaction for only the ramp rate was studied, isothermal holds of both 30 and 60 min were also studied. Their cured heat of reaction plots are shown in Figure 93 and Figure 94, respectively. Similar to the 0 min hold for the 1 °C/min ramp rate, the 30 and 60 min holds show very little exotherm energy, meaning that nearly all the reaction has occurred during the heating ramp. Additionally, there is an exponential increase in the exotherm intensity versus ramp rate for these polymers, with increasing ramp rate. This suggests that, as the ramp rate increases, less reaction occurs, even after an isotherm of 30 or 60 min. This supports the original hypothesis that the amount of reaction will be dependent on the cure heating ramp rate but is the opposite trend as expected. Originally, an increase in the amount of reaction with increasing ramp rate was anticipated, but this is not the case for 33DDS/TGDDM. Therefore, the premise that applying more thermal energy more quickly will allow more reaction to occur before

vitrification is incorrect. In fact, it appears that the opposite is true; vitrification occurs so quickly that less conversion is realized during the cure.

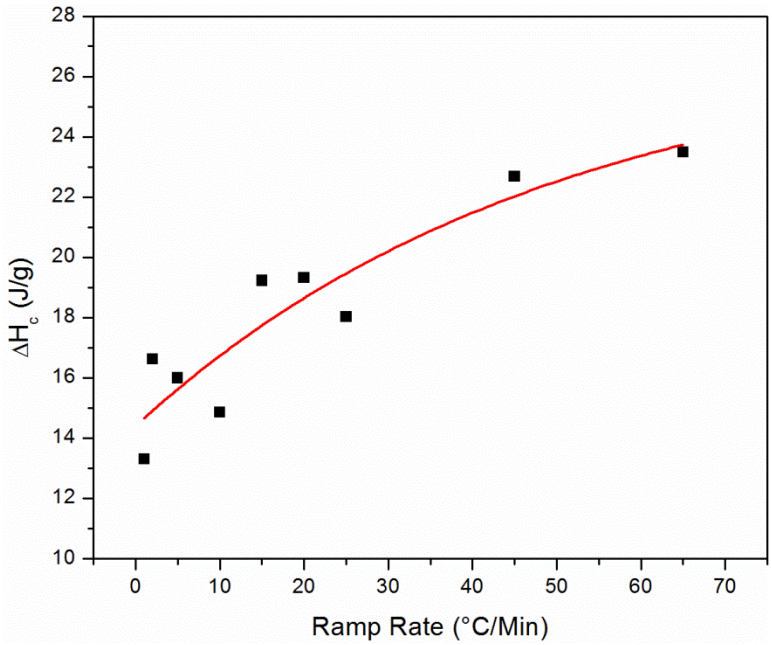

Figure 93. ΔHc after 30 min of cure at 180 °C for 33DDS/TGDDM. R^2 = 0.8032, exponential fit.

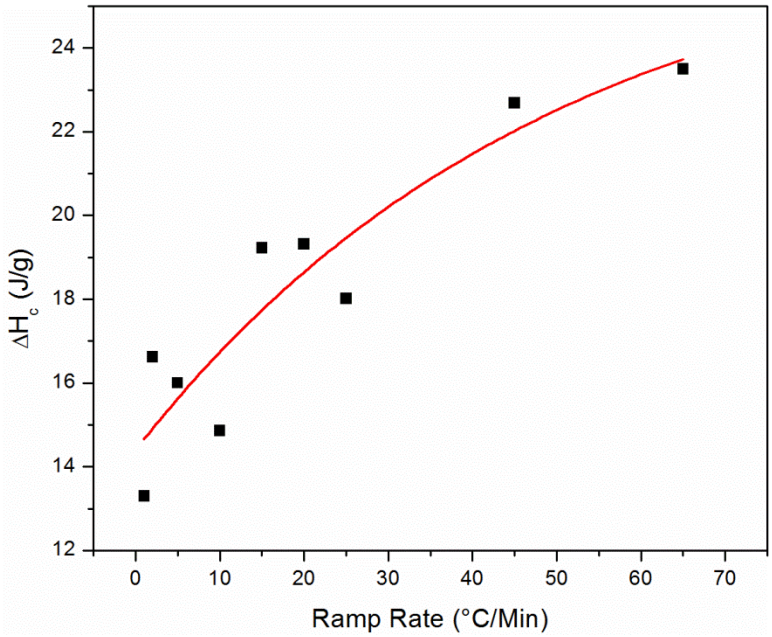

Figure 94. ΔHc after 60 min of cure at 180 °C for 33DDS/TGDDM. R^2 = 0.8024, exponential fit.

Experiments identical to those just discussed for TGDDM/33DDS were also performed for TGDDM/44DDS. Some differences and similarities between the two chemistries have already been discussed, and in some regard, this study is no different. The zero minute hold for the cured heat of reaction of TGDDM/44DDS is shown below in Figure 95. The trend observed for this hold is similar to the 33DDS matrix polymer in that a majority of the cure for the very slow ramp rates occur during the cure, and as the ramp rate is increased, the amount of cure during the heating ramp is reduced.

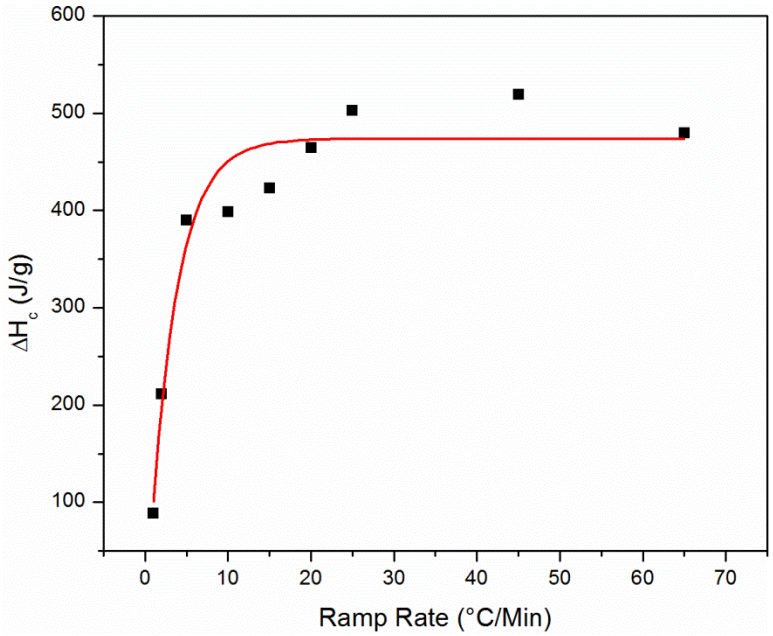

Figure 95. ΔHc after 0 min of cure at 180 °C for 44DDS/TGDDM. R^2 = 0.9299, exponential fit.

Despite their similarities, the major differences between 33DDS and 44DDS polymers are observed in the hold times. Figure 96 shows the 30 min hold and resulting cured heat of reaction dependence on cure heating ramp rate. Initially the trend is the same as the 33DDS analogue; however, the intensity of the exothermic events is much higher, more than double in some cases. This suggests that even less cure is realized during the heating ramp and exotherm than the 33DDS and is most likely related to the differences in activation energy. Finally, for the 30 min hold, the fastest ramp rate of 65 °C/min is also unique. The residual exotherm intensity is much lower and does not fit the trend of the previous samples. The difference is due to thermal degradation, the polymer sample at a ramp rate of 65 °C/min was charred. Thus while the data for this ramp rate should not be used to determine a trend, it was included for completeness.

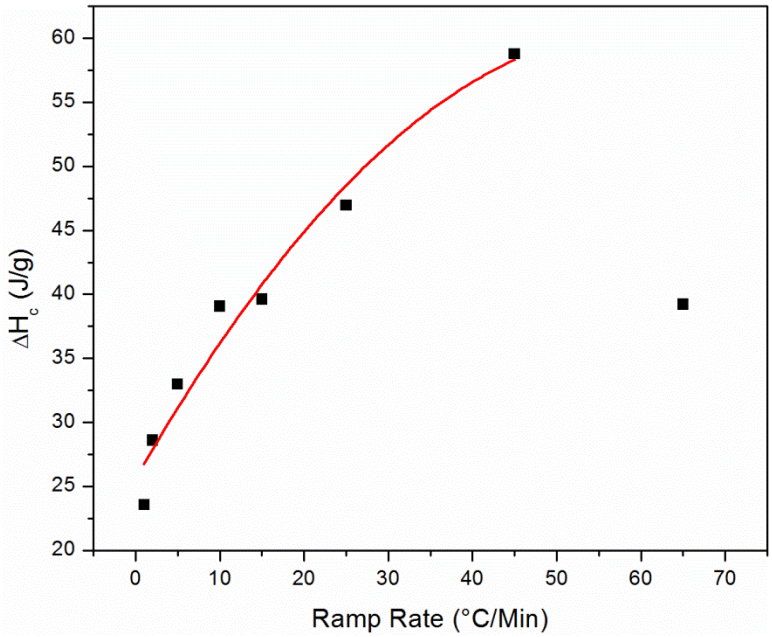

Figure 96. ΔHc after 30 minutes of cure at 180 °C for 44DDS/TGDDM. R^2 = 0.9526, exponential fit.

The cured heat of reaction data for the 60 min polymer sample is shown in Figure 97. Again, this hold shows differences between the 33 and 44DDS based polymers. While no trend can be identified, this fact on its own is important because it shows that after 60 min at temperature, the polymer samples cannot be made to reach a higher conversion. In fact, all polymer samples appear to have reached a similar conversion. As with the 30 min hold, the sample at a ramp rate of 65 °C/min for the 60 min hold was also charred, it is only a coincidence that the data point appears to fall in line with the others.

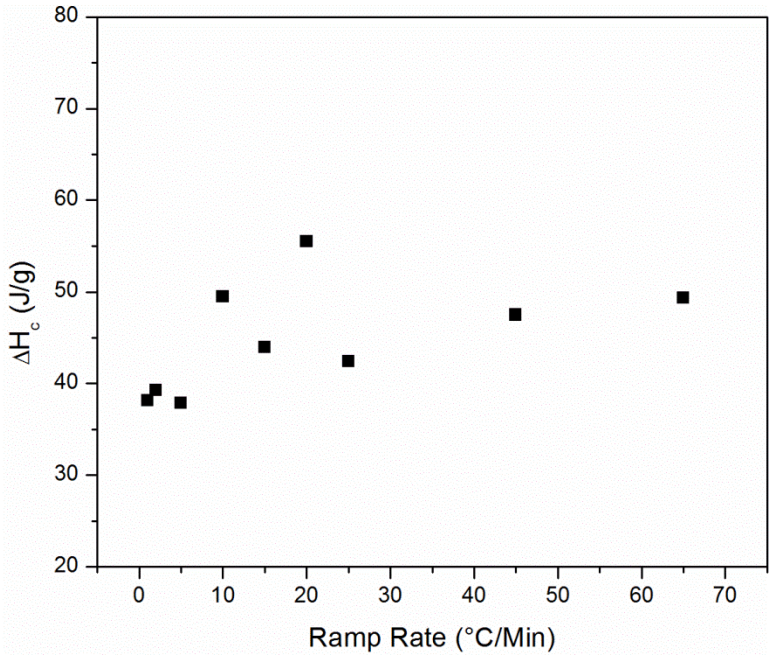

Figure 97. ΔHc after 60 minutes of cure at 180 °C for 44DDS/TGDDM.

Degree of Conversion

The final part of the thermal analysis of the cure rate dependence of multifunctional epoxide based thermoset networks is cure conversion. The calculation for cure conversion is based on both the uncured and cured heats of reaction and can be calculated for just the heating ramp and for isothermal holds of the polymer matrix. The specific equation used for the calculation can be found in Chapter II of this dissertation; however, it is essentially a ratio of the uncured to cured heats of reaction. Because the DSC can only detect when reaction has occurred, it cannot detect any residual un-reacted monomers. As a result of this, the conversion reported is only a relative conversion. Further DES and NIR work still in progress at the time of this writing will provide for an absolute value; however, considerable insight can still be gained from the relative conversion analysis.

The relative conversion for the TGDDM/33DDS matrix for just the heating ramp (no isotherm) is displayed in Figure 98 and shows a trend similar to the uncured heat of reaction. For the slower ramp rates, the maximum amount of relative conversion is achieved only in the ramp, so an isotherm after would be unnecessary. From this information, cycle time for a part could be reduced from a 145 min heating ramp and 180 min isotherm to simply a 145 min isotherm and increasing the ramp rate would not be necessary. However, for all ramp rates faster than 1 °C/min, an isotherm would be necessary.

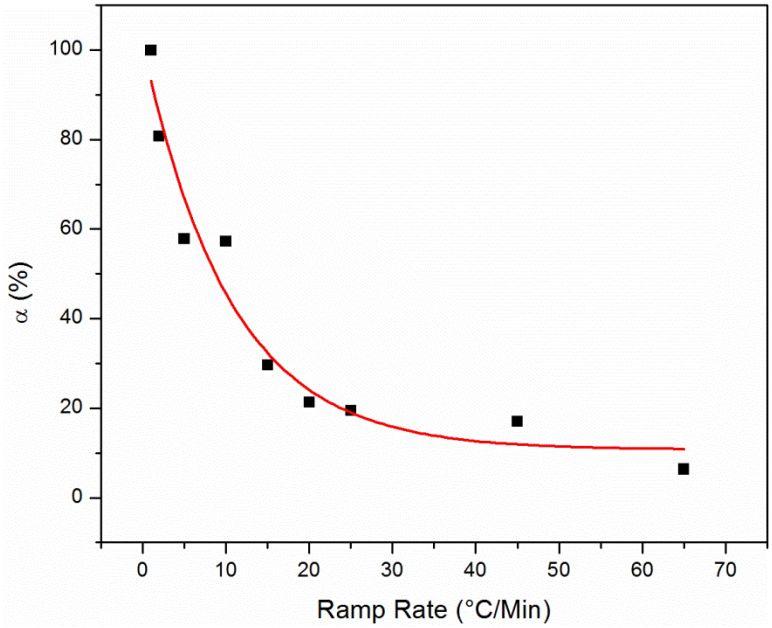

Figure 98. Conversion as measured via DSC for 33DDS/TGDDM after 0 min of cure at 180°C. R^2 = 0.9433, exponential fit.

To maximize the conversion of the TGDDM/33DDS polymers under most circumstances, an isotherm would be necessary. However, the standard isotherm of 180 min is not necessary in the context of Figure 99. Figure 99 shows the conversion after both a 30 and 60 min isotherm at 180 °C. In both cases the polymers reach approximately

the same conversion, with only a few percent differences between them. Similarly to the DGEBF/33DDS system, comparable thermal and mechanical properties should be realized; however, molecular scale properties, such as free volume, may be unique for each cure heating ramp rate.

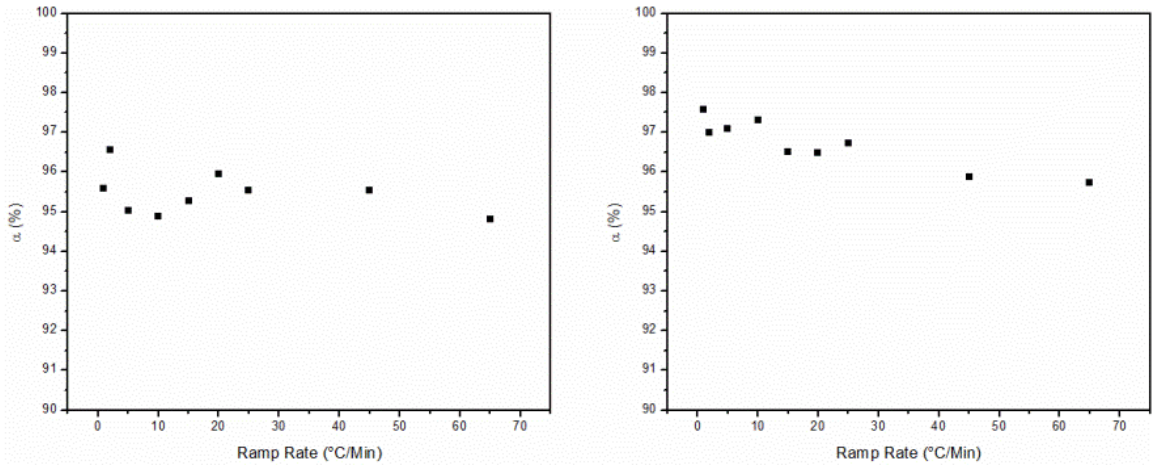

Figure 99. Conversion measured via DSC for 33DDS/TGDDM after 30 (left) and 60 (right) min of cure at 180 °C.

For the TGDDM/44DDS relative conversion shown in Figure 100, the same trend does not hold true as the 33DDS polymer. Conversion of only ~80% is realized for the slowest ramp rate after only the heating ramp. An isotherm would be necessary to maximize the conversion under any of the circumstances studied.

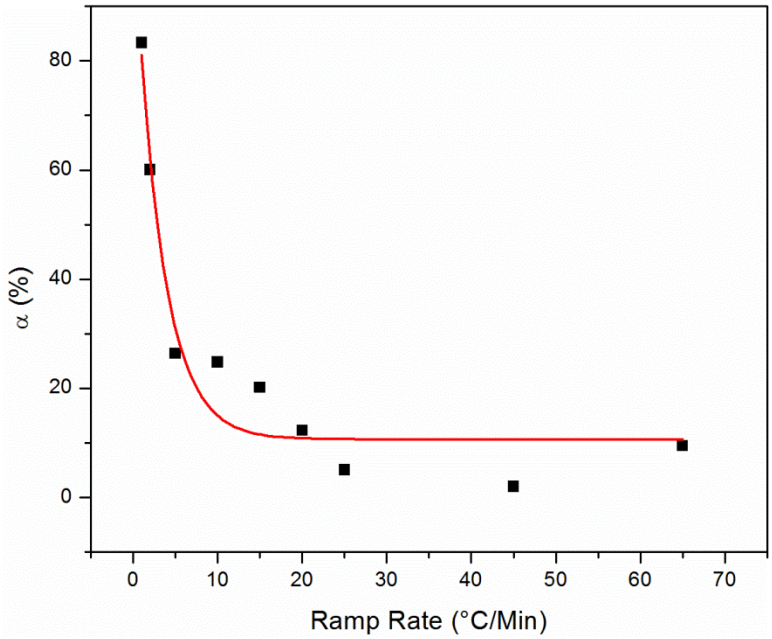

Figure 100. Conversion as measured via DSC for 44DDS/TGDDM after 0 min of cure at 180°C. R^2 = 0.9299, exponential fit.

The conversion for the 30 and 60 min isotherms for the TGDDM/44DDS matrix polymers are shown in Figure 101. In the case of the 44DDS polymer at a 30 min isotherm, each of the ramp rates have a distinct conversion percentage. There is a marked drop in conversion when changing from a 1 to 25 °C/min ramp rate. This would most likely result in differences for thermo-mechanical properties of the polymer matrix. Once the isotherm is extended to 60 min, the differences are minimized. As opposed to a reduction from 95% to 87% conversion for the 30 min isotherm, the 60 min isotherm only drops from about 93% to 90% conversion. It is currently unclear as to why the final conversion is slightly reduced at a 60 min exotherm and could be either experimental error or a minor amount of degradation.

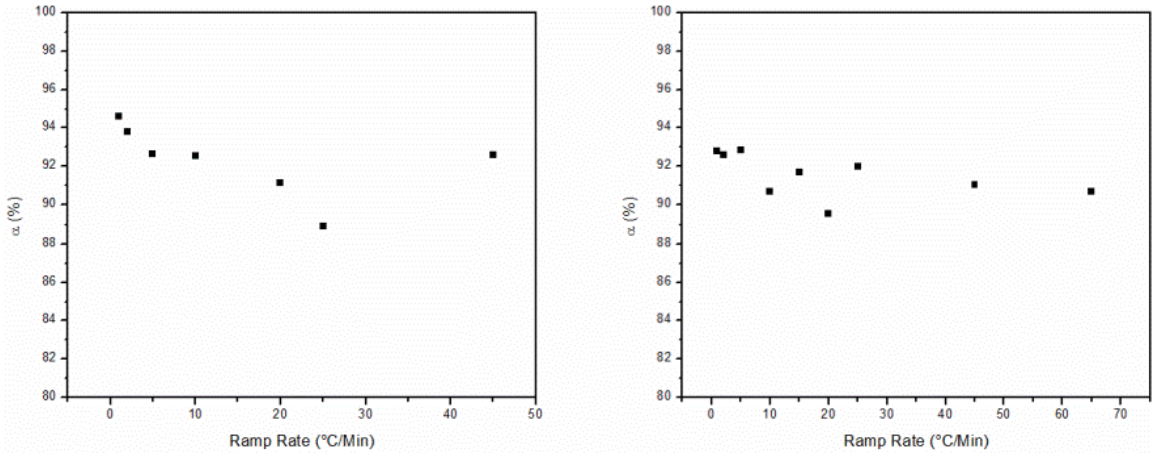

Figure 101. Conversion measured via DSC for 44DDS/TGDDM after 30 (left) and 60 (right) min of cure at 180 °C.

Summary

In summary for these polymers, the differences in conversion with respect to cure heating ramp rate for TGDDM polymers cured with either 33DDS or 44DDS are not a clear as previously proposed. While there appear to be distinct differences between the TGDDM polymers cured with both 33 and 44DDS in how the networks grow and how the chemical reactions progress, similar conversions are reached for both matrix polymers. Because the conversion changes only a little with respect to cure heating ramp rate, there is no reason as to why very fast cure heating ramp rates cannot be realized for this system of polymer, as long as degradation is avoided. That being said, a full molecular level characterization of these polymers is required before complete conclusions can be drawn.

REFERENCES

(1) Hexcel Corporation. HexTow(R) IM7 Carbon Fiber Product Data Sheet, 2010, *000*, 1–2.

(2) Lubin, G. *Handbook of Composites*; 1982.

(3) Morgan, P. *Carbon Fibers and their Composites*; CRC Press: Boca Raton, 2005.

(4) Jackson, M. Effects of Molecular Architecture on Fluid Ingress Behavior of Glassy Polymer Networks, The University of Southern Mississippi, 2011.

(5) Frank, K. Relationships Between Cure Kinetics, Network Architecture, and Fluid Sensitivity in Glassy Epoxies, The University of Southern Mississippi, 2013.

(6) Odian, G. *Principles of Polymerization*; 4th Ed.; John Wiley & Sons: Hoboken, 2004.

(7) Smith, M. B. *March's Advanced Organic Chemistry: Reactions, Mechanisms, and Structure*; 7th ed.; Wiley, 2013.

(8) Meyer, F.; Sanz, G.; Exeiza, A.; Mondragon, I. *Polymer (Guildf).* **1995**, *36*, 1407–1414.

(9) Sohn, D.; Ko, K. *Korea Polym. J.* **1999**, *7*, 181–188.

(10) Jackson, M.; Kaushik, M.; Nazarenko, S.; Ward, S.; Maskell, R.; Wiggins, J. *Polymer (Guildf).* **2011**, *52*, 4528–4535.

(11) Frank, K.; Childers, C.; Dutta, D.; Gidley, D.; Jackson, M.; Ward, S.; Maskell, R.; Wiggins, J. *Polymer (Guildf).* **2013**, *54*, 403–410.

(12) Tucker, S. J. Study of 3,3' vs. 4,4' DDS isomer curatives on physical properties and phenyl ring motions of DGEBA epoxy via molecular dynamics, deuterium NMR, and dielectric spectroscopy, The University of Southern Mississippi.

(13) Childers, C. H.; Hassan, M. K.; Wiggins, J. S. In *Society for the Advancement of Material and Process Engineering Technical Conference*; Seattle, WA, 2014.

(14) Bellenger, V.; Dhaoui, W.; Morel, E.; Verdu, J. *J. Appl. Polym. Sci.* **1988**, *35*, 563–571.

(15) Jackson, M.; Kaushik, M.; Nazarenko, S.; Ward, S.; Maskell, R.; Wiggins, J. *Polymer (Guildf).* **2011**, *52*, 4528–4535.

(16) Guadagno, L.; Vertuccio, L.; Sorrentino, A.; Raimondo, M.; Naddeo, C.; Vittoria, V.; Iannuzzo, G.; Calvi, E.; Russo, S. *Carbon N. Y.* **2009**, *47*, 2419–2430.

(17) Kuo, S.-W.; Chang, F.-C. *Prog. Polym. Sci.* **2011**, *36*, 1649–1696.

(18) Hardis, R.; Jessop, J. L. P.; Peters, F. E.; Kessler, M. R. *Compos. Part A Appl. Sci. Manuf.* **2013**, *49*, 100–108.

(19) Rosu, D.; Cascaval, C. N.; Mustat, F.; Ciobanu, C. *Thermochim. Acta* **2002**, *383*, 119–127.

(20) Vyazovkin, S.; Sbirrazzuoli, N. *Macromolecules* **1996**, *29*, 1867–1873.

(21) Block, C.; Van Mele, B.; Van Puyvelde, P.; Van Assche, G. *React. Funct. Polym.* **2013**, *73*, 332–339.

(22) Lachenal, G.; Pierret, A.; Poissont, N.; Bernard, U. C.; Otude, L. D. **1996**, *4328*.

(23) Nuhiji, B.; Attard, D.; Thorogood, G.; Hanley, T.; Magniez, K.; Fox, B. *Compos. Sci. Technol.* **2011**, *71*, 1761–1768.

(24) Zhang, J.; Guo, Q.; Fox, B. L. *Compos. Sci. Technol.* **2009**, *69*, 1172–1179.

(25) Olmos, D.; Bagdi, K.; Mózcó, J.; Pukánszky, B.; González-Benito, J. *J. Colloid Interface Sci.* **2011**, *360*, 289–299.

(26) Guerrero, P.; De la Caba, K.; Valea, A.; Corcuera, M. A.; Mondragon, I. *Polymer (Guildf).* **1996**, *37*, 2195–2200.

(27) Stewart, I.; Chambers, a.; Gordon, T. *Int. J. Adhes. Adhes.* **2007**, *27*, 277–287.

(28) Trappe, V.; Günzel, S.; Jaunich, M. *Polym. Test.* **2012**, *31*, 654–659.

(29) Lange, J.; Altmann, N.; Kelly, C. .; Halley, P. . *Polymer (Guildf).* **2000**, *41*, 5949–5955.

(30) Carter, J. T.; Emmerson, G. T.; Faro, C. Lo; Mcgrail, P. T.; Moore, D. R. **2003**, *80*, 83–91.

(31) Frank, K. L.; Exley, S. E.; Thornell, T. L.; Morgan, S. E.; Wiggins, J. S. *Polymer (Guildf).* **2012**, *53*, 4643–4651.

(32) Kazilas, M. C.; Partridge, I. K. *Polymer (Guildf).* **2005**, *46*, 5868–5878.

(33) Hubert, P.; Ashrafi, B.; Adhikari, K.; Meredith, J.; Vengallatore, S.; Guan, J.; Simard, B. *Compos. Sci. Technol.* **2009**, *69*, 2274–2280.

(34) Havriliak, S.; Negami, S. *Polymer (Guildf).* **1967**, *8*, 161.

(35) Kremer, F.; Schönhals, A. *Broadband Dielectric Spectroscopy*; Springer: Berlin, 2003; pp. 64, 225.

(36) Kremer, F.; Schönhals, A. *Broadband Dielectric Spectroscopy*; Springer: Berlin, 2003.

(37) Mijovic, J. In *Broadband Dielectric Spectroscopy*; Springer, Ed.; Berlin, 2003; pp. 349–384.

(38) Schönhals, A.; Kremer, F. In *Broadband Dielectric Spectroscopy*; Springer, Ed.; Berlin, 2003; pp. 59–98.

(39) Valentini, L.; Armentano, I.; Puglia, D.; Kenny, J. M. *Carbon N. Y.* **2004**, *42*, 323–329.

(40) Valentini, L.; Puglia, D.; Frulloni, E.; Armentano, I.; Kenny, J. M.; Santucci, S. *Compos. Sci. Technol.* **2004**, *64*, 23–33.

(41) Shaplov, A. S.; Vlasov, P. S.; Lozinskaya, E. I.; Ponkratov, D. O.; Malyshkina, I. A.; Vidal, F.; Okatova, O. V; Pavlov, G. M.; Wandrey, C.; Bhide, A.; Sch, M.; Vygodskii, Y. S. *Macromolecules* **2011**, *44*, 9792–9803.

(42) Bauhofer, W.; Kovacs, J. Z. *Compos. Sci. Technol.* **2009**, *69*, 1486–1498.

(43) Havriliak, S.; Negami, S. *J. Polym Sci. Polym Symp.* **1966**, *14*, 99.

(44) Negami, S.; Ruch, R. J.; Myers, R. R. *J. Colloid Interface Sci.* **1982**, *90*, 117.

(45) Mauritz, K. A. *Macromolecules* **1989**, *22*, 4483.

(46) Zihlif, Z. M. E. W. T. H. A. M. *J. Mater. Sci. Mater. Electron* **2012**.

(47) Nakamura, K.; Fukao, K.; Inoue, T. *Macromolecules* **2012**, *45*, 3850–3858.

(48) Soliman, R. Early Stages of Polymer Crystalization Studied by Dielectric Spectroscopy, Rostock University, 2004.

(49) Shimp, D.; Chin, B.; Hammerton, I. *Chemistry and Technology of Cyanate Ester Resins*; Chapman and Hall: London, 1994; pp. 231–257.

(50) Goertzen, W.; Kessler, M. *Compos. Part A Appl. Sci. Manuf.* **2007**, *38*, 779–784.

(51) Ogura, I.; Yamamoto, T. **2000**, *36*, 1375–1381.

(52) Minoia, A.; Chen, L.; Beljonne, D.; Lazzaroni, R. *Polymer (Guildf).* **2012**, *53*, 5480–5490.

(53) Christensen, S. In *Proceedings of the SAMPE Technical National Meeting.*; Baltimore.

(54) Allen, M. P.; Tildesley, D. J. *Computer Simulation of Liquids*; Oxford University Press: New York, 1989.

(55) Leach, A. R. *Molecular Modeling Principles and Applications*; 2nd Ed.; Pearson Education Limited: Dorchester, 2001.

(56) Chui, C.; Boyce, M. C. *Macromolecules* **1999**, *32*, 3795–3808.

(57) Hassan, W. A. W.; Hammerton, I.; Howlin, B. J. *PLoS One* **2013**, *8*, e61179.

(58) Hossain, D.; Tschopp, M. a.; Ward, D. K.; Bouvard, J. L.; Wang, P.; Horstemeyer, M. F. *Polymer (Guildf).* **2010**, *51*, 6071–6083.

(59) Jawalkar, S. S.; Nataraj, S. K.; Raghu, A. V; Aminabhavi, T. M. *J. Appl. Polym. Sci.* **2008**, *108*, 3572–3576.

(60) Lavine, M. S.; Waheed, N.; Rutledge, G. C. *Polymer (Guildf).* **2003**, *44*, 1771–1779.

(61) Childers, C. H. In *Society for the Advancement of Material and Process Engineering National Conference*.

(62) Childers, C. H.; Tucker, S. J.; Wiggins, J. S. In *American Chemical Society National Symposium*.

(63) Varshney, V.; Patnaik, S. S.; Roy, A. K.; Farmer, B. L. *Macromolecules* **2008**, *41*, 6837–6842.

(64) Sundararaghavan, V.; Kumar, A. 1–20.

(65) Yu, S.; Yang, S.; Cho, M. *Polymer (Guildf).* **2009**, *50*, 945–952.

(66) Fan, H. B.; Yuen, M. M. F. *Polymer (Guildf).* **2007**, *48*, 2174–2178.

(67) Wang, Q.; Suraweera, N. S.; Keffer, D. J.; Deng, S.; Mays, J. *Macromolecules* **2012**, *45*, 6669–6685.

(68) Li, C.; Browning, A. R.; Christensen, S.; Strachan, A. *Compos. Part A Appl. Sci. Manuf.* **2012**, *43*, 1293–1300.

(69) Li, C.; Strachan, A. *Polymer (Guildf).* **2011**, *52*, 2920–2928.

(70) Li, C.; Jaramillo, E.; Strachan, A. *Polymer (Guildf).* **2013**, *54*, 881–890.

(71) Clancy, T. C.; Frankland, S. J. V.; Hinkley, J. a.; Gates, T. S. *Polymer (Guildf).* **2009**, *50*, 2736–2742.

(72) Ward, S.; Harriman, M. Benzoxazines and Compositions Containing the Same. 20130267659, 2013.

(73) Ward, S.; Cross, P.; Maskell, R. Benzoxazine Resins. 20130345352, 2013.

(74) Um, M.-K.; Daniel, I. M.; Hwang, B.-S. *Compos. Sci. Technol.* **2002**, *62*, 29–40.

(75) Kandelbauer, a.; Wuzella, G.; Mahendran, a.; Taudes, I.; Widsten, P. *Chem. Eng. J.* **2009**, *152*, 556–565.

(76) Qiu, J.; Wang, S. *Mater. Chem. Phys.* **2010**, *121*, 295–301.

(77) Olson, B.; Lin, J.; Nazarenko, S.; Jamieson, A. *Macromolecules* **2003**, *36*, 7618.

(78) Kirkegaard, P.; Eldrup, M.; Mogensen, O.; Pedersen, N. *J. Comput. Phys. Commun.* **1981**, *23*, 307.

(79) Eldrup, M.; Lightbody, D.; Shearwood, J. *Chem. Phys.* **1981**, *63*, 51.

(80) Merriam-Webster.com. Monte Carlo. *Merriam-Webster*.

(81) Wu, C.; Xu, W. *Polymer (Guildf).* **2006**, *47*, 6004–6009.

(82) Bandyopadhyay, A.; Valavala, P. K.; Clancy, T. C.; Wise, K. E.; Odegard, G. M. *Polymer (Guildf).* **2011**, *52*, 2445–2452.

(83) *COMPASS Forcefield*; Ver. 6.1.; Accelrys Inc., 2014.

(84) Chui, C.; Boyce, M. C. *Macromolecules* **1999**, *32*, 3795–3808.

(85) Allcock, H. R.; Lampe, F. W.; Mark, J. E. *Contemporary Polymer Chemistry*; 3rd Ed.; Pearson Education, Inc.: Upper Saddle River, 2003.

(86) Sahagun, C. M. Molecular Network Development of a Thermosetting Epoxy-Amine Polymer, University of Southern Mississippi, 2012.

(87) Min, B. G.; Stachurski, Z. H.; Hodgkin, J. H.; Heath, G. R. *Polymer (Guildf).* **1993**, *34*, 3620–3627.

(88) Vogel, H. *Phys* **1921**, *22*, 645.

(89) Ochi, M.; Okazaki, M.; Shinto, M. *J. Polym. Sci. Part B Polym. Phys.* **1982**, *20*, 689–699.